European Space Agency

D-TEC

Technical Note

Equalization of MERIS L1b products from the 2nd reprocessing

M. Bouvet (TEC-EEP)

F. Ramoino (TEC-EEP)

Reference: TEC-EEP/2009.521/MB

Issue: 1, Revision 3

08.12.2009

Table of content

Table of content....3
1 Executive summary 5
2 Introduction....6
2.1 Detector-to-detector systematic radiometric differences and camera interfaces in L1b and L2 data6
2.2 The detector-to-detector systematic differences in each spectral band show patterns seemingly stable over time....9
3 Methodology....11
3.1 The dataset from which equalization coefficients are derived: L1b products over Antarctica 11
3.2 The process of equalization and derivation of equalization coefficients for a single Antarctica scene 11
3.2.1 Retrieval of the $c_{eq}(\lambda,d)$ from a single Antarctica scene....12
3.2.2 Illustration of the equalization coefficient retrieval and equalization process for a single Antarctica scene....13
3.2.3 Few important remarks on the retrieval on $c_{eq}(\lambda,d)$ from a single Antarctica scene 15
3.2.4 Uncertainties associated with the retrieval of $c_{eq}(\lambda,d)$ from a single Antarctica scene 16
3.3 Combining equalization coefficients retrieved from a large number of Antarctica scenes across the full mission 22
3.3.1 Are the equalization coefficients time dependant?....22
3.3.2 Modelling the equalisation coefficients time dependency with a 2nd order polynomial 24
4 Results....26
4.1 The equalization coefficients....26
5 Verification 30
5.1 How to quantitatively measure the improvements brought by the equalization correction? 30
5.2 Focusing on intra camera and inter camera effects 34
5.2.1 Monitoring the evolution of at camera interface radiometric differences 34
5.2.2 Monitoring the evolution of intra camera detector-to-detector systematic radiometric differences....41
5.3 Does the equalization truly work? : visual comparison of equalised and non equalised bands 44
5.3.1 Comparison of equalised and non equalised band ratios: why are band ratios a good mean to verify the equalisation procedure?....44
5.3.2 Antarctica....45
5.3.3 Ocean 46
5.3.4 Vegetation....51
5.4 Conclusion of the verification 52
6 Discussion....53
6.1 Known issues and limitations 53
6.1.1 Determination of coefficients at the edges of the swath....53
6.1.2 Equalization of band 11 53
6.1.3 Equalization of band 15 54
6.1.4 Smile correction....55
6.2 Characteristics of the equalization coefficients 55

6.2.1 What is the impact of the equalization on the global radiometry of a product? 55
6.2.2 Time variations of the standard deviation associated to the detector-to-detector variability of the equalization coefficients 57
6.2.3 Band to band correlations between equalisation coefficients 58
6.2.4 Correlations between $c_{eq}^{t=0}(\lambda,d)$, $\frac{\partial c_{eq}(\lambda,d,t)}{\partial t}$ and $\frac{\partial^2 c_{eq}(\lambda,d,t)}{\partial t^2}$ 61
6.2.5 Is there a particular spatial frequency characterising the detector-to-detector systematic differences? 66
6.2.6 Is there any impact of the OCL off period on the equalization coefficient retrieval 70
6.3 Impact of the correction on the retrieval of water leaving reflectances 71
6.4 The detector-to-detector systematic radiometric differences: what causes them? 71
6.4.1 A straylight issue? 73
6.4.2 A dark current issue? 73
6.4.3 A non linearity issue? 73
6.4.4 A smear issue? 73
6.4.5 A calibration issue? 73
6.5 Could the equalization coefficients retrieval for single spectral bands be further constrained by band ratio equalization coefficients? 73
6.6 Ground segment implementation: practical considerations 74
6.6.1 Implementation of the equalization procedure 74
6.6.2 Smile correction 74
6.6.3 FR versus RR 74
6.6.4 Didn't we derive Quality Indicators? 75
6.6.5 Computing time 75
7 Conclusion 76
8 Acknowledgement 76
9 References 77

1 Executive summary

We observe detector-to-detector systematic radiometric differences in MERIS L1b products from the 2nd reprocessing. A simple radiometric model to explain these differences is proposed and inverted to retrieve equalization coefficients. The inversion is based on 104 cloud free scenes over Antarctica. The equalization coefficients depend on time, detector index and spectral band. They reveal detector-to-detector systematic radiometric differences in the range of 0.03% to 0.2 % RMSE at TOA reflectance level. We applied these coefficients to 101 independent cloud free scenes and measured the improvements brought by the equalization via a proxies for the across track and along track noise. The equalization leads to significant noise reduction in the across track direction reaching 100 % on data from 2009. This is qualitatively confirmed by visual inspection of equalized ocean and vegetation L1b scenes. The potential impact of the equalization on ocean colour product is assessed. We conclude that it should NOT have a significant impact on the retrieval of water leaving reflectance in the visible range (412 to 560 nm) for Case 1 waters in terms of bias and RMSE.

The equalization coefficients also provide insight into the evolution of the detector-to-detector radiometric differences and the at camera interface radiometric differences throughout the MERIS mission. We observe an increase of detector-to-detector radiometric differences amplitude (RMSE) over time by a factor 2 to 3 during the full mission and a general increase of radiometric differences at camera interfaces reaching up to 1%, at TOA reflectance level, in 2009.

2 Introduction

2.1 Detector-to-detector systematic radiometric differences and camera interfaces in L1b and L2 data

There are obvious image quality issues with the MERIS L1b and L2 products from the 2nd reprocessing: camera interfaces and detector-to-detector systematic differences are visible. These visual artefacts also constitute a potential threat for the accuracy and precision of L2 geophysical products.
As a representative illustration of these artefacts, Figure 1 shows the Algal 1 L2 product over the Eastern Mediterranean.

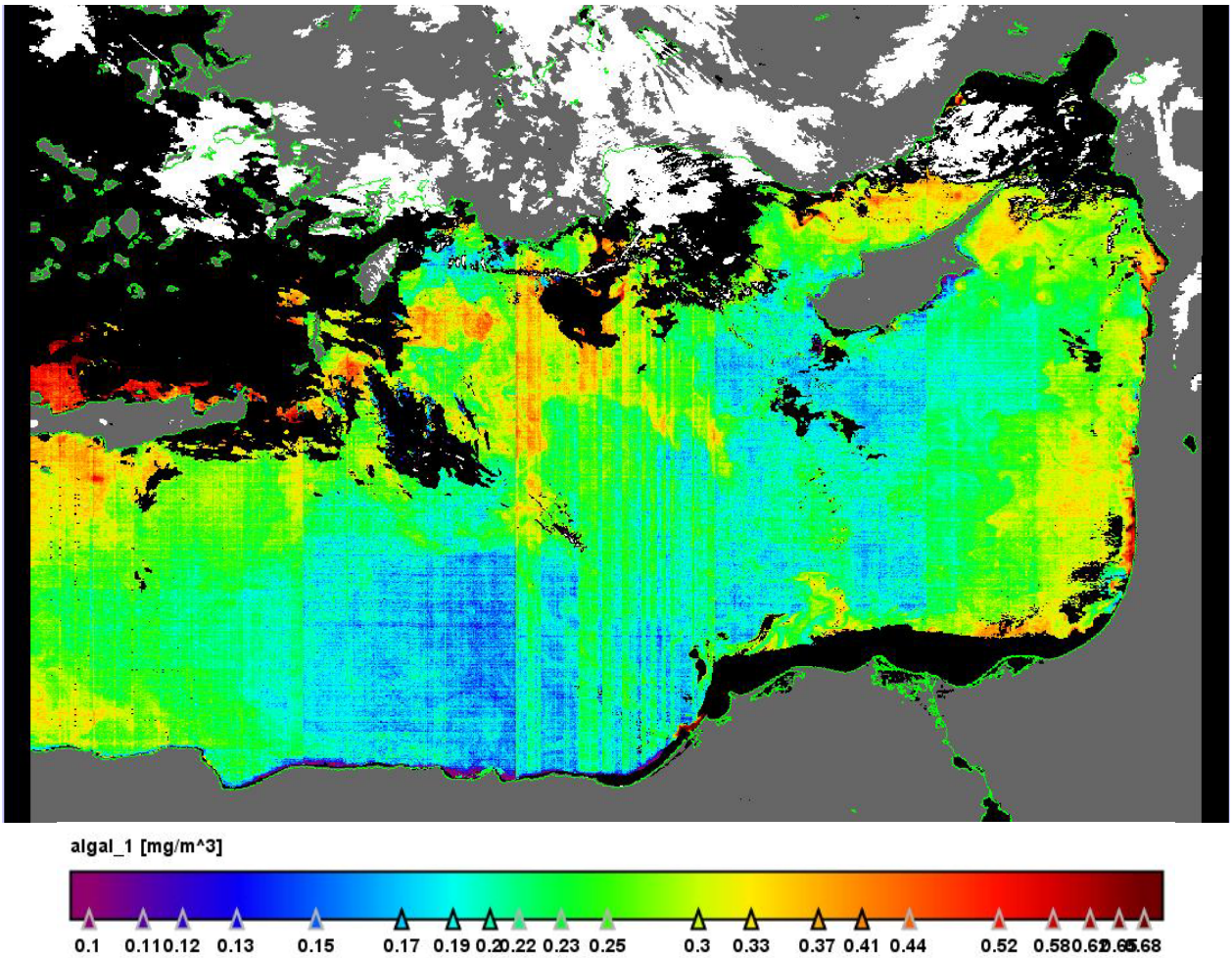

Figure 1: The L2 algal_1 product for MER_RR__2PPBCM20090203_082156_000002002076_00107_36233_0078

Figure 2 is a L1b RGB over Antarctica. Camera interfaces can be distinguished. This is somewhat to be expected since these scene is not smile corrected.

Figure 2: MER_RR__1PNMAP20090103_000513_000000562075_00159_35784_0001 - RGB

In *Figure 3* we display $\frac{\rho_{MERIS}^{TOA}(865)}{\rho_{MERIS}^{TOA}(778)}$. Not only are camera interfaces visible but also detector-to-detector systematic differences.

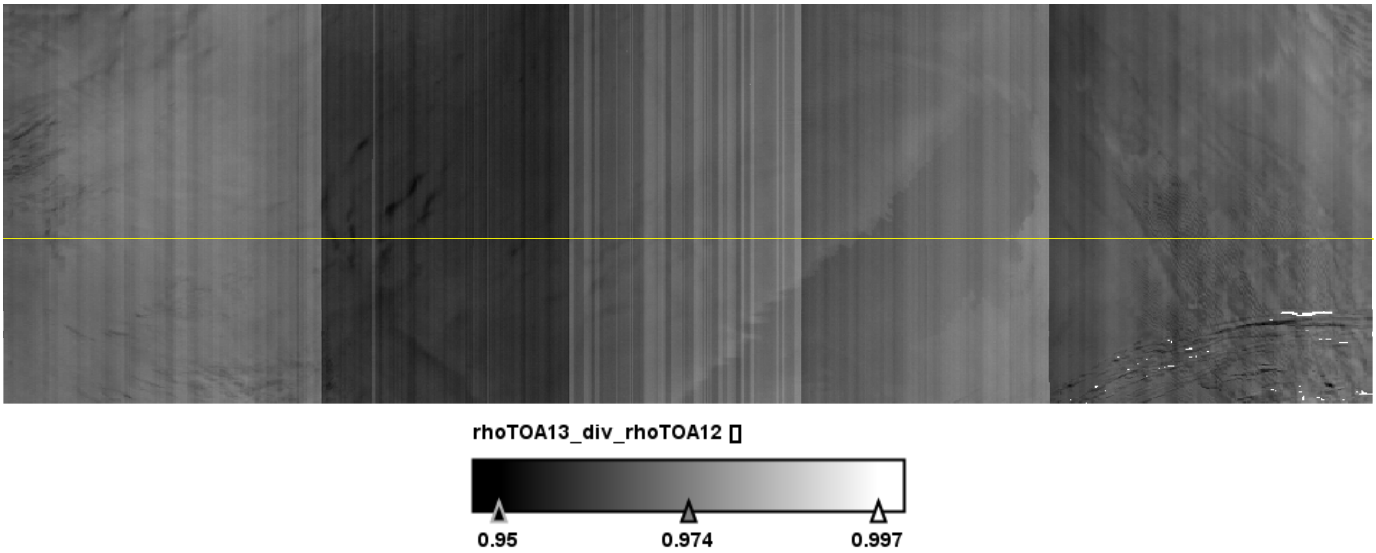

Figure 3: MER_RR__1PNMAP20090103_000513_000000562075_00159_35784_0001 $\frac{\rho_{MERIS}^{TOA}(865)}{\rho_{MERIS}^{TOA}(778)}$ *– no smile correction*

The detector-to-detector systematic noise seems to be constant as the instrument scans along track.

The smile correction (performed with BEAM) improves the situation mainly at the at camera interface boundaries (see *Figure 4*). Camera boundaries however remain visible after smile correction and the detector-to-detector systematic radiometric differences remain present.

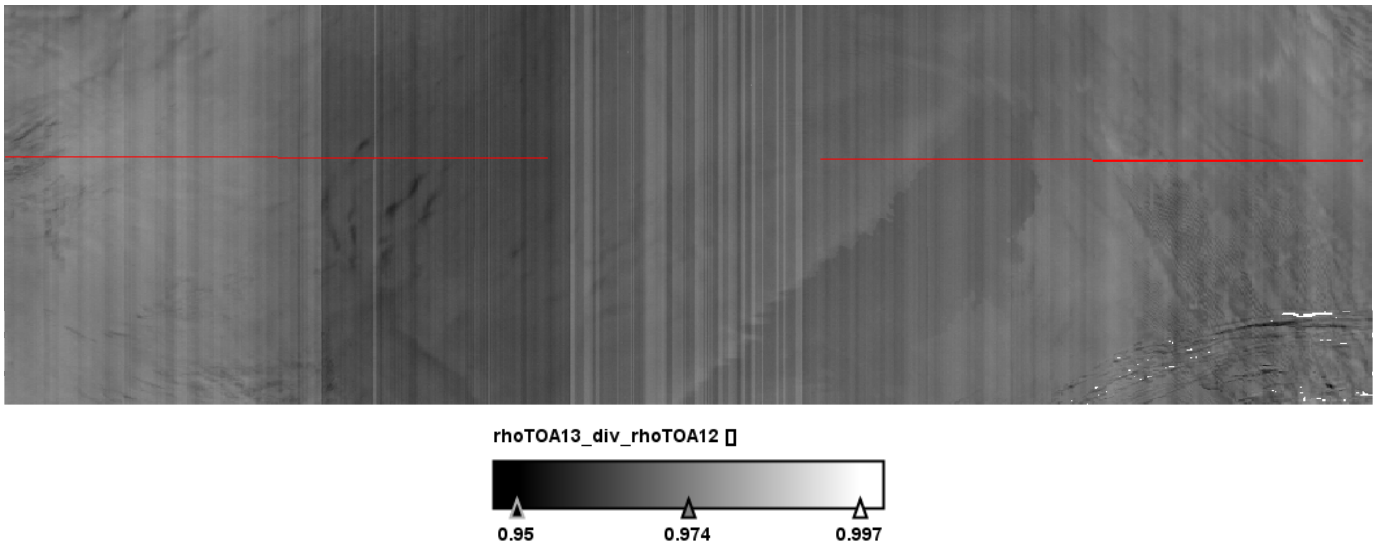

Figure 4: MER_RR__1PNMAP20090103_000513_000000562075_00159_35784_0001 $\frac{\rho_{MERIS}^{TOA}(865)}{\rho_{MERIS}^{TOA}(778)}$ *after smile correction*

To quantitatively illustrate these detector to detector effect and camera effects, in respectively Figure 5 and Figure 6 we show the across track profile $\frac{\rho_{MERIS}^{TOA}(865)}{\rho_{MERIS}^{TOA}(778)}$ without and with smile correction, along a transect materialized in red in Figure 4.

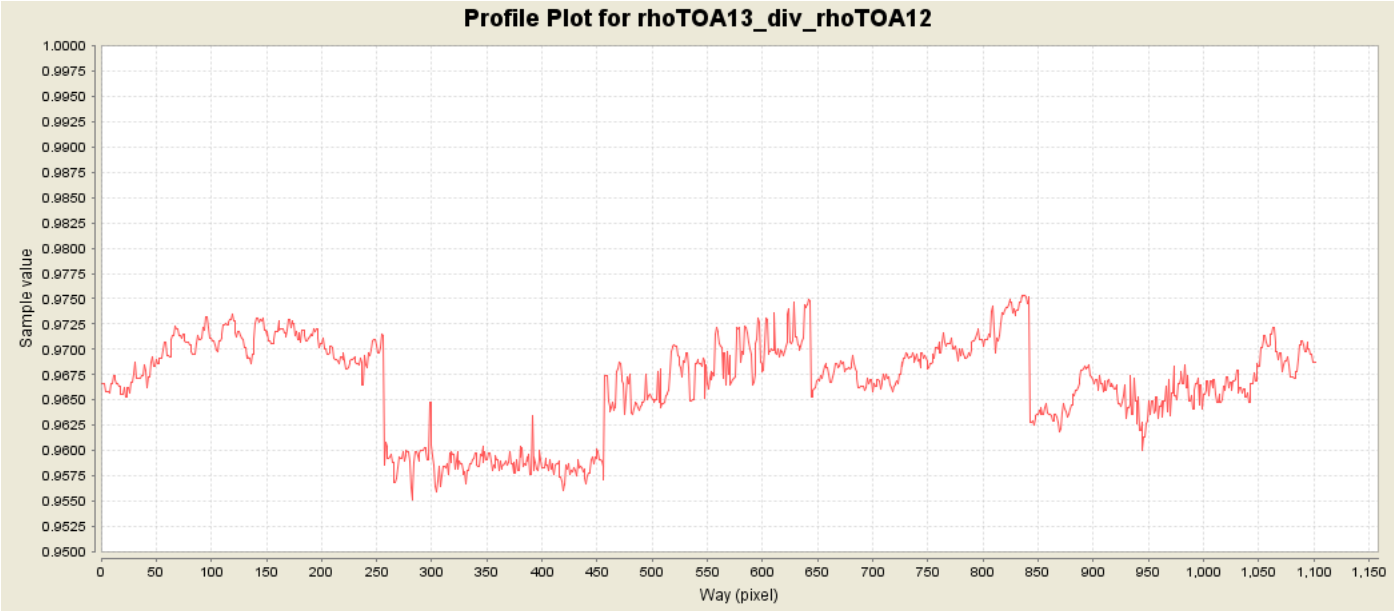

Figure 5: MER_RR__1PNMAP20090103_000513_000000562075_00159_35784_0001
Across track profile – no smile correction

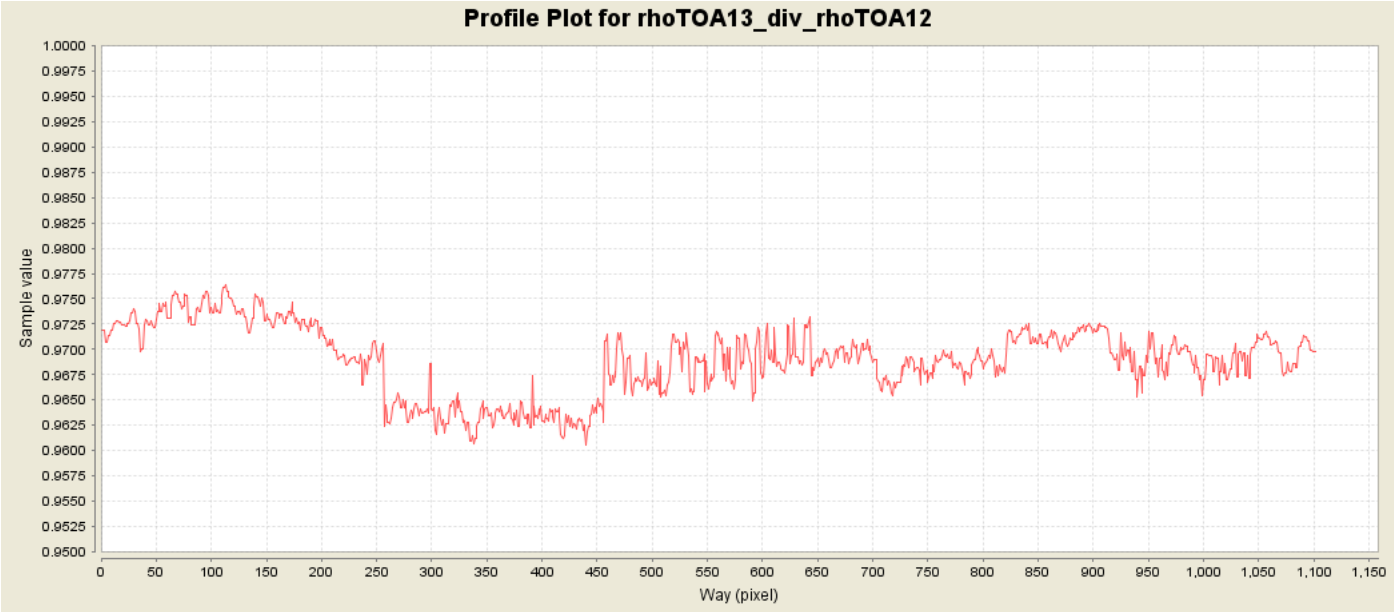

Figure 6: MER_RR__1PNMAP20090103_000513_000000562075_00159_35784_0001
Across track profile after smile correction

2.2 The detector-to-detector systematic differences in each spectral band show patterns seemingly stable over time

In the previous product, we observed that the detector-to-detector systematic radiometric differences on TOA reflectance band ratios seem to be invariant along track over periods of seconds to minutes. The next

product, from the same year (2009) but on a different year, shows that detector-to-detector systematic radiometric differences are persistent patterns even when observed also over time scales of days.

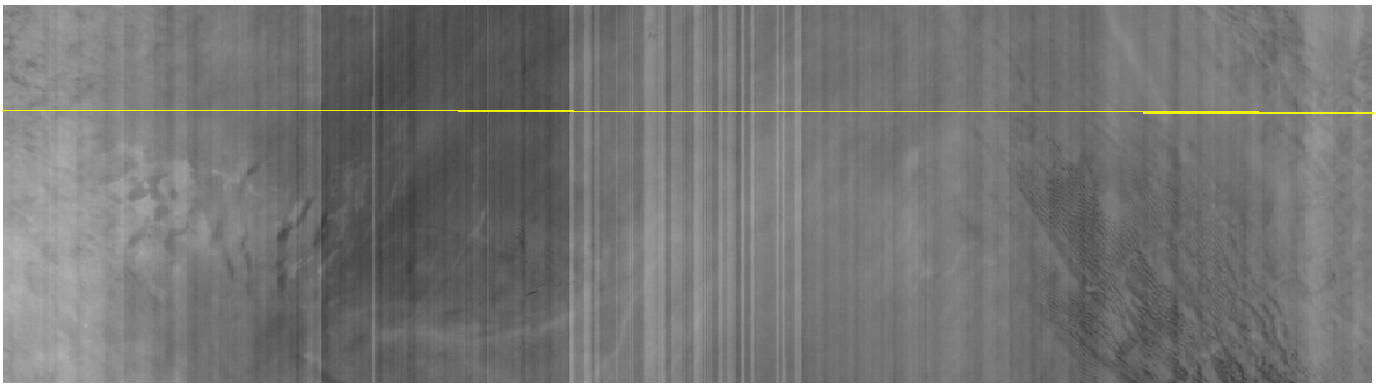

Figure 7:MER_RR__1PNMAP20090112_235059_000000542075_00302_35927_0001
L1b rhoTOA13/rhoTOA12 after smile correction

If we take a product from one year before (2008), again we observe the same detector-to-detector radiometric difference pattern (see *Figure 8*).

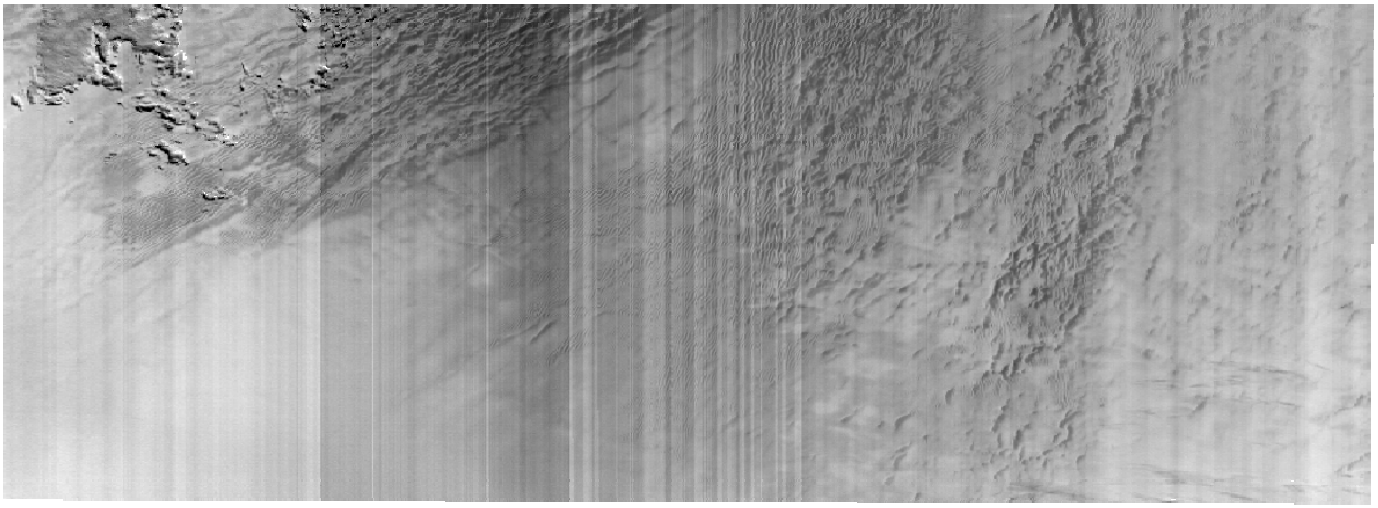

Figure 8: MER_RR__1PPBCM20081201_173407_000000702074_00198_35322_0007
L1b rhoTOA13/rhoTOA12 after smile correction

The temporal persistence of the systematic detector-to-detector radiometric pattern has motivated the development of an equalization methodology based on detector dependant equalization coefficients.

3 Methodology

3.1 The dataset from which equalization coefficients are derived: L1b products over Antarctica

All MERIS L1b RR acquisitions from the 2nd reprocessing over Antarctica from 2002 to 2009 were downloaded from MERCI. They are about 500 km long along track. They were visually cloud screened to ensure a very low cloud cover across the swath. The cloud screening resulted into clear sky 205 products. They were split into 104 products from which the equalization coefficients are retrieved and 101 products on which the equalization procedure is applied and its performance is measured. Here follows an example of these products. The scene is visually spatially and radiometrically homogeneous.

Figure 9: MER_RR__1PPBCM20070110_224832_000000562054_00330_25434_0058.N1 - RGB

3.2 The process of equalization and derivation of equalization coefficients for a single Antarctica scene

Assumption 1: The TOA reflectance measured by MERIS after smile correction is proportional to a the true value of this reflectance, by 'true' it is meant as would be measured by a perfect instrument:

$$\rho_{MERIS}^{TOA}(\lambda,x,y) = c_{eq}(\lambda, d = f(x,y))\rho_{TRUE}^{TOA}(\lambda,x,y)$$

where $\rho_{MERIS}^{TOA}(\lambda,x,y)$ is the MERIS L1b <u>smile corrected</u> band, x and y are the pixel coordinate in the band in the image, d is the detector index (0 to 923 in RR products), λ is the band number (from 1 to 15), and $\rho_{TRUE}^{TOA}(\lambda,x,y)$ is an estimate of what could be measured by a perfect instrument. The $c_{eq}(\lambda, d = f(x,y))$ or $c_{eq}(\lambda,d)$are the equalization coefficients.

The purpose of the equalization procedure is to compute $\rho_{TRUE}^{TOA}(\lambda,x,y)$ from $\rho_{MERIS}^{TOA}(\lambda,x,y)$ and $c_{eq}(\lambda,d)$.

3.2.1 Retrieval of the $c_{eq}(\lambda,d)$ from a single Antarctica scene

First of all, $\rho_{MERIS}^{TOA}(\lambda,x,y)$ is projected into the detector space, that is, each pixel of the L1b image is reassigned to the detector than measured it. In this detector space, the image is 924 pixel wide rather than 1121. We thus obtain $\rho_{MERIS}^{TOA}(\lambda,f,d)$ where *f* is the frame number and *d* the detector number.

If we average the TOA smile corrected reflectance over all frames for a constant detector index we obtain:

$$\overline{\rho}_{MERIS}^{TOA}(\lambda,d) \equiv \frac{1}{N_{pix}(d)} \times \sum_{f=1}^{f_{\max}} \rho_{MERIS}^{TOA}(\lambda,f,d)$$

where $N_{pix}(d)$ is the number of pixels in a given band image which have the same detector index *d* and f_{max} the maximum number of frames in the product.

Using the same definition for the true band it follows:

$$\overline{\rho}_{MERIS}^{TOA}(\lambda,d) = c_{eq}(\lambda,d)\overline{\rho}_{TRUE}^{TOA}(\lambda,d)$$

Assumption 2: $\overline{\rho}_{TRUE}^{TOA}(\lambda,d)$ ***variations with the detector index d can be approximated by the following smoothed function of*** $\overline{\rho}_{MERIS}^{TOA}(\lambda,d)$***:***

$$\overline{\rho}_{TRUE}^{TOA}(\lambda,d) \approx \frac{1}{N_{smooth}} \times \sum_{\delta=d-\frac{N_{smooth}-1}{2}}^{\delta=d+\frac{N_{smooth}-1}{2}} \overline{\rho}_{MERIS}^{TOA}(\lambda,\delta-d) I_{N_{smooth}}(\delta)$$

Where $N_{smooth}-1$ is the size of the sliding average window over which the smoothing is done and $I_{N_{smooth}}(\delta)$ is a unity vector of size N_{smooth}. Moreover we assume:

$\overline{\rho}_{TRUE}^{TOA}(\lambda,d) = \overline{\rho}_{TRUE}^{TOA}(\lambda,0)$ if d < 0

and,

$\overline{\rho}_{TRUE}^{TOA}(\lambda,d) = \overline{\rho}_{TRUE}^{TOA}(\lambda,d_{\max})$ if d > $d_{\max}$

This is a sliding window average of the curve $\overline{\rho}_{MERIS}^{TOA}(\lambda,d)$ (see illustration in *Figure 10*). The choice of the N_{smooth} value is of significant importance. It is chosen to be larger than the observed typical spatial period (expressed in number of RR detectors) of the observed vertical stripping induced by detector-to-detector systematic differences. It is empirically determined by visually studying these patterns (see for instance *Figure 2* to *Figure 8*). Patterns of more than 50 are not observed. This doesn't mean that there are no such pattern, but they spatial variabiliby become difficult to distinguish from the geophysical variability of the signal. We have empirically set N_{smooth} to 51 (it should be per definition an uneven number). Once $\overline{\rho}_{TRUE}^{TOA}(\lambda,d)$ and $\overline{\rho}_{MERIS}^{TOA}(\lambda,d)$ have been computed we can derive the equalization coefficients:

$$c_{eq}(\lambda,d) = \frac{\overline{\rho}_{MERIS}^{TOA}(\lambda,d)}{\overline{\rho}_{TRUE}^{TOA}(\lambda,d)}$$

3.2.2 Illustration of the equalization coefficient retrieval and equalization process for a single Antarctica scene

The methodology we applied to the retrieval of equalization coefficients and the equalization of bands can be summarized in several steps:

1. Starting from an Antarctica L1b product, a smile correction is applied. The L1b radiances are then converted to reflectances.
2. The L1b product is then projected into the detector space, that is, each pixel of the L1b image is reassigned to a detector. In this detector space, the image is 924 pixel wide rather than 1121.
3. The mean value of a band TOA reflectance along all frames, for a given detector index $\overline{\rho}_{MERIS}^{TOA}(\lambda, d)$ (varying from 0 to 923 in reduced resolution) is then computed (see *Figure 10*).

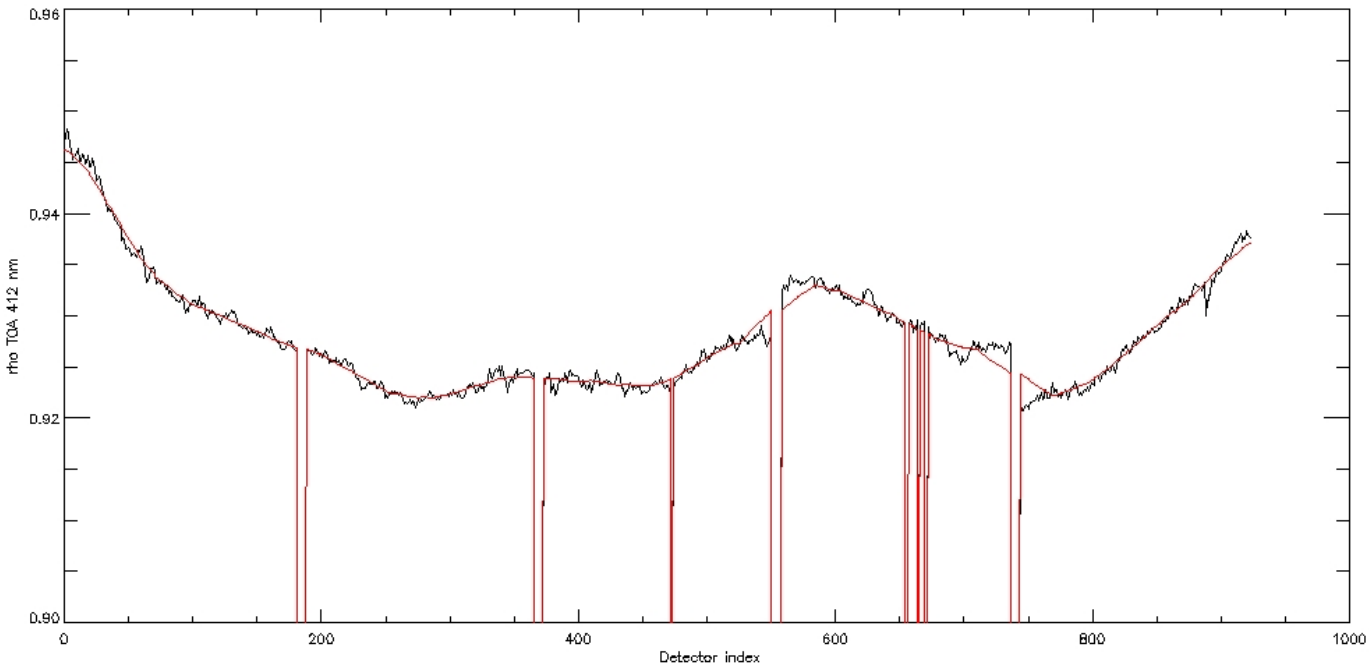

Figure 10: MER_RR__1PPBCM20070110_224832_000000562054_00330_25434_0058.N1
In black, the mean value of smile corrected reflectance at 412 nm for a given detector index $\overline{\rho}_{MERIS}^{TOA}(\lambda, d)$ *as a function of the detector index. In red the smoothed curve corresponding to* $\overline{\rho}_{TRUE}^{TOA}(\lambda, d)$.

4. A sliding average technique is applied to smooth the mean value of smile corrected reflectance for a given detector index. Under assumption 1 this is a proxy for $\overline{\rho}_{TRUE}^{TOA}(\lambda, d)$. The sliding average is done using a 51 pixel box (see *Figure 10*)
5. The ratio of the smoothed curve to the mean value of a band TOA reflectance along all frames original curve (red curve over black curve in *Figure 10*) gives the equalisation coefficients $c_{eq}(\lambda, d)$ (see *Figure 11*).

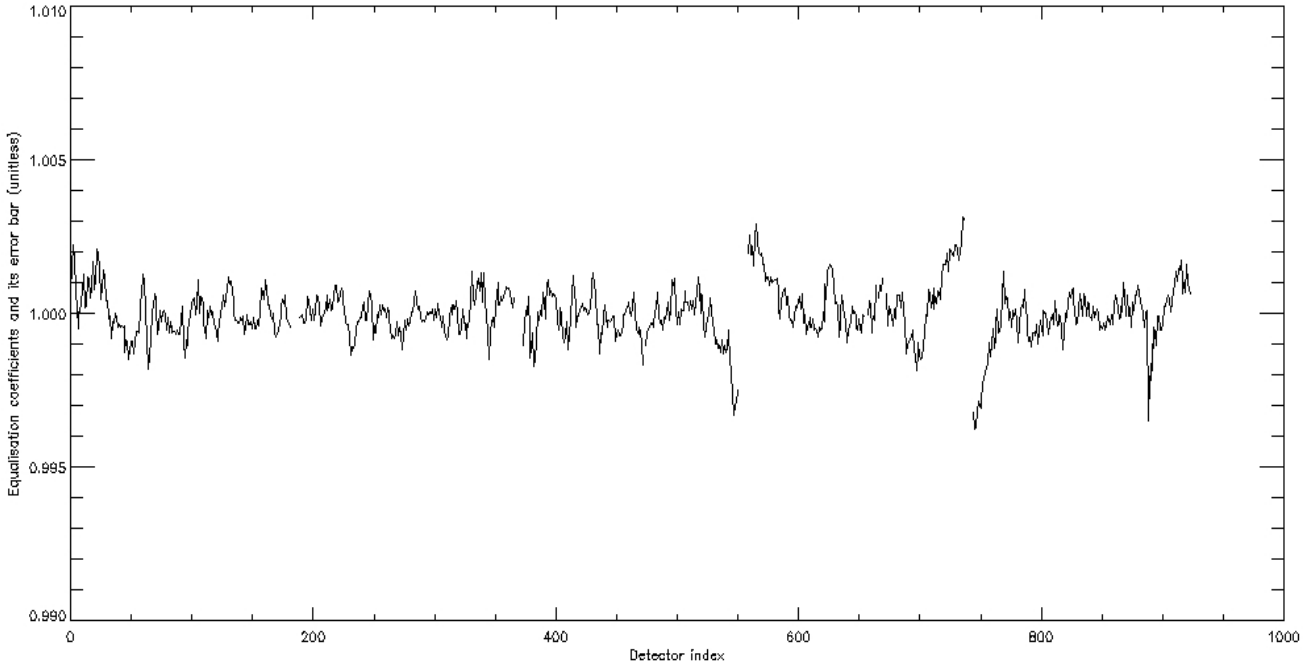

Figure 11: MER_RR__1PPBCM20070110_224832_000000562054_00330_25434_0058.N1
The equalization coefficients $c_{eq}(\lambda, d)$ *for the 412 nm band*

6. Once we have obtained these equalization coefficients for each spectral band and each detector, we can simply equalize the band image, as a sanity check, by applying the set of detector dependant equalisation coefficients we derived from the scene itself (see *Figure 12*) using:

$$\rho_{TRUE}^{TOA}(\lambda, x, y) = \frac{\rho_{MERIS}^{TOA}(\lambda, x, y)}{c_{eq}(\lambda, d = f(x, y))}$$

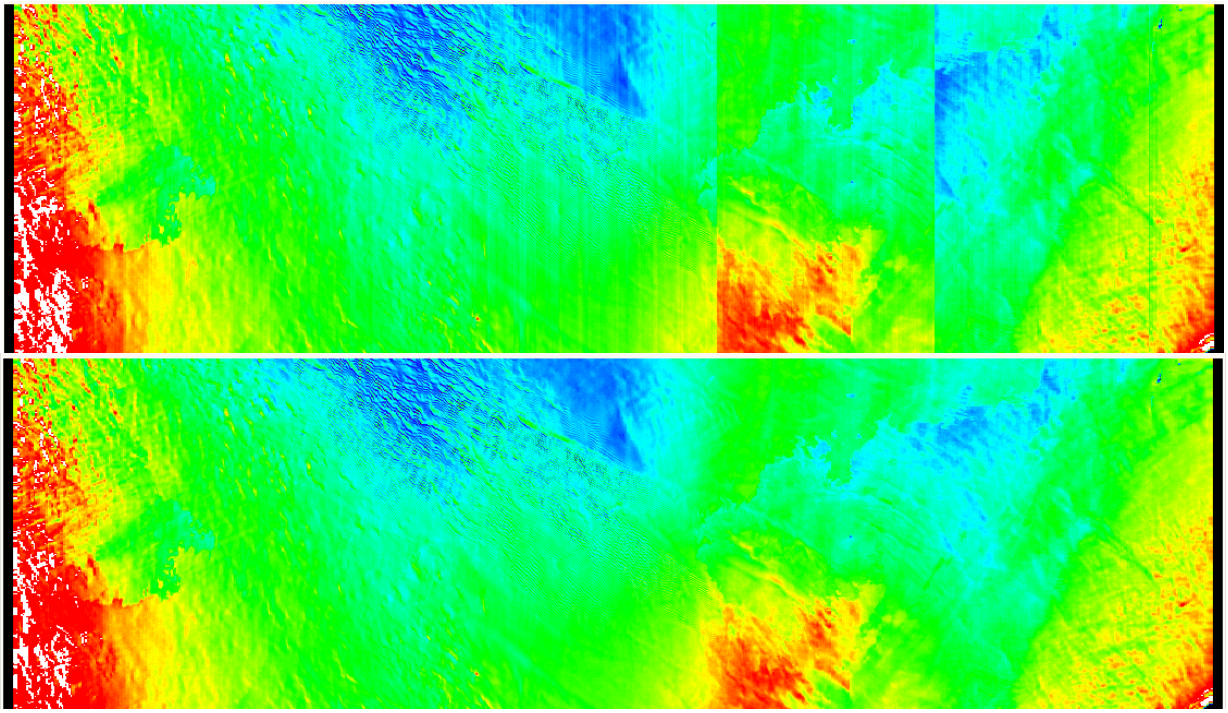

Figure 12: MER_RR__1PPBCM20070110_224832_000000562054_00330_25434_0058.N1 The top image is the original smile corrected TOA reflectance at 412 nm . The bottom image is the equalized TOA reflectance at 412 nm. Both images use the same color scale ranging from 0.9 to 0.95.

3.2.3 Few important remarks on the retrieval on $c_{eq}(\lambda,d)$ from a single Antarctica scene

3.2.3.1 Remark 1: The $c_{eq}(\lambda,d)$ must be retrieved over a spatially homogeneous surface but they should be applicable to complex scenes as well

Assumption 2 is valid only for radiometrically homogeneous scenes like the one we chose. It is invalid in complex scenes (e.g.: a coastline or a cloud border oriented in the along track direction). This implies that the equalization process become impossible for complex scenes because the variations of $\overline{\rho}_{MERIS}^{TOA}(\lambda,d)$ cannot solely be attributed to detector-to-detector systematic differences but become the combination of true geophysical variations a detector-to-detector systematic differences. However, if the $c_{eq}(\lambda,d)$ are not time dependant (or if we can model their time dependency), the $c_{eq}(\lambda,d)$ retrieved from a single Antarctica scene should be applicable to any scene, regardless of its spatial homogeneity. In other words, the retrieval of the $c_{eq}(\lambda,d)$ is bounded to homogeneous surfaces such as Antarctica but not their applicability.

3.2.3.2 Remark 2: Assumption 1 and 2 are a posteriori justified

The fact that the equalisation correction works for the Antarctica scenes (it is visually significantly improving the image quality) implicitly validates assumption 1 and assumption 2 over these areas.

3.2.3.3 Remark 3: The averaged of $c_{eq}(\lambda,d)$ across the swath is 1

We can see from *Figure 11* that the mean $c_{eq}(\lambda,d)$ over the full swath is about 1. Should this not be true, the correction would introduce a bias to the radiometry of the image. We can evaluate this bias by computing the so-called uncertainty on the mean:

$$\sigma_{Cal_bias} = \frac{stddev(c_{eq}(\lambda,d))}{\sqrt{d_{\max}}} \approx \frac{0.1\%}{\sqrt{924}} \approx 0.003\%$$

This is not significant.

3.2.3.4 Remark 4: Band 11 and band 15 are not smile corrected

We have implemented the smile correction excluding band 11 and 15 because of issues related to gaseous absorption in these two bands. Moreover, band 11 position was changed in December 2002. The retrieval of equalisation coefficients as it is described in the present document is not applicable to band 11 and 15. We however treated these bands in our computations as if they had been smile corrected, hoping to learn something. All results hereafter presented concerning these bands should however be interpreted extremely cautiously.

3.2.4 Uncertainties associated with the retrieval of $c_{eq}(\lambda,d)$ from a single Antarctica scene

In the previous section, we have described the steps leading to the retrieval of the equalization coefficients. In this section we described the steps leading to the assessment of their uncertainties. These steps were guided by the QA4EO guidelines (see R - 4). We have also found valuable help in R - 3.

The first step in our algorithm for the retrieval of the $c_{eq}(\lambda,d)$ is to compute $\overline{\rho}^{TOA}_{MERIS}(\lambda,d)$. This simple averaging is performed with the $\rho^{TOA}_{MERIS}(\lambda,f,d)$ as input. We have no quality indicator in MERIS products (e.g.: uncertainty on systematic error and random error). Inspired by the uncertainty budget analysis presented in R - 5, we have tried to derive conservative estimates of the systematic and random errors for the MERIS L1b smile corrected TOA reflectances.

Assumption 3:

1. ***The upper limit on the systematic error, ε_{MERIS_TOA}, associated to the smile corrected MERIS TOA reflectance $\rho^{TOA}_{MERIS}(\lambda,f,d)$ is 3%.***
2. ***The random errors associated to the smile corrected MERIS TOA reflectance $\rho^{TOA}_{MERIS}(\lambda,f,d)$ follow a normal distribution with standard deviation $\sigma_{MERIS_TOA} = 0.66\%$ (i.e., 99.7 % of the random errors below 2%)***

3.2.4.1 Impact of L1b systematic errors on the computation of the $c_{eq}(\lambda,d)$

Let's first consider the impact of a systematic error ε_{MERIS_TOA} on the $c_{eq}(\lambda,d)$. We defined:

$$\overline{\rho}_{MERIS}^{TOA}(\lambda,d) \equiv \frac{1}{N_{pix}(d)} \times \sum_{f=1}^{f_{\max}} \rho_{MERIS}^{TOA}(\lambda, f, d)$$

From this equation we infer that the systematic error ε_{MERIS_TOA} associated to $\rho_{MERIS}^{TOA}(\lambda, f, d)$ will translate into an identical systematic error on $\overline{\rho}_{MERIS}^{TOA}(\lambda,d)$.

From the definition of $\overline{\rho}_{TRUE}^{TOA}(\lambda,d)$, i.e., $\overline{\rho}_{TRUE}^{TOA}(\lambda,d) = \frac{1}{N_{smooth}} \times \sum_{\delta=d-\frac{N_{smooth}-1}{2}}^{\delta=d+\frac{N_{smooth}-1}{2}} \overline{\rho}_{MERIS}^{TOA}(\lambda,\delta-d) I_{N_{smooth}}(\delta)$ we similarly derive that the systematic error associated to $\overline{\rho}_{TRUE}^{TOA}(\lambda,d)$ will also be ε_{MERIS_TOA}.

From the definition of the equalization coefficients we thus get:

$$c_{eq}(\lambda,d) = \frac{\overline{\rho}_{MERIS}^{TOA}(\lambda,d) + \varepsilon_{MERIS_TOA}}{\overline{\rho}_{TRUE}^{TOA}(\lambda,d) + \varepsilon_{MERIS_TOA}} = \frac{\overline{\rho}_{MERIS}^{TOA}(\lambda,d) + \overline{\rho}_{TRUE}^{TOA}(\lambda,d) - \overline{\rho}_{TRUE}^{TOA}(\lambda,d) + \varepsilon_{MERIS_TOA}}{\overline{\rho}_{TRUE}^{TOA}(\lambda,d) + \varepsilon_{MERIS_TOA}}$$

$$c_{eq}(\lambda,d) = 1 + \frac{\overline{\rho}_{MERIS}^{TOA}(\lambda,d) - \overline{\rho}_{TRUE}^{TOA}(\lambda,d)}{\overline{\rho}_{TRUE}^{TOA}(\lambda,d) + \varepsilon_{MERIS_TOA}}$$

The systematic error ε_{C_eq} on $c_{eq}(\lambda,d)$ becomes:

$$\varepsilon_{C_eq} = 1 + \frac{\overline{\rho}_{MERIS}^{TOA}(\lambda,d) - \overline{\rho}_{TRUE}^{TOA}(\lambda,d)}{\overline{\rho}_{TRUE}^{TOA}(\lambda,d) + \varepsilon_{MERIS_TOA}} - \left(1 + \frac{\overline{\rho}_{MERIS}^{TOA}(\lambda,d) - \overline{\rho}_{TRUE}^{TOA}(\lambda,d)}{\overline{\rho}_{TRUE}^{TOA}(\lambda,d)}\right)$$

$$= \frac{\overline{\rho}_{MERIS}^{TOA}(\lambda,d) - \overline{\rho}_{TRUE}^{TOA}(\lambda,d)}{\overline{\rho}_{TRUE}^{TOA}(\lambda,d) + \varepsilon_{MERIS_TOA}} - \frac{\overline{\rho}_{MERIS}^{TOA}(\lambda,d) - \overline{\rho}_{TRUE}^{TOA}(\lambda,d)}{\overline{\rho}_{TRUE}^{TOA}(\lambda,d)}$$

$$= \frac{-\varepsilon_{MERIS_TOA} \times \left[\overline{\rho}_{MERIS}^{TOA}(\lambda,d) - \overline{\rho}_{TRUE}^{TOA}(\lambda,d)\right]}{\left(\overline{\rho}_{TRUE}^{TOA}(\lambda,d) + \varepsilon_{MERIS_TOA}\right) \times \overline{\rho}_{TRUE}^{TOA}(\lambda,d)}$$

$$\approx \frac{-\varepsilon_{MERIS_TOA} \times \left[\overline{\rho}_{MERIS}^{TOA}(\lambda,d) - \overline{\rho}_{TRUE}^{TOA}(\lambda,d)\right]}{\left(\overline{\rho}_{TRUE}^{TOA}(\lambda,d)\right)^2}$$

Leading to:

$$\varepsilon_{C_eq} \approx \frac{-\varepsilon_{MERIS_TOA} \times \left[\overline{\rho}_{MERIS}^{TOA}(\lambda,d) - \overline{\rho}_{TRUE}^{TOA}(\lambda,d)\right]}{\left(\overline{\rho}_{TRUE}^{TOA}(\lambda,d)\right)^2}$$

Let's try to give an order of magnitude of ε_{C_eq}. From *Figure 10* and *Figure 11* we see that $\frac{\left[\overline{\rho}_{MERIS}^{TOA}(\lambda,d)-\overline{\rho}_{TRUE}^{TOA}(\lambda,d)\right]}{\overline{\rho}_{TRUE}^{TOA}(\lambda,d)}$ is less than 0.5 %. Over Antarctica $\overline{\rho}_{TRUE}^{TOA}(\lambda,d)$ is about 0.9 in all bands except band 11.

Thus, for a $c_{eq}(\lambda,d)$ corresponding to a correction of 0.5% at TOA reflectance level (i.e. $c_{eq}(\lambda,d)=1.005$), a 3 % uncertainty on the systematic error on $\rho_{MERIS}^{TOA}(\lambda,f,d)$ leads to a 0.00015 uncertainty on $c_{eq}(\lambda,d)$, i.e., $c_{eq}(\lambda,d)=1.00500\pm0.00015$. This translates into a 0.015% impact at TOA reflectance level on the final $\rho_{TRUE}^{TOA}(\lambda,f,d)$ when the $c_{eq}(\lambda,d)$ are applied to equalize a L1b scene. This is about half the quantification noise at such reflectance level.

As a conclusion, the impact of systematic errors ε_{MERIS_TOA} < 3% on the equalized product $\rho_{TRUE}^{TOA}(\lambda,f,d)$ is negligible. In other words, the equalization process is insensitive to systematic errors associated to the MERIS L1b.

3.2.4.2 Impact of L1b random errors on the computation of the equalization coefficients

We compute the uncertainty $\sigma_{MERIS}(\lambda,d)$ associated to $\overline{\rho}_{MERIS}^{TOA}(\lambda,d)$ through the error propagation equation (see Appendix A in R - 3 for details):

$$\sigma^2{}_{MERIS}(\lambda,d)=\left[\frac{1}{N_{pix}(d)}\right]^2\times\sum_{f=1}^{f_{max}}\sigma^2_{MERIS_TOA}=\frac{\sigma^2_{MERIS_TOA}}{N_{pix}(d)}=\frac{\left[0.0066\times\overline{\rho}_{MERIS}^{TOA}(\lambda,d)\right]^2}{N_{pix}(d)}$$

Similarly, we obtain the uncertainty $\sigma_{TRUE}(\lambda,d)$ associated to the computation of $\overline{\rho}_{TRUE}^{TOA}(\lambda,d)$:

$$\sigma^2{}_{TRUE}(\lambda,d)=\frac{\sigma^2{}_{MERIS}(\lambda,d)}{N_{smooth}}$$

The values of $\sigma_{MERIS}(\lambda,d)$and $\sigma_{TRUE}(\lambda,d)$ for an Antarctica scene are given in *Figure 14*. They correspond to uncertainties rescales at TOA reflectance level of respectively generally (depending on the scene) about 0.05 % RMSE and 0.01% RMSE. For comparison, a quantification of $\frac{1}{2^{12}}$ corresponds to 0.024 % of the TOA signal for a reflectance level of 1.

3.2.4.3 Impact of assumption 2 on the computation of the equalization coefficients

In addition to the two statistical uncertainties associated to the computation of $\overline{\rho}_{MERIS}^{TOA}(\lambda,d)$ and $\overline{\rho}_{TRUE}^{TOA}(\lambda,d)$, there is a more fundamental methodological uncertainty: to which extend is our assumption 2 valid? (Assumption 2 is $\overline{\rho}_{TRUE}^{TOA}(\lambda,d)$ *variations with the detector index d can be approximated by the smoothed function of* $\overline{\rho}_{MERIS}^{TOA}(\lambda,d)$*).* We can indeed imagine that $\overline{\rho}_{TRUE}^{TOA}(\lambda,d)$ might not follow a perfectly smooth curve from one detector to the next due to a natural geophysical variability (e.g.: a coastline oriented in the along track direction). At first sight, it is difficult to estimate the uncertainty associated with this assumption. One way to do so however is to test the validity of assumption 2 in the along track direction. Indeed, whilst vertical stripping induced by detector-to-detector systematic radiometric differences is clearly

visible, the along track signal variations seems to be mostly governed by geophysical variations (see for instance *Figure 3*).

Assumption 3: The uncertainty $\sigma_{assumption3}(\lambda)$ associated to assumption 2 can be evaluated by assessing the validity of the to assumption 2 in the along track direction.

Let thus proceed by computing the mean across track reflectance and compute the difference to it smoothed version in the along track direction.
We compute the mean $\rho_{MERIS}^{TOA}(\lambda, f, d)$ along each frame *f*:

$$\bar{\rho}_{MERIS}^{TOA}(\lambda, f) = \frac{1}{f_{\max}} \sum_{d=1}^{d_{\max}} \rho_{MERIS}^{TOA}(\lambda, f, d)$$

Then we compute the smoothed along track value of $\bar{\rho}_{MERIS}^{TOA}(\lambda, f)$ which we write:

$$\bar{\rho}_{MERIS_SMOOTHED}^{TOA}(\lambda, f) = \frac{1}{N_{smooth}} \times \sum_{\varphi = f - \frac{N_{smooth}-1}{2}}^{\varphi = f + \frac{N_{smooth}-1}{2}} \bar{\rho}_{MERIS}^{TOA}(\lambda, \varphi - f) I_{N_{smooth}}(\varphi)$$

We illustrate this process in *Figure 13*.

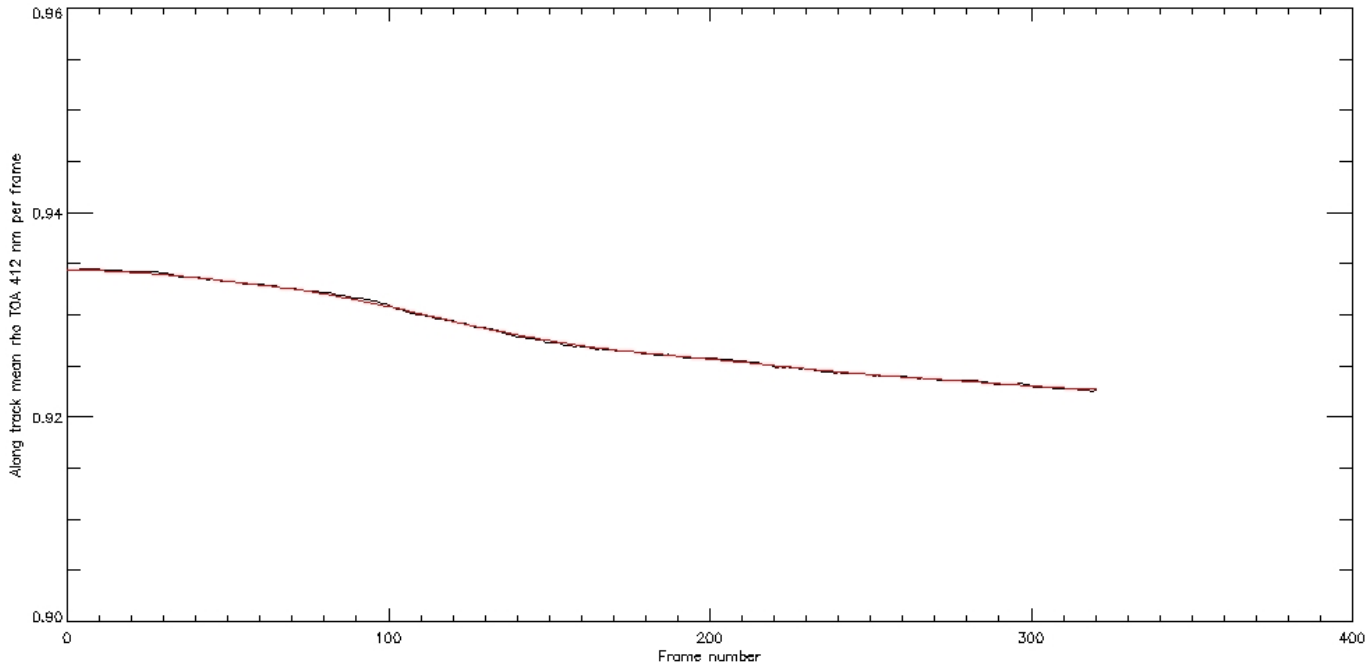

Figure 13: MER_RR__1PPBCM20070110_224832_000000562054_00330_25434_0058.N1
In black, the mean value of smile corrected reflectance at 412 nm for a given frame $\bar{\rho}_{MERIS}^{TOA}(\lambda, f)$ as a function of the detector index. In red the smoothed curve corresponding to $\bar{\rho}_{MERIS_SMOOTHED}^{TOA}(\lambda, f)$.

Looking at *Figure 13* we see that the mean frame $\overline{\rho}_{MERIS}^{TOA}(\lambda, f)$ and its smoothed version $\overline{\rho}_{MERIS_SMOOTHED}^{TOA}(\lambda, f)$ are nearly superimposed. This should be compared to what can be seen in *Figure 10*, there the detector-to-detector systematic radiometric differences are clearly visible. Qualitatively, we observe that the uncertainty associated to assumption 2 is low compared to the detector-to-detector systematic radiometric difference we are aiming at correcting. Quantitatively, we can estimate an upper value of $\sigma_{assumption3}(\lambda)$ by computing the standard deviation of the difference $\overline{\rho}_{MERIS}^{TOA}(\lambda, f) - \overline{\rho}_{MERIS_SMOOTHED}^{TOA}(\lambda, f)$

Now that all sources of uncertainties were identified, we can derive the total uncertainty associated with the equalization coefficients. Using the definition of $c_{eq}(\lambda, d)$, i.e., $c_{eq}(\lambda, d) = \frac{\overline{\rho}_{MERIS}^{TOA}(\lambda, d)}{\overline{\rho}_{TRUE}^{TOA}(\lambda, d)}$, and its logarithm derivative we can derive the total uncertainty associated to the retrieval of the equalization coefficients:

$$\frac{\Delta c_{eq}(\lambda, d)}{c_{eq}(\lambda, d)} = \frac{\Delta \overline{\rho}_{MERIS}^{TOA}(\lambda, d)}{\overline{\rho}_{MERIS}^{TOA}(\lambda, d)} + \frac{\Delta \overline{\rho}_{TRUE}^{TOA}(\lambda, d)}{\overline{\rho}_{TRUE}^{TOA}(\lambda, d)}$$

i.e.,

$$\frac{\Delta c_{eq}(\lambda, d)}{c_{eq}(\lambda, d)} = \frac{\sigma_{MERIS}(\lambda, d)}{\overline{\rho}_{MERIS}^{TOA}(\lambda, d)} + \frac{\sigma_{TRUE}(\lambda, d)}{\overline{\rho}_{TRUE}^{TOA}(\lambda, d)} + \frac{\sigma_{assumption3}(\lambda)}{\overline{\rho}_{TRUE}^{TOA}(\lambda, d)}$$

Or since $c_{eq}(\lambda, d)$ are very close to 1

$$\Delta c_{eq}(\lambda, d) \approx \frac{\Delta c_{eq}(\lambda, d)}{c_{eq}(\lambda, d)} \approx \frac{\sigma_{MERIS}(\lambda, d)}{\overline{\rho}_{TRUE}^{TOA}(\lambda, d)} + \frac{\sigma_{TRUE}(\lambda, d)}{\overline{\rho}_{TRUE}^{TOA}(\lambda, d)} + \frac{\sigma_{assumption3}(\lambda)}{\overline{\rho}_{TRUE}^{TOA}(\lambda, d)}$$

Hereafter, we illustrate the process of the computation of the uncertainties associated to the equalization coefficients with the plot of these uncertainties for a given L1b product and a given band, 412 nm.

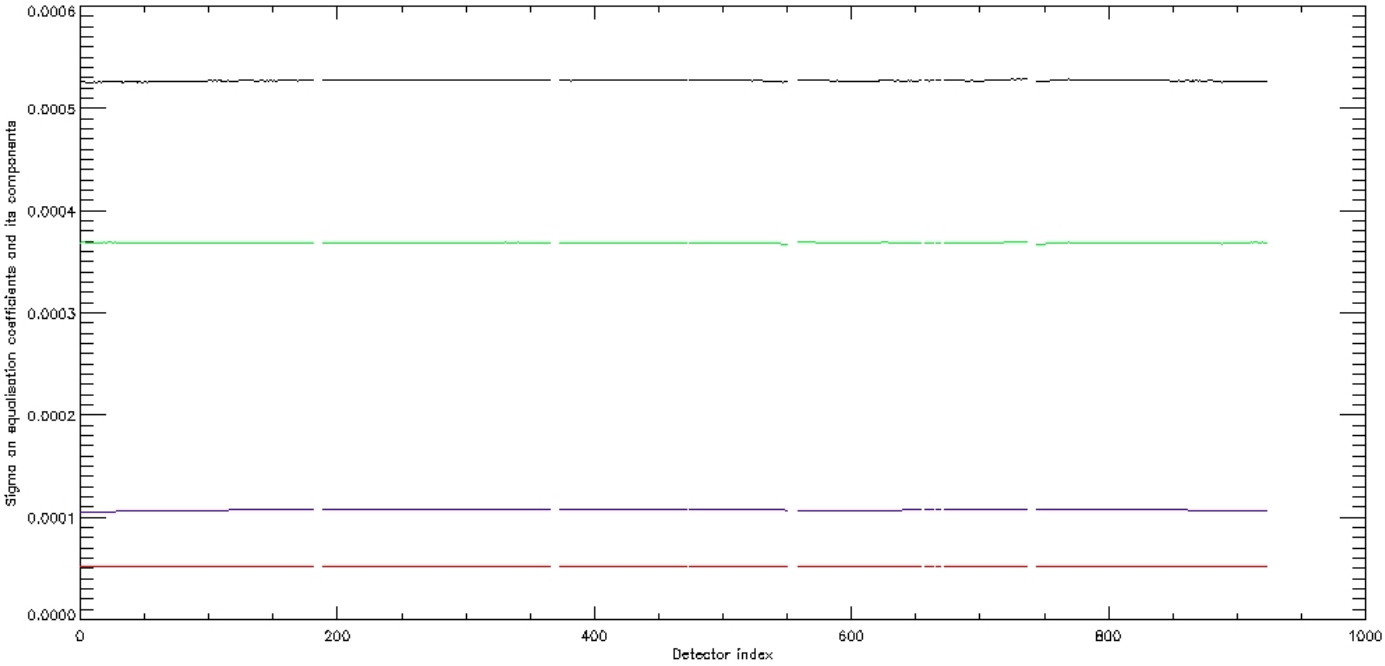

Figure 14: MER_RR__1PPBCM20070110_224832_000000562054_00330_25434_0058.N1
In black to total uncertainty associated with equalization coefficients at 412 nm
$\Delta c_{eq}(\lambda,d) \approx \frac{\sigma_{MERIS}(\lambda,d)}{\overline{\rho}_{TRUE}^{TOA}(\lambda,d)} + \frac{\sigma_{TRUE}(\lambda,d)}{\overline{\rho}_{TRUE}^{TOA}(\lambda,d)} + \frac{\sigma_{assumption3}(\lambda)}{\overline{\rho}_{TRUE}^{TOA}(\lambda,d)}$. *In green, the first component of the total uncertainty,* $\frac{\sigma_{MERIS}(\lambda,d)}{\overline{\rho}_{TRUE}^{TOA}(\lambda,d)}$, *in red, the second component,* $\frac{\sigma_{TRUE}(\lambda,d)}{\overline{\rho}_{TRUE}^{TOA}(\lambda,d)}$, *and in blue the third component* $\frac{\sigma_{assumption3}(\lambda)}{\overline{\rho}_{TRUE}^{TOA}(\lambda,d)}$.

As a final result, for a single L1b scene over Antarctica and a given spectral band, we obtain the equalization coefficients and the uncertainties associated to them (see for instance *Figure 15*)

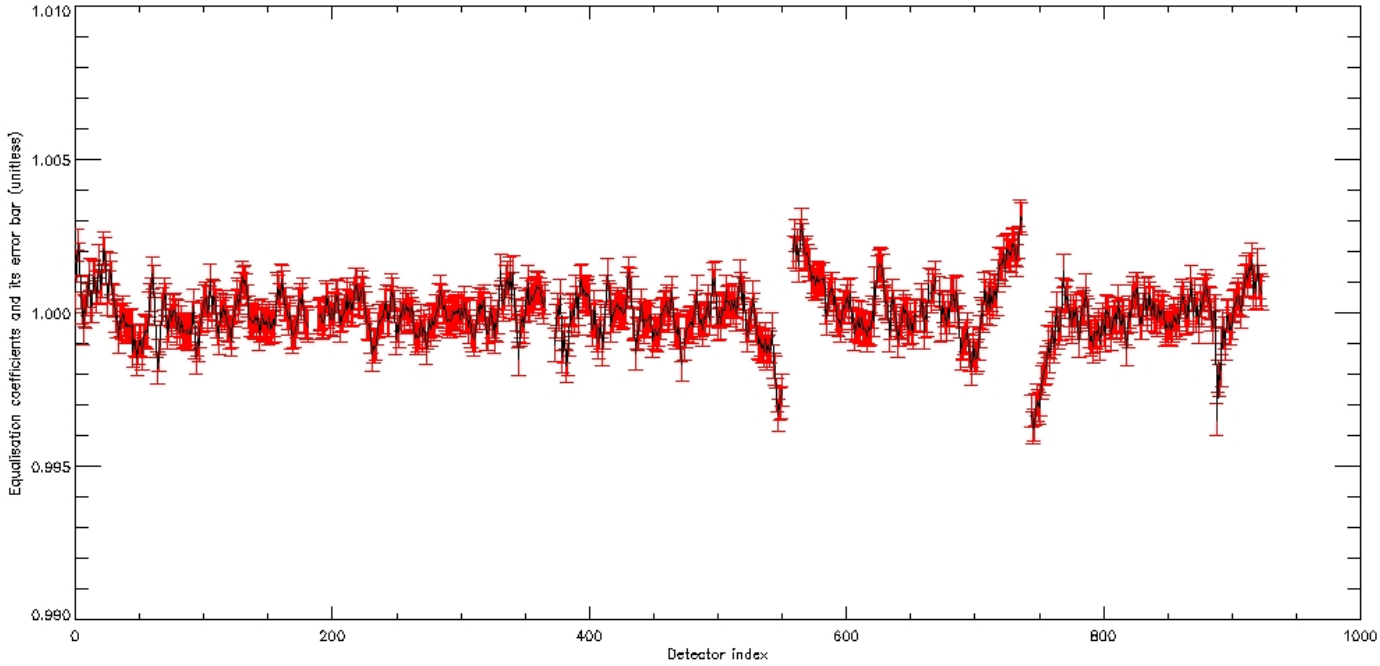

Figure 15: MER_RR__1PPBCM20070110_224832_000000562054_00330_25434_0058.N1
In black the equalization coefficients at 412 nm and in red their associated uncertainties

3.3 Combining equalization coefficients retrieved from a large number of Antarctica scenes across the full mission

In the previous sections, we have retrieved the $c_{eq}(\lambda,d)$ for a single scene. In this section, we analyse the result of generating $c_{eq}(\lambda,d)$ from a large number of scenes (104 in total). The objective of this approach is to understand what the temporal variability of the $c^{i}_{eq}(\lambda,d)$, where i is the index associate to a scene, and consequently design an optimal methodology for equalization based on these $c^{i}_{eq}(\lambda,d)$.

3.3.1 Are the equalization coefficients time dependant?

We previously described how for a single scene i we can derive a set of equalization coefficients $c^{i}_{eq}(\lambda,d)$ and the associated uncertainties $\Delta c^{i}_{eq}(\lambda,d)$. A question arises: are the equalization coefficients constant in time as a first visual inspection would suggest?
We answer this question by computing the (Pearson) correlation coefficients for each band and each detector between the $c^{i}_{eq}(\lambda,d)$ and time elapsed since the beginning of the MERIS mission.

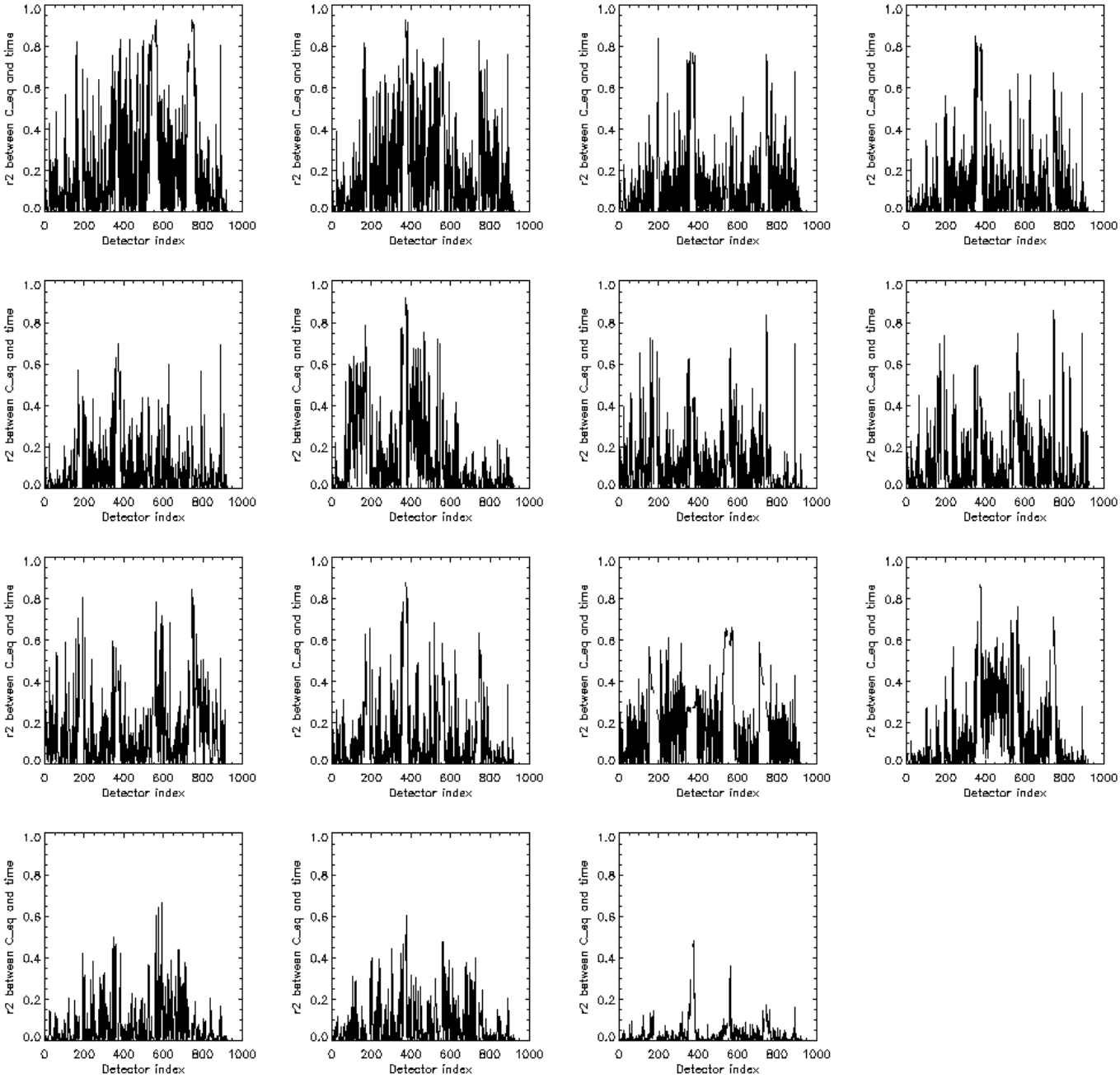

Figure 16: the r^2 correlation coefficients between $c_{eq}^{i}(\lambda, d)$ and time elapsed since the beginning of the MERIS mission, from the left to right and top to bottom, for each spectral band (λ = 1 to 15).

A close inspection of *Figure 16* reveals that:

- The correlation coefficients seem to generally decrease with increasing wavelength. In band 15, the variation of the $c_{eq}^{i}(\lambda, d)$ appears only loosely time dependant whereas in band 1 and 2, there is a significant time dependence for many detectors.
- In many instances the correlation between $c_{eq}^{i}(\lambda, d)$ and time is maximum at camera interfaces (each camera as 185 detectors), suggesting at camera interface radiometric differences evolving with time.

As far as band 11 is concerned, not only is our methodology not applicable because we did not correct the L1b data for smile in this band, but also the spectral position of the band has changed at the end of 2002.

3.3.2 Modelling the equalisation coefficients time dependency with a 2nd order polynomial

In Figure 17, we show two examples of equalisation coefficients retrieval, for 2 different RR detectors, at 412 nm, for 104 scenes acquired during the MERIS mission. A time variation is clearly visible in one of the two cases (for RR detector 750).

Assumption 4: A second order polynomial fit is sufficient capture the $c_{eq}^{i}(\lambda, d)$ ***time variation:***

$$c_{eq}^{i}(\lambda, d) = c_{eq}(\lambda, d, t_i) = c_{eq}^{t=0}(\lambda, d) + \frac{\partial c_{eq}(\lambda, d, t)}{\partial t} t_i + \frac{\partial^2 c_{eq}(\lambda, d, t)}{\partial t^2} t_i^2$$

With t=0 corresponding to 01/04/2002.

In our assessment of uncertainties associated with the $c_{eq}^{i}(\lambda, d)$ (see section 3.2.4) we showed that:

- The retrieval of the $c_{eq}^{i}(\lambda, d)$ can be considered insensitive to systematic errors at $\rho_{MERIS}^{TOA}(\lambda, f, d)$ level. The retrieval of the $c_{eq}^{i}(\lambda, d)$ can thus be considered unbiased.
- The uncertainty associated to the $c_{eq}^{i}(\lambda, d)$ is derived from the $\rho_{MERIS}^{TOA}(\lambda, f, d)$ error which we assumed to be modelled by a normal distribution. It should thus be random as well.

The condition to apply the weighted least square formalism to our problem are fulfilled. In Figure 17 the result of the fitting and the associated uncertainties polynomial coefficients (1-sigma) is superimposed on the $c_{eq}^{i}(\lambda, d)$ time variations (in practice we used the IDL poly_fit.pro routine to perform the fit).

It is remarkable to see that our evaluation of the uncertainty associated to the retrieval of the $c_{eq}^{i}(\lambda, d)$ at each date is such that it just allows a 2nd order polynomial to fit the time series. This is an *a posteriori* indication that the assumption 4 is justified.

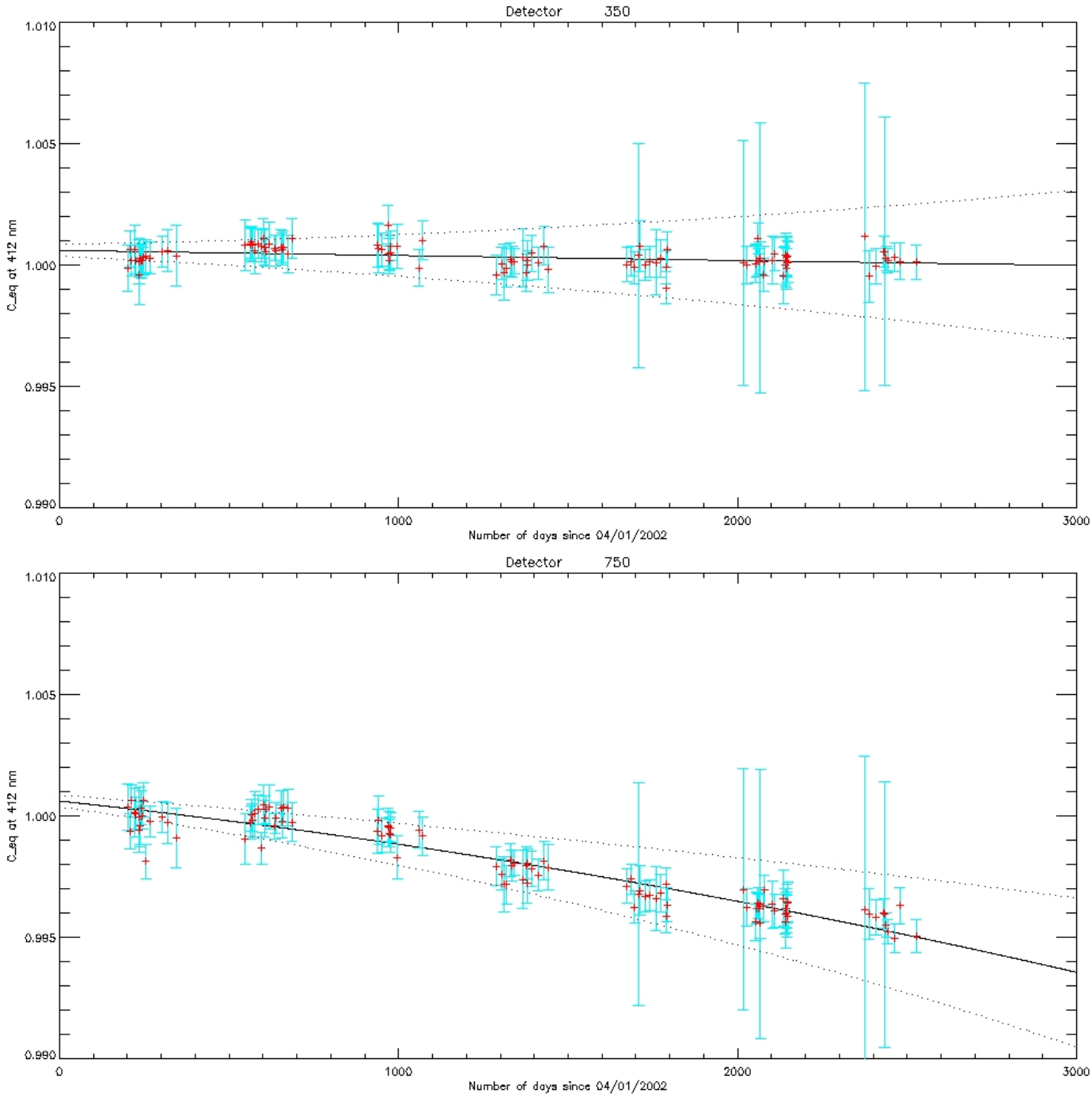

Figure 17: In red crosses, the $c_{eq}^{i}(\lambda, d)$ at λ =412 nm for detector d=350 (top panel) and d=750 (bottom panel) and their associated uncertainties (cyan error bars). The black line is the second order polynomial weighted least square fit and the associated 1-sigma uncertainty (dotted line)

4 Results

4.1 The equalization coefficients

We present in the following Figure 18 to Figure 20 the coefficients $c_{eq}^{t=0}(\lambda,d)$, $\frac{\partial c_{eq}(\lambda,d,t)}{\partial t}$, $\frac{\partial^2 c_{eq}(\lambda,d,t)}{\partial t^2}$ resulting from the fit for all bands and for all RR detectors.

Few remarks on the $c_{eq}^{t=0}(\lambda,d)$ in Figure 18:

- There seem to be a general trend of increase detector-to-detector variations of $c_{eq}(\lambda,d)$ with λ
- The $c_{eq}(\lambda,d)$ are largest at camera boundaries
- $c_{eq}(11,d)$ behaves differently from other bands as expected, in particular t camera boundaries. Again it should be reminded that band 11 was not smile corrected, that the spectral configuration changed at the end of 2002 and that consequently our methodology is not adapted to this band.

Few remarks on the $\frac{\partial c_{eq}(\lambda,d,t)}{\partial t}$ and $\frac{\partial^2 c_{eq}(\lambda,d,t)}{\partial t^2}$ respectively shown in Figure 19 and Figure 20 :

- Time dependencies are strongest at camera interfaces suggesting that the existence of temporally variable at camera interface radiometric differences.
- There is no obvious wavelength dependency.

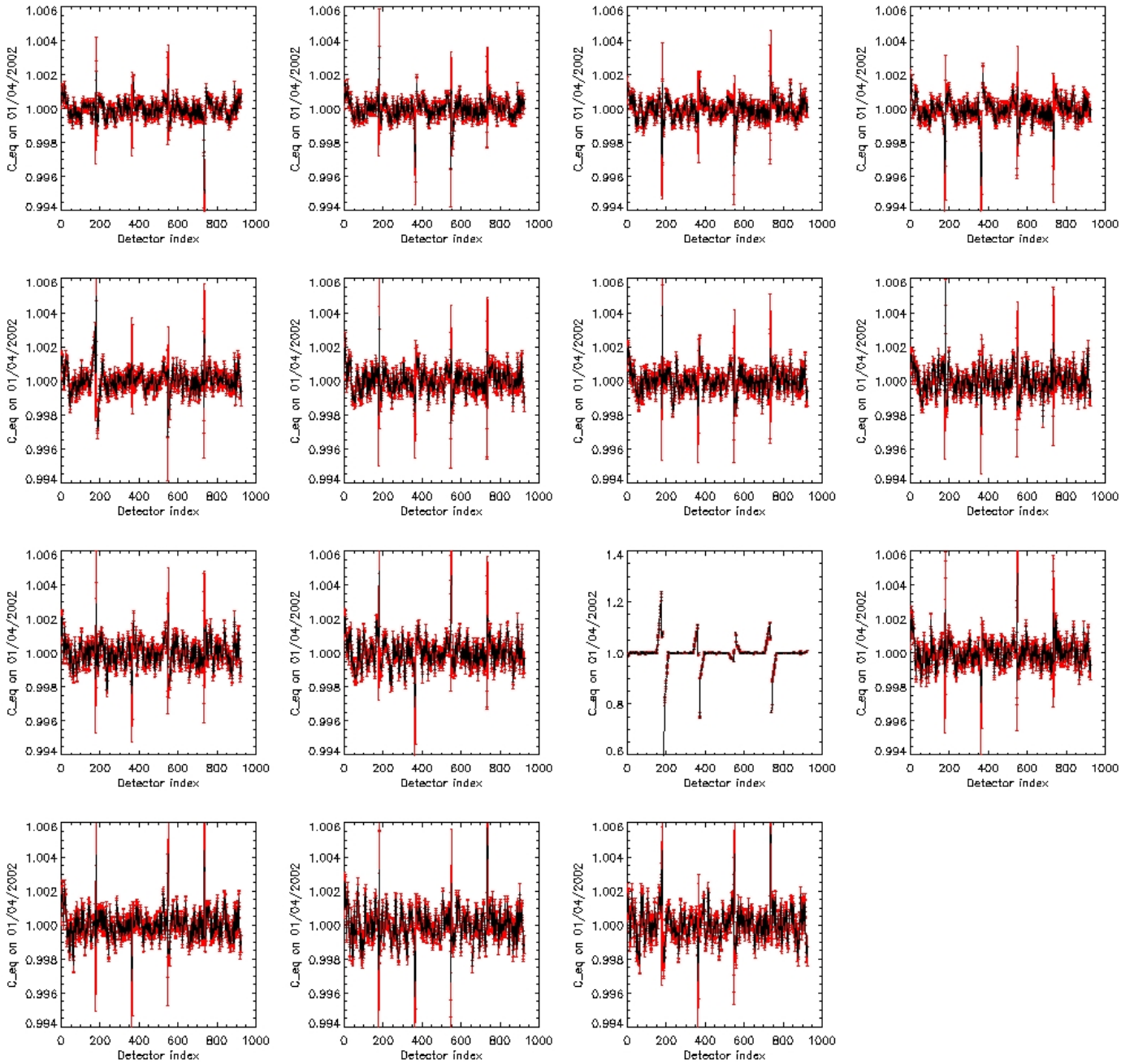

Figure 18: $c_{eq}^{t=0}(\lambda, d)$ *(black line) with its associated uncertainty (red error bars), from the left to right and top to bottom, for each spectral band (* λ *= 1 to 15).*

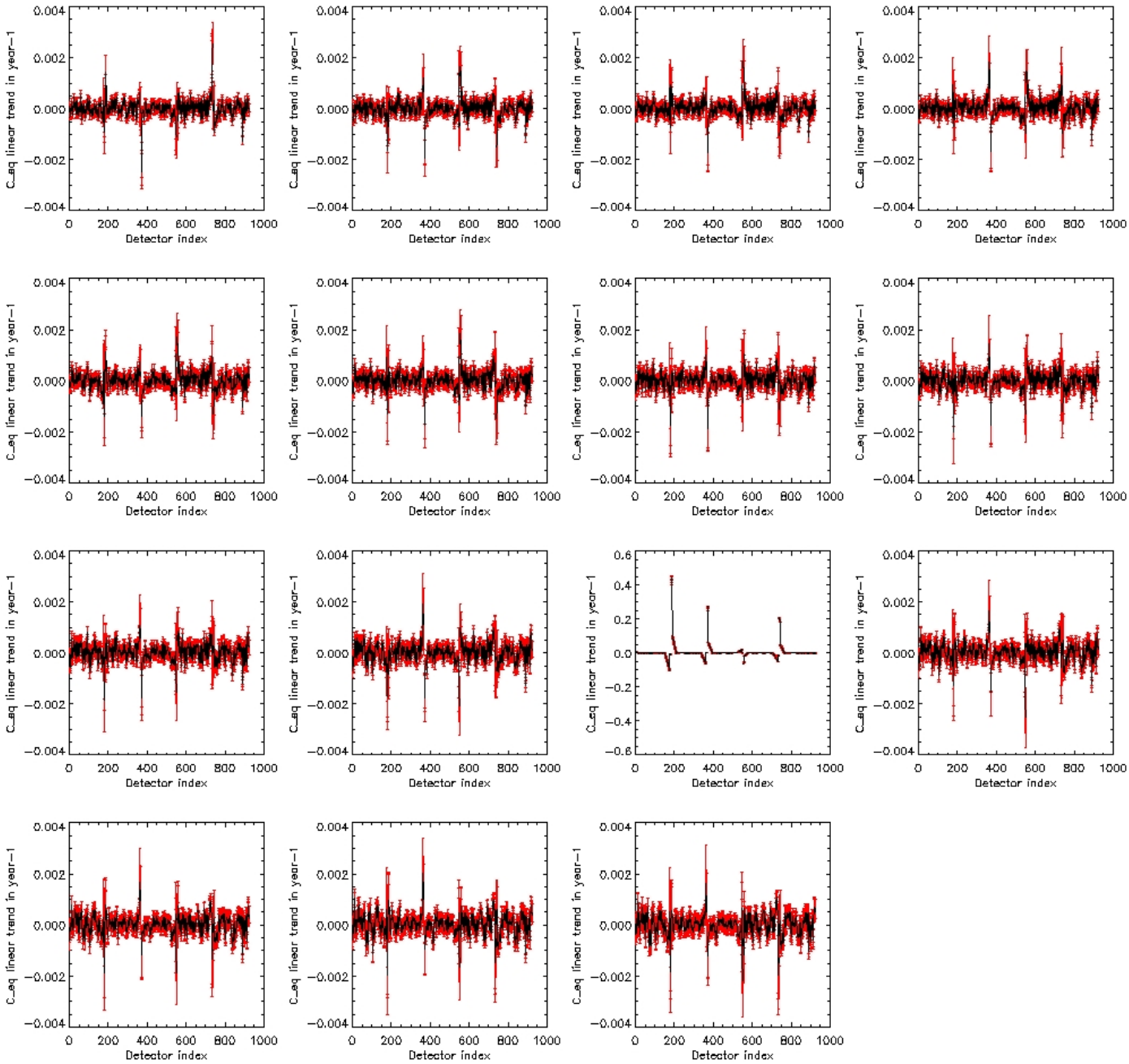

Figure 19: the linear trend on $c_{eq}(\lambda,d)$, $\frac{\partial c_{eq}(\lambda,d,t)}{\partial t}$, *in year*$^{-1}$ *(black line) with its associated uncertainty (red error bars), from the left to right and top to bottom, for each spectral band (* λ *= 1 to 15).*

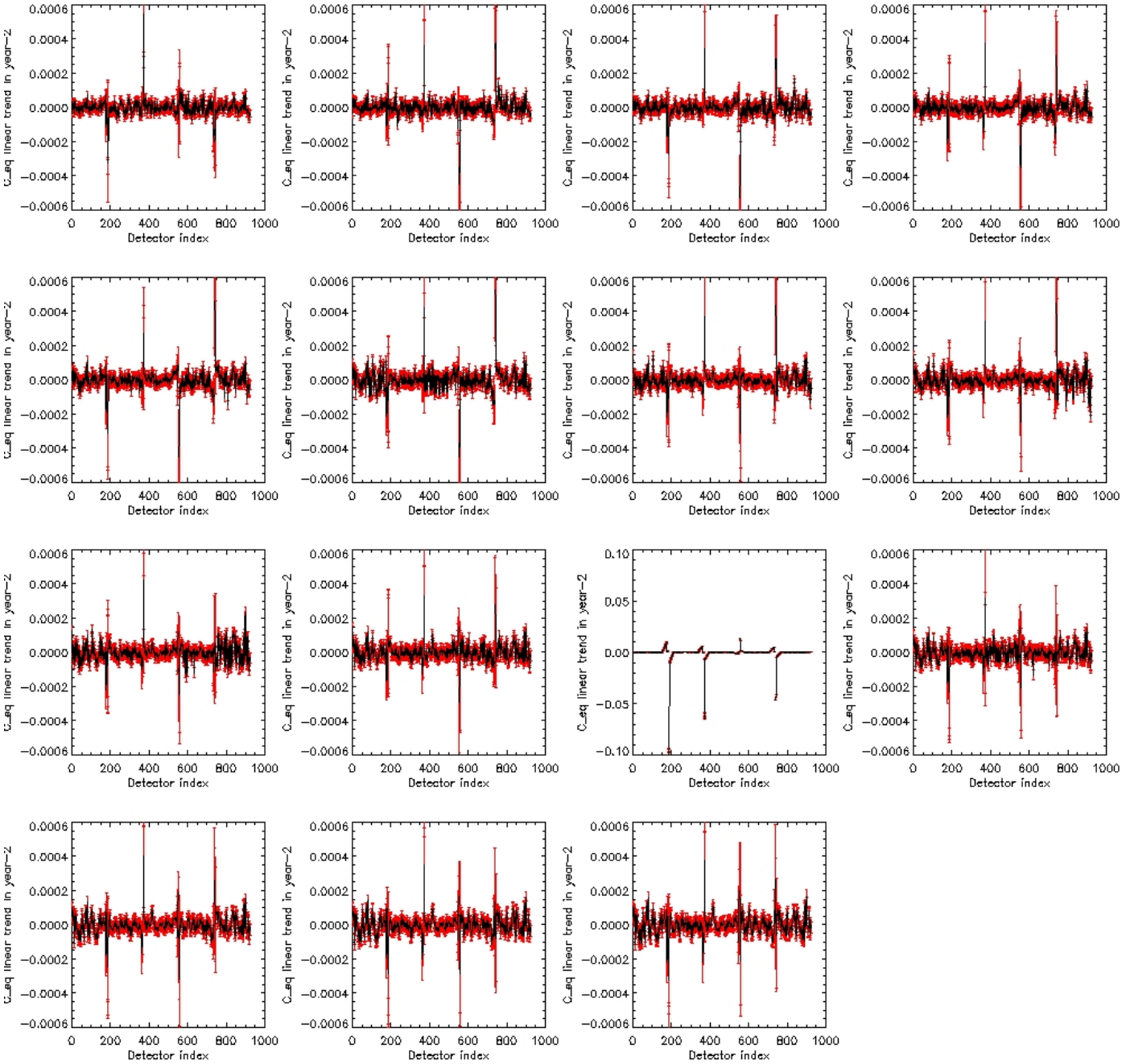

Figure 20: the quadratic trend on $c_{eq}(\lambda,d)$, $\frac{\partial^2 c_{eq}(\lambda,d,t)}{\partial t^2}$, *in year*$^{-2}$ *(black line) with its associated uncertainty (red error bars), from the left to right and top to bottom, for each spectral band (* λ *= 1 to 15).*

5 Verification

5.1 How to quantitatively measure the improvements brought by the equalization correction?

Our equalisation correction is based on the assumption of smoothness of the geophysical TOA signal across and along track (assumption 2). We showed for instance in Figure 13 that this assumption is well justified in the along track direction (frame-to-frame) but not across track (see Figure 10).

A criteria of success for the equalization is that the across track detector-to-detector systematic radiometric differences after equalization should be of the same order than the along track frame-to-frame noise. We derive proxies for these two quantities on an image basis by:

1. Computing the standard deviation $\sigma_{\text{detector}}(\lambda)$ of the quantity $\frac{\overline{\rho}^{TOA}_{MERIS}(\lambda,d)-\overline{\rho}^{TOA}_{MERIS_SMOOTHED}(\lambda,d)}{\overline{\rho}^{TOA}_{MERIS_SMOOTHED}(\lambda,d)}$ along track (see these variables on Figure 10). This is a proxy for the detector-to-detector systematic radiometric differences.
2. Computing the standard deviation $\sigma_{frame}(\lambda)$ of the quantity $\frac{\overline{\rho}^{TOA}_{MERIS}(\lambda,f)-\overline{\rho}^{TOA}_{MERIS_SMOOTHED}(\lambda,f)}{\overline{\rho}^{TOA}_{MERIS_SMOOTHED}(\lambda,f)}$ along track (see these variables on Figure 13). This is a proxy for the frame-to-frame noise.

The two proxies are derived similarly although they characterise noises of quite different nature: whilst in the across track direction the detector-to-detector differences are systematic, the along track frame-to-frame noise seems to be random.

In order to perform a quantitative assessment of the equalization procedure, we have selected 101 L1b scenes over Antarctica as a verification dataset. All scenes are nearly cloudless and the equalization coefficients were applied to them, after smile correction, in the following way for each acquisition *i*:

1. First $c_{eq}(\lambda,d,t_i)=c_{eq}^{t=0}(\lambda,d)+\frac{\partial c_{eq}(\lambda,d,t)}{\partial t}t_i+\frac{\partial^2 c_{eq}(\lambda,d,t)}{\partial t^2}t_i^2$ is computed for each band, detector using the coefficients $c_{eq}^{t=0}(\lambda,d)$, $\frac{\partial c_{eq}(\lambda,d,t)}{\partial t}$, $\frac{\partial^2 c_{eq}(\lambda,d,t)}{\partial t^2}$
2. Second, the corrected band is obtained via $\rho^{TOA}_{TRUE}(\lambda,x,y)=\frac{\rho^{TOA}_{MERIS}(\lambda,x,y)}{c_{eq}(\lambda,d=f(x,y),t_i)}$

It should be noted that the 101 L1b products in the verification dataset are different from the 104 L1b that were use to retrieve the equalization coefficients, although they span over the same period of time and cover the same geographic area.

In Figure 21, we have plotted the proxies $\sigma_{\text{detector}}(\lambda)$ and $\sigma_{frame}(\lambda)$ before and after equalization for the L1b products in the verification dataset. Several observations can be made:

- $\sigma_{detector}(\lambda)$ is generally reduced by the after equalization
- $\sigma_{frame}(\lambda)$ remains unchanged by the equalization process and corresponds to generally less than 0.1% of the TOA reflectance.
- $\sigma_{detector}(\lambda)$ after equalization is about twice $\sigma_{frame}(\lambda)$ and generally remains below 0.2% of the TOA reflectance.
- $\sigma_{detector}(\lambda)$ for equalized L1b remains constant throughout the mission whilst it increases with time for non equalized L1b products.

In Figure 22, we focus on the last point. We plot the proxy for the reduction of detector-to-detector systematic differences, defined as:

$$DetectorNoiseReduction = \frac{\sigma_{detector}^{before_equalization}(\lambda) - \sigma_{detector}^{after_equalization}(\lambda)}{\sigma_{detector}^{after_equalization}(\lambda)} \times 100$$

We notice that:

- The reduction of detector-to-detector systematic differences is generally of at least 10 % on average
- For all bands but band 15 (and 11), as time goes, the detector-to-detector systematic differences reduction is significant, starting at about 10 % at the beginning of the mission and reaching up to 100 % for data from 2009.

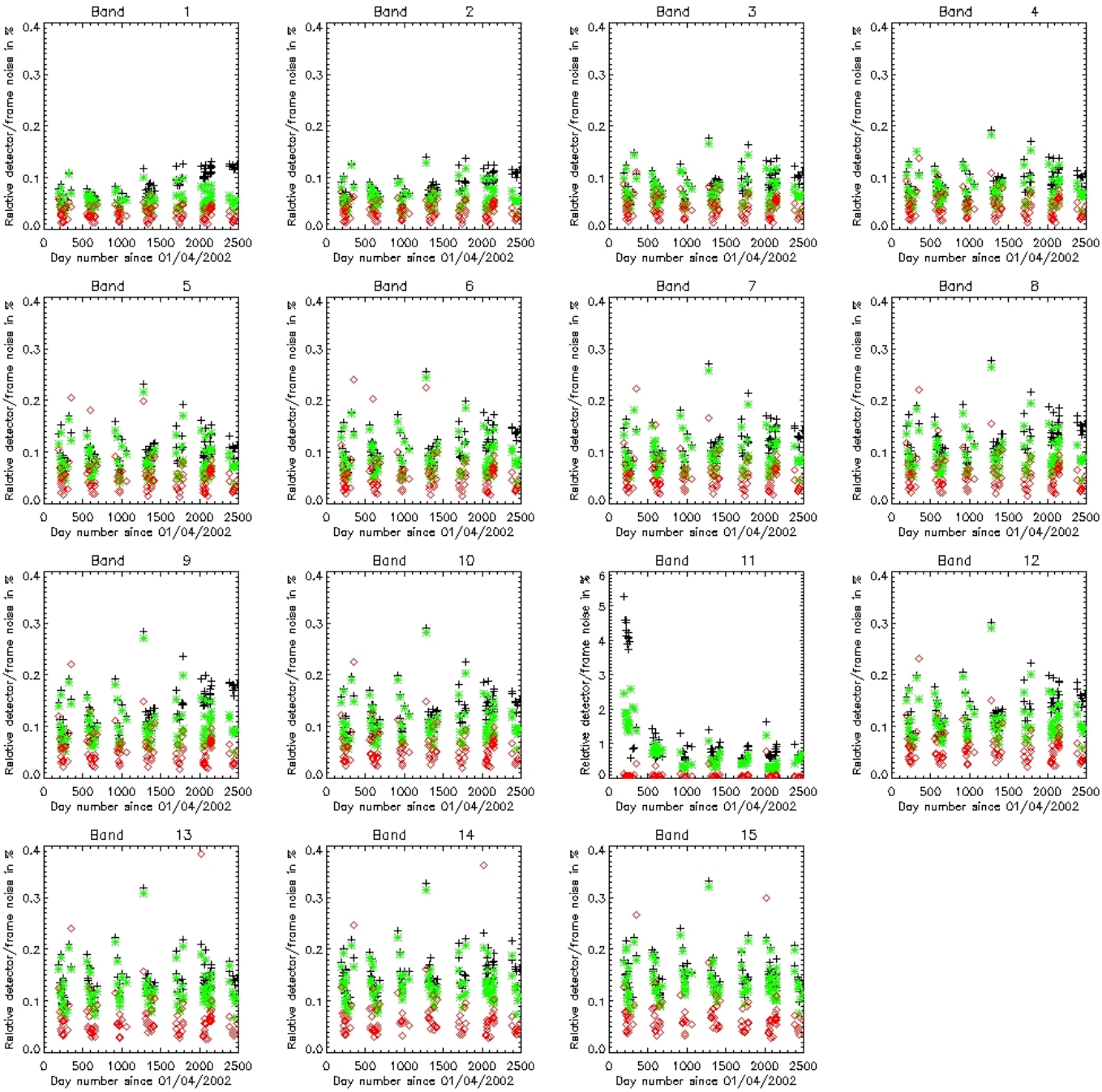

Figure 21: $\sigma_{frame}(\lambda)$ (in red diamonds), $\sigma_{detector}(\lambda)$ before equalization (in black crosses) and $\sigma_{detector}(\lambda)$ after equalisation (in green stars) all expressed in % for 101 scenes over Antarctica.

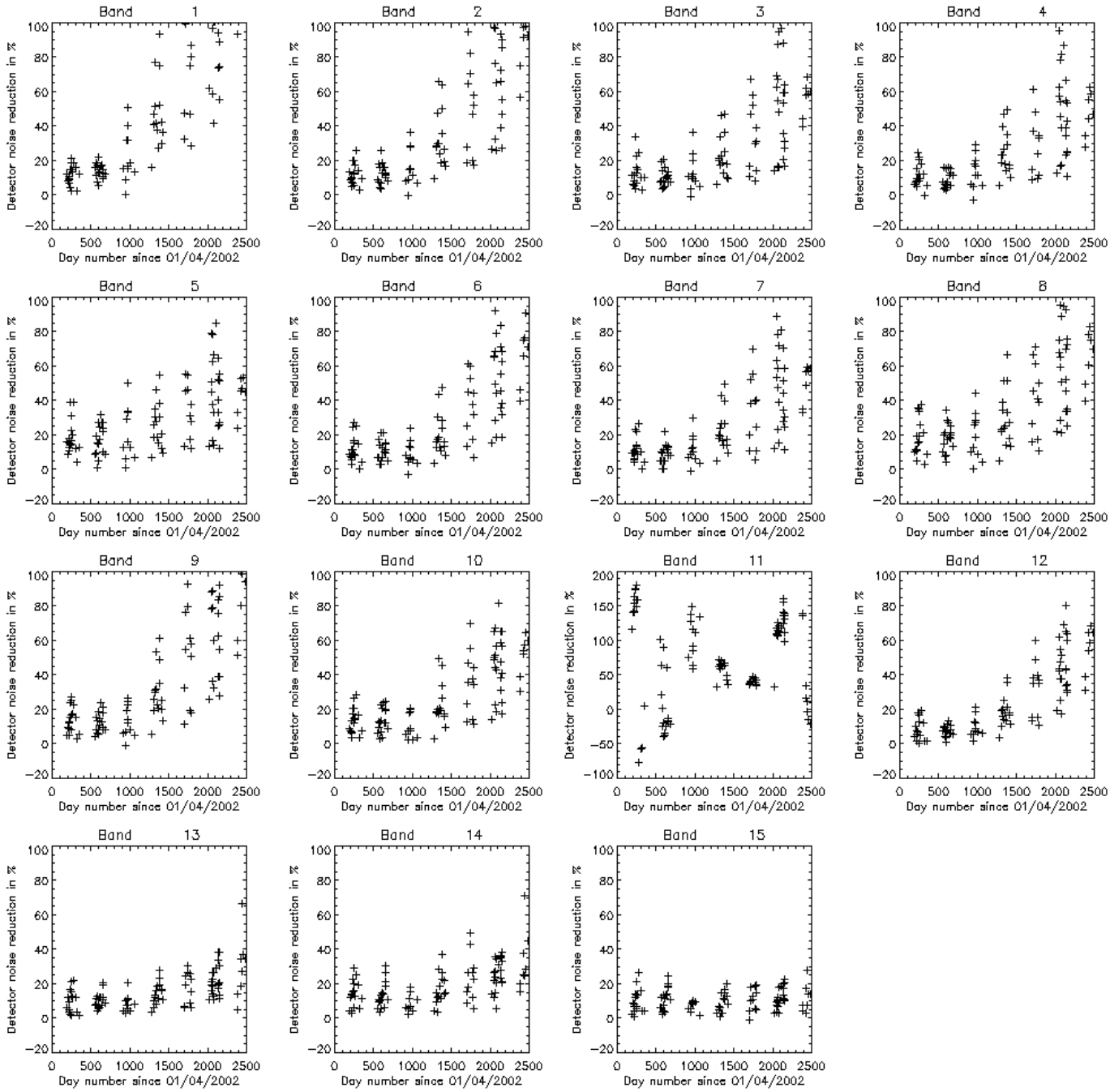

Figure 22: the noise reduction induced by the equalization for 101 scenes over Antarctica. The detector noise reduction is expressed as ($\sigma_{detector}(\lambda)$ before equalization - $\sigma_{detector}(\lambda)$ after equalisation)/ $\sigma_{detector}(\lambda)$ after equalization x 100.

5.2 Focusing on intra camera and inter camera effects

We can distinguish two groups of equalization coefficients depending on their location across the swath with respect to camera interfaces:

1. Group 1: The retrieval of the equalization coefficients is such that in the vicinity of a camera interface, i.e., from $\frac{N_{smooth}-1}{2}$ detectors before a camera interface to $\frac{N_{smooth}-1}{2}$ detectors after this camera interface, the coefficients are sensitive to the at camera interface radiometric offsets (see definition of equalization coefficients in section 3.2.1)
2. Group 2: On the other hand, the retrieval of the equalization coefficients for detectors located $\frac{N_{smooth}-1}{2}$ detectors after a camera interface and $\frac{N_{smooth}-1}{2}$ detectors before the next one is NOT sensitive to the at camera interface systematic radiometric differences. It is only sensitive to the detector-to-detector systematic radiometric differences.

The evolution of at camera interface radiometric differences can be monitored with equalization coefficients from group 1. The evolution of detector-to-detector radiometric differences can be monitored with equalization coefficients from group 2. In the previous Figure 21 and Figure 22, these two groups were together. In the next 2 section we look at equalization coefficients from group 1 and 2 seperately.

5.2.1 Monitoring the evolution of at camera interface radiometric differences

For a reason that we do not understand, there are detectors close to the camera interfaces that are not systematically used in the resampling of the L1b over Antarctica. Figure 23 shows an example at camera interface 2-3 for which the equalization coefficients could not be determined after 2004 because no data coming from detector 372 was present.

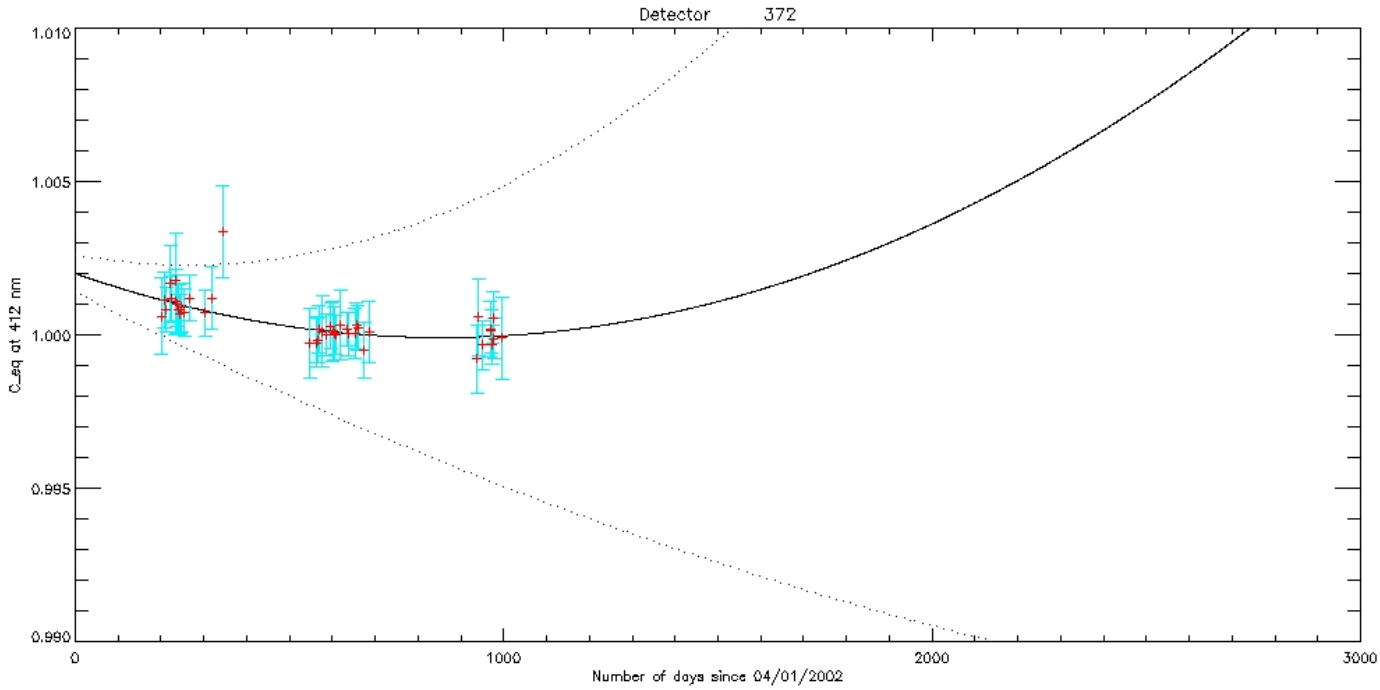

Figure 23: In red crosses, the $c_{eq}^{i}(\lambda, d)$ at λ =412 nm for detector d=372 and their associated uncertainties. The black line is the second order polynomial weighted least square fit and the associated 1-sigma uncertainty (dotted line)

The fit of this time series of equalization coefficients result into large uncertainties for the equalization coefficient in 2009. This will be an issue if we use the equalization coefficient at this detector to characterize the at camera interface radiometric differences. We use instead the equalization coefficients for which the detector are the closest to the camera interface and have data from 2002 to 2009 to perform the fit of the equalization coefficient. We end up with the following selection of RR detectors: 176 and 189 to assess the radiometric differences at camera 1 and 2 interface, 362 and 373 to assess the radiometric differences at camera 2 and 3 interface, 545 and 559 to assess the radiometric differences at camera 3 and 4 interface and 731 and 744 to assess the radiometric differences at camera 4 and 5 interface. As a proxy for the at camera interface radiometric difference we have for instance for interface between camera 2 and 3:

$$\Delta c_{eq}^{camera2-3}(\lambda, t_i) = c_{eq}(\lambda, 362, t_i) - c_{eq}(\lambda, 373, t_i)$$
$$= \left(c_{eq}^{t=0}(\lambda, 362) - c_{eq}^{t=0}(\lambda, 373)\right) + \left(\frac{\partial c_{eq}(\lambda, 362, t)}{\partial t} - \frac{\partial c_{eq}(\lambda, 373, t)}{\partial t}\right) t_i + \left(\frac{\partial^2 c_{eq}(\lambda, 362, t)}{\partial t^2} - \frac{\partial^2 c_{eq}(\lambda, 373, t)}{\partial t^2}\right) t_i^2$$

In Figure 24 to Figure 27 we plot the difference between the equalization coefficients on each side of the 4 camera interfaces, for each spectral band. Again, the result for band 11 should simply not be interpreted (nor looked at).
We make the following observations:

- At launch time (t0=01/04/2002), the difference at camera interface is below 0.003 (i.e. 0.3% at TOA reflectance level) for all bands and all camera interfaces except camera transition 1-2 in band 5 and 15 where it reaches 0.005 (i.e. 0.5% at TOA reflectance level).
- There is a general tendency towards a larger spectral spread at each camera interface reaching 0.01 (i.e., 1 % at TOA reflectance level)

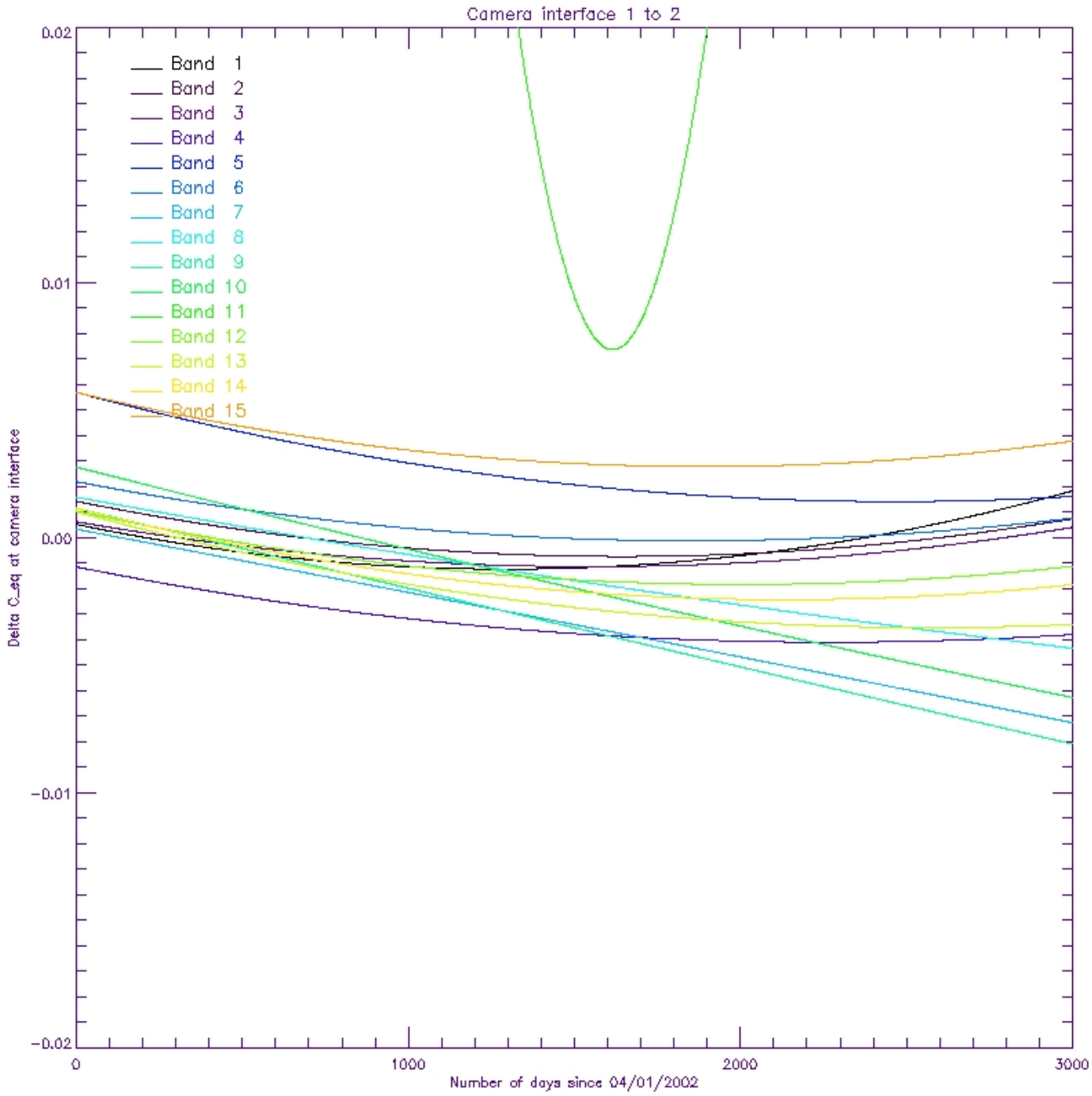

Figure 24: Time variations of the difference between the equalization coefficients before and after the camera interface 1-2. A difference of 0.01 at a camera interface between the equalization coefficients implies a 1 % difference at TOA reflectance level in a L1b product before equalization correction.

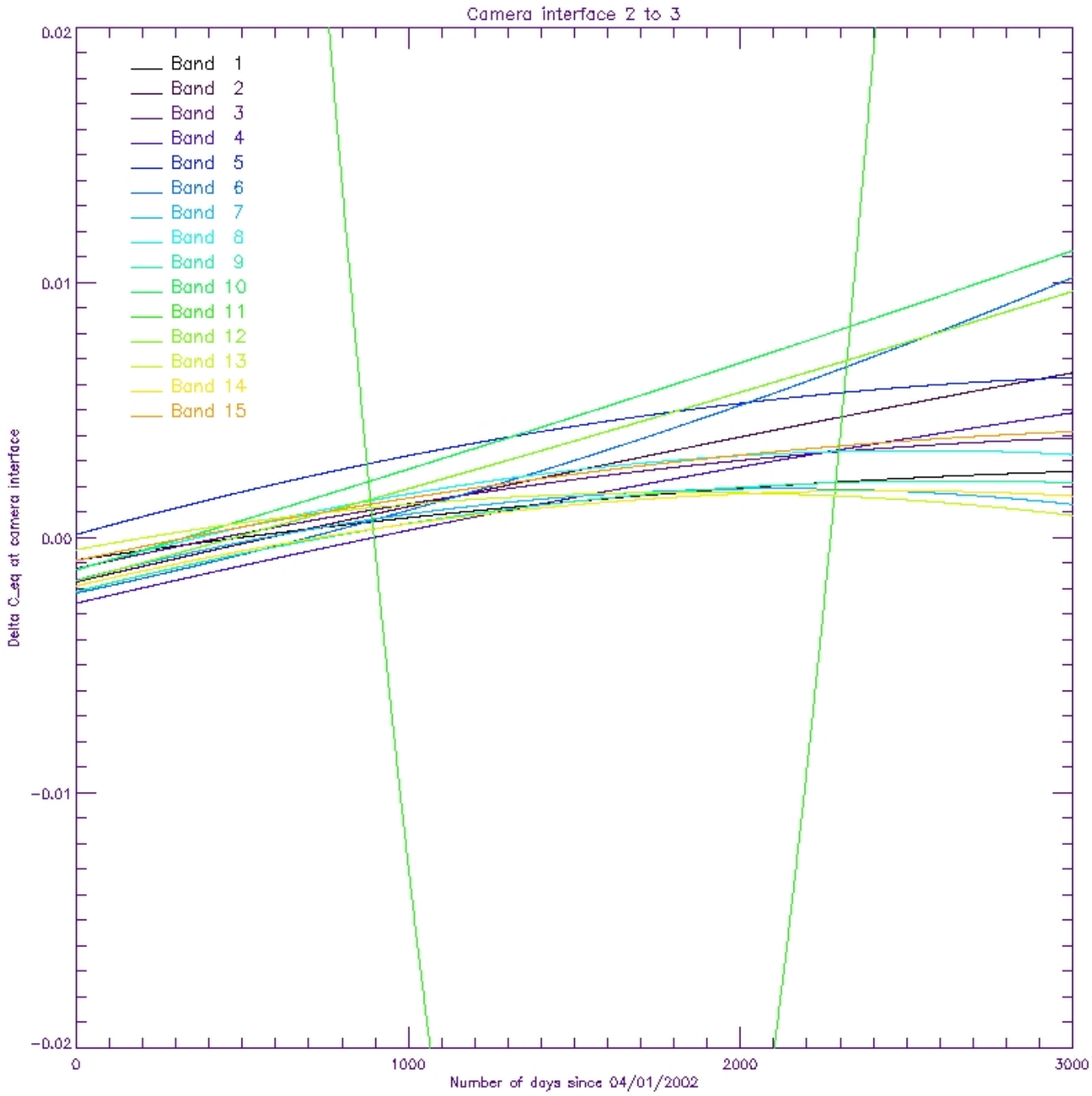

Figure 25: Time variations of the difference between the equalization coefficients before and after the camera interface 2-3. A difference of 0.01 at a camera interface between the equalization coefficients implies a 1 % difference at TOA reflectance level in a L1b product before equalization correction.

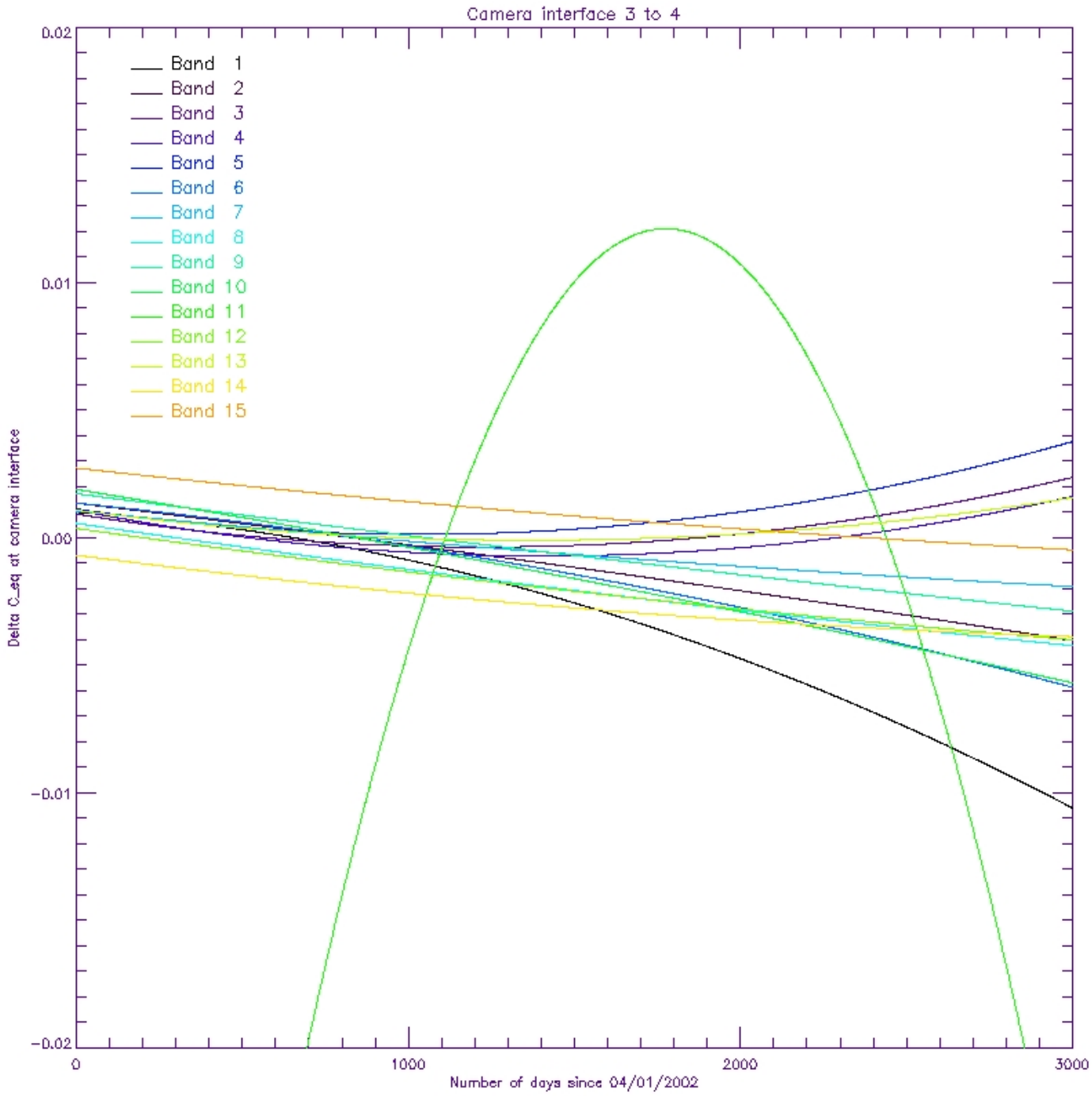

Figure 26: Time variations of the difference between the equalization coefficients before and after the camera interface 3-4. A difference of 0.01 at a camera interface between the equalization coefficients implies a 1 % difference at TOA reflectance level in a L1b product before equalization correction.

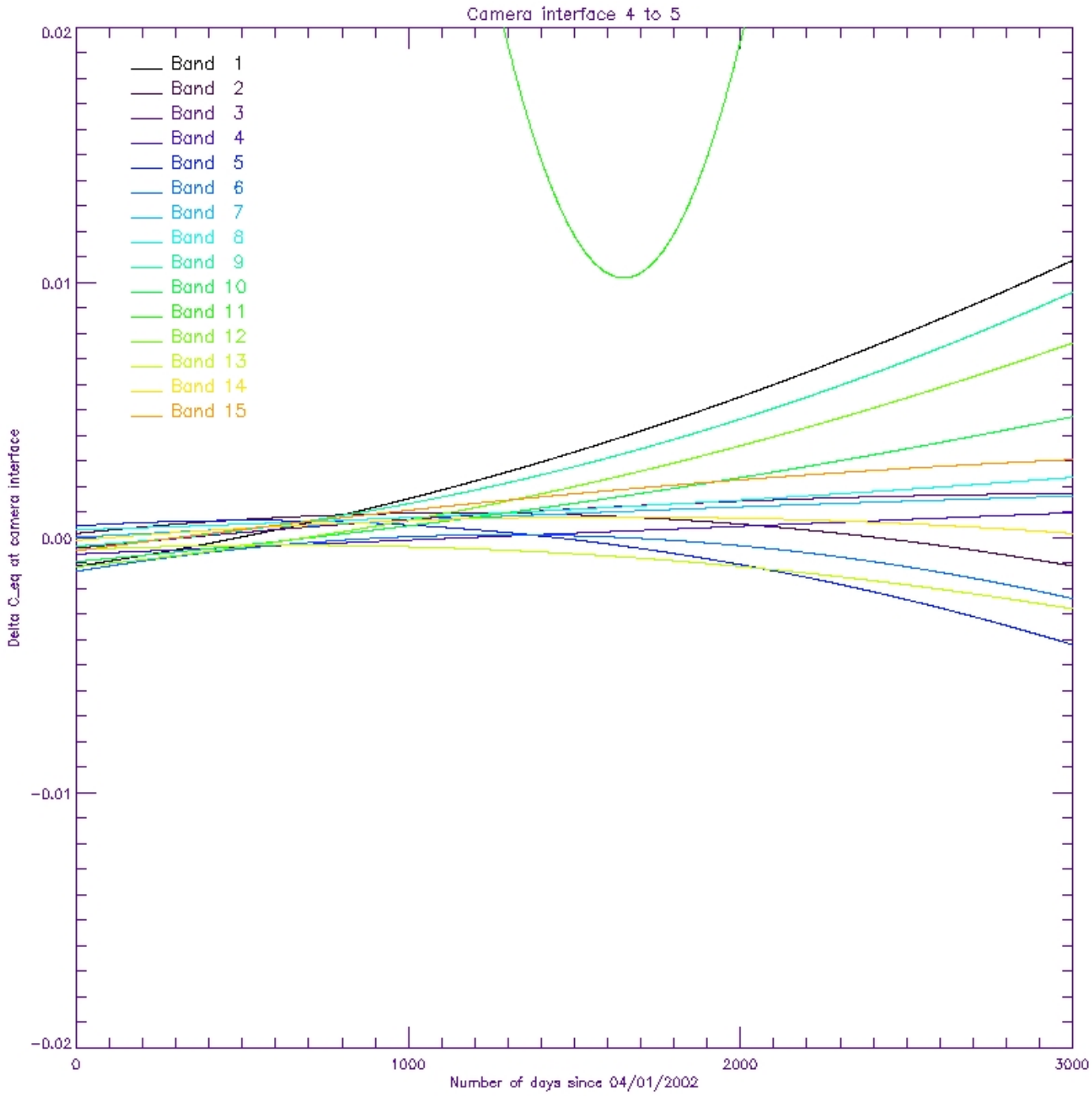

Figure 27: Time variations of the difference between the equalization coefficients before and after the camera interface 4-5. A difference of 0.01 at a camera interface between the equalization coefficients implies a 1 % difference at TOA reflectance level in a L1b product before equalization correction.

5.2.2 Monitoring the evolution of intra camera detector-to-detector systematic radiometric differences

In this section we focus on the equalization coefficient from the group 2, i.e., those that are only sensitive to the detector-to-detector systematic radiometric and not to at camera interface radiometric differences. The results are shown in Figure 28 and Figure 29. We make the same observations we did on similar plots where the equalization coefficients from group 1 and 2 were kept together (see section 5.1).

N.B.: We actually further restrict the number of detectors in group 2 when computing $\sigma_{detector}(\lambda)$ by extending the exclusion zone around the camera interface to $N_{smooth}-1$ detectors instead of $\frac{N_{smooth}-1}{2}$ detectors. This is necessary because in the equalized products the influence of a camera interface extends to $\frac{N_{smooth}-1}{2}$ detectors from the camera interface via the equalization coefficients. To fully remove camera interface incluences in $\sigma_{detector}(\lambda)$ computed over equalized products, we thus only use $N_{smooth}-1$ detector from a camera interface. For original (non equalized) L1b products, $\sigma_{detector}(\lambda)$ can be computed over the detectors from group 2 but for consistency in our comparison, we also use a restricted group 2 with an exclusion zone around the camera interface of $N_{smooth}-1$ detectors instead of $\frac{N_{smooth}-1}{2}$ detectors.

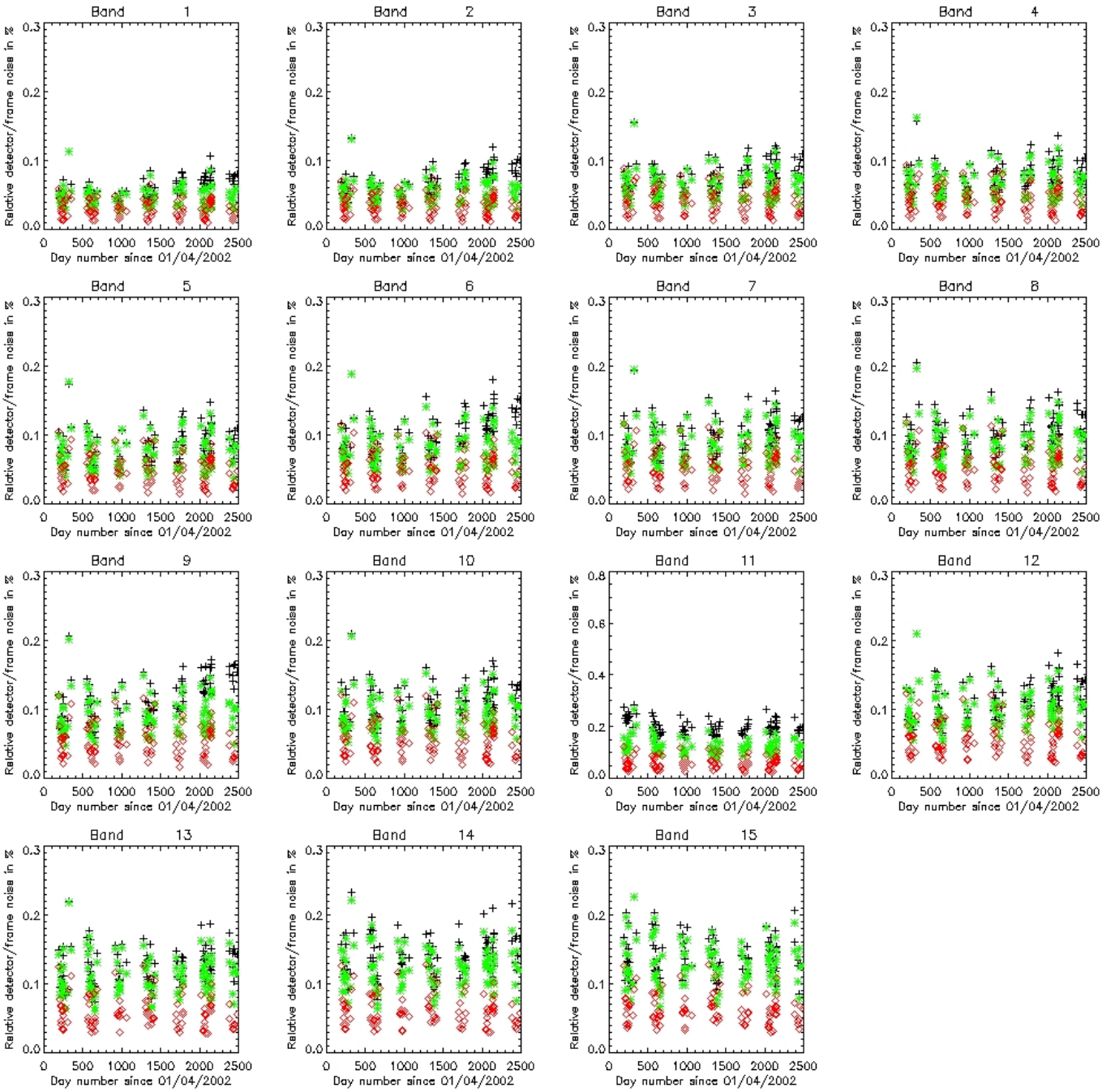

Figure 28: $\sigma_{frame}(\lambda)$ is unchanged by the equalization (in red diamonds), $\sigma_{detector}(\lambda)$ before equalization (in black crosses) and $\sigma_{detector}(\lambda)$ after equalisation (in green stars) all expressed in % for 101 scenes over Antarctica, for equalization coefficients only affect by detector-to-detector radiometric differences and not by at camera interface radiometric differences (group 2 equalization coefficients).

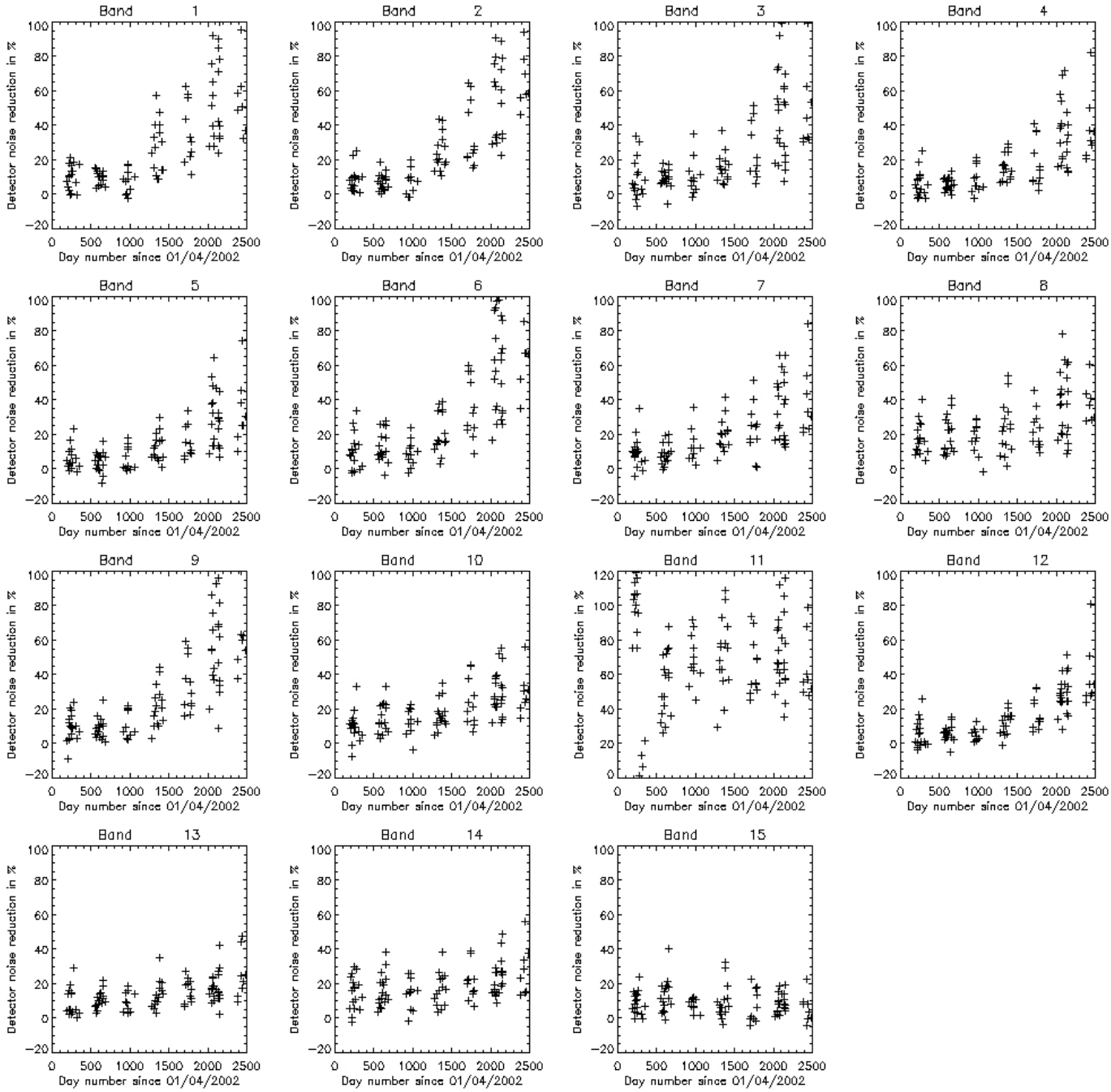

Figure 29: the noise reduction induced by the equalization for 101 scenes over Antarctica for equalization coefficients only affected by detector-to-detector radiometric differences and not by radiometric differences

at camera interface (i.e., equalization coefficients from group 2). The detector noise reduction is expressed as ($\sigma_{\det ector}(\lambda)$ before equalization - $\sigma_{\det ector}(\lambda)$ after equalisation)/ $\sigma_{\det ector}(\lambda)$ after equalization x 100.

5.3 Does the equalization truly work? : visual comparison of equalised and non equalised bands

The best way to measure the impact of the equalization over ocean would to look at L2 products processed with and without equalization. Unfortunately, we do not have MEGS 7.4 available. We can still gain look at smile corrected TOA band ratios and find out whether the vertical striping has been reduced by the equalization procedure. If so, chances are good the L2 processing will benefit from the equalization correction as much as the L1b.

5.3.1 Comparison of equalised and non equalised band ratios: why are band ratios a good mean to verify the equalisation procedure?

Let's assume the following model for the TOA reflectance as observed by a perfect instrument:

$$\rho_{TRUE}^{TOA}(\lambda,x,y)=\overline{\rho}_0(\lambda)\left(1+\delta\rho_{geophysical}^{TOA}(\lambda,x,y)\right)$$

Following the formulation previously introduced, we can write the MERIS measurement:

$$\rho_{MERIS}^{TOA}(\lambda,x,y)=c_{eq}(\lambda,d=f(x,y),t)\rho_{TRUE}^{TOA}(\lambda,x,y)=c_{eq}(\lambda,d=f(x,y),t)\overline{\rho}_0^{TOA}(\lambda)\left(1+\delta\rho_{geophysical}^{TOA}(\lambda,x,y)\right)$$

It is decomposed in an only spectrally dependent term, $\overline{\rho}_0^{TOA}(\lambda)$, a spectrally and detector dependant term $c_{eq}(\lambda,d=f(x,y),t)$ and a spectrally and spatially dependant term $\delta\rho_{geophysical}^{TOA}(\lambda,x,y)$.

It follows that a band ratio writes:

$$\gamma_{MERIS}(\lambda_1,\lambda_{2,}x,y)=\frac{\rho_{MERIS}^{TOA}(\lambda_1,x,y)}{\rho_{MERIS}^{TOA}(\lambda_2,x,y)}=\frac{c_{eq}(\lambda_1,d=f(x,y))}{c_{eq}(\lambda_2,d=f(x,y))}\frac{\overline{\rho}_0^{TOA}(\lambda_1)\left(1+\delta\rho_{geophysical}^{TOA}(\lambda_1,x,y)\right)}{\overline{\rho}_0^{TOA}(\lambda_2)\left(1+\delta\rho_{geophysical}^{TOA}(\lambda_2,x,y)\right)}$$

Using a Taylor series on the denominator and removing second order terms we get:

$$\gamma_{MERIS}(\lambda_1,\lambda_{2,}x,y)=\frac{\rho_{MERIS}^{TOA}(\lambda_1,x,y)}{\rho_{MERIS}^{TOA}(\lambda_2,x,y)}\approx\frac{c_{eq}(\lambda_1,d=f(x,y))}{c_{eq}(\lambda_2,d=f(x,y))}\frac{\overline{\rho}_0^{TOA}(\lambda_1)}{\overline{\rho}_0^{TOA}(\lambda_2)}\left(1+\delta\rho_{geophysical}^{TOA}(\lambda_1,x,y)-\delta\rho_{geophysical}^{TOA}(\lambda_2,x,y)\right)$$

If λ_1 and λ_2 correspond to neighbouring bands and the area is spatially homogeneous then the geophysical residual $\delta\rho_{geophysical}^{TOA}(\lambda_1,x,y)$ and $\delta\rho_{geophysical}^{TOA}(\lambda_2,x,y)$ between the two channels are generally <u>spatially</u> correlated. The band ratio spatial variability is dominated by the detector-to-detector variability.

$$\gamma_{MERIS}(\lambda_1,\lambda_{2,}x,y)\approx\frac{c_{eq}(\lambda_1,d=f(x,y))}{c_{eq}(\lambda_2,d=f(x,y))}\frac{\overline{\rho}_0^{TOA}(\lambda_1)}{\overline{\rho}_0^{TOA}(\lambda_2)}(1+C)$$

On the other hand, the analysis of images tends to show that the detector-to-detector variations in neighbouring spectral bands are in most cases only loosely correlated (see section 6.2.1). Thus when looking at band ratios, using neighbouring band, most of the spatial variability is actually due to the $c_{eq}(\lambda_1, d = f(x,y))$ and $c_{eq}(\lambda_2, d = f(x,y))$. The larger the spectral distance between the two band however, the least the correlation between residual terms in $\left(1+\delta\rho^{TOA}_{geophysical}(\lambda_1, x, y) - \delta\rho^{TOA}_{geophysical}(\lambda_2, x, y)\right)$ and thus the stronger the geophysical spatial variations: the detector-to-detector variability become less visible.
In the following sections we will use these band ratios to enhance the visibility of the detector-to-detector systematic radiometric differences.

5.3.2 Antarctica

In Figure 30 we show a representative example taken from the verification dataset over Antarctica of the impact of the equalization procedure on band ratios. Clearly the image quality is improved.

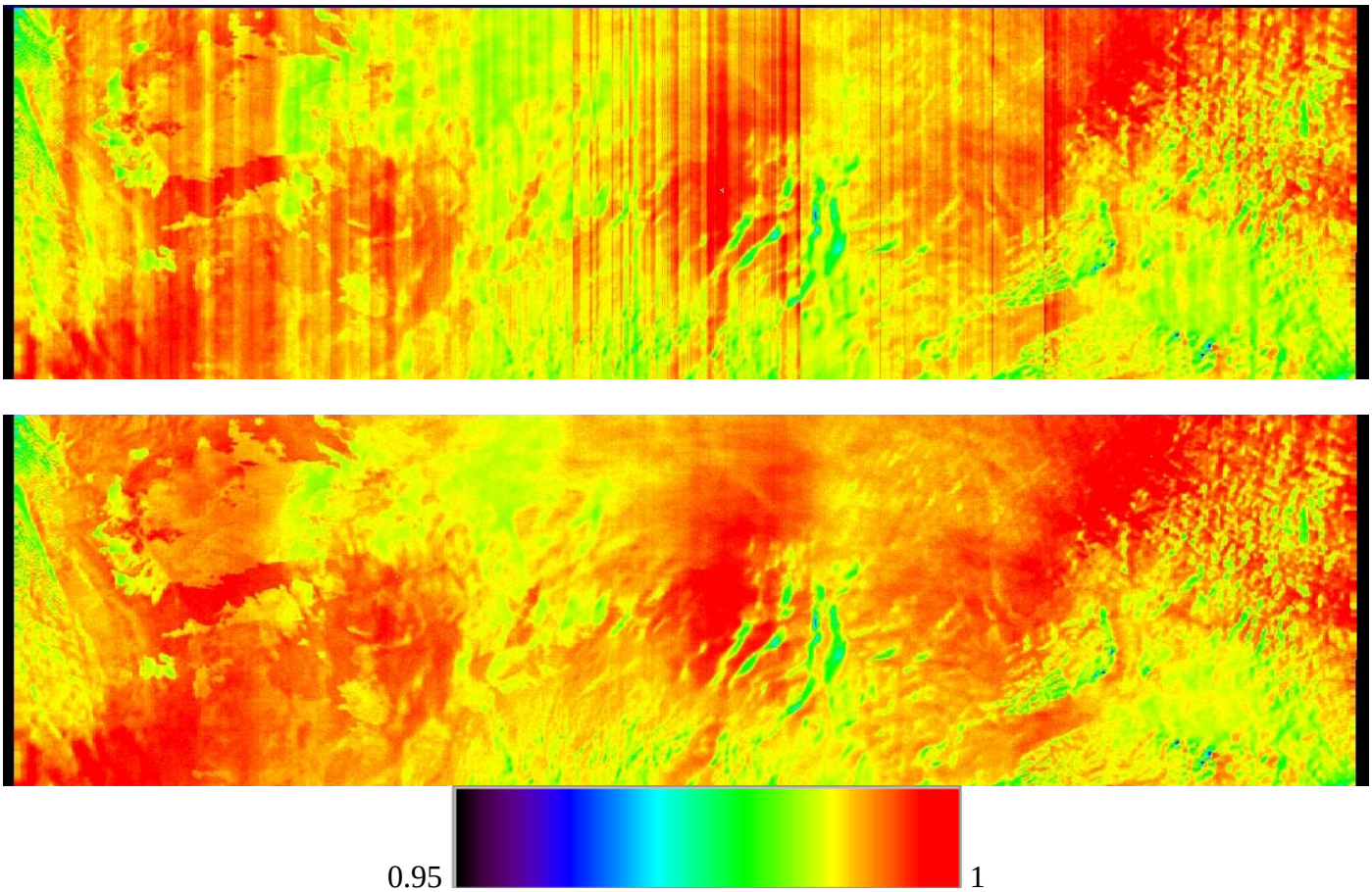

Figure 30: $\frac{\rho^{TOA}_{MERIS}(865)}{\rho^{TOA}_{MERIS}(778)}$ *before (top panel) and after (bottom panel) equalization for the product MER_RR__1PPBCM20061121_003105_000000542053_00102_24705_0045.N1*

5.3.3 Ocean

5.3.3.1 Example 1

We have verified several scenes over ocean and reach the same conclusion: the equalization should significantly improve MERIS L2 products. As an example, Figure 31 shows the corresponding L2 Algal 1 product processed with the IPF version (equivalent to MEGS 7.4). No equalization correction was thus applied prior to the L2 processing. Again, as shown in our introduction (see section 2), the vertical striping is clearly visible on this Algal 1 product (and on all Algal 1 products actually).

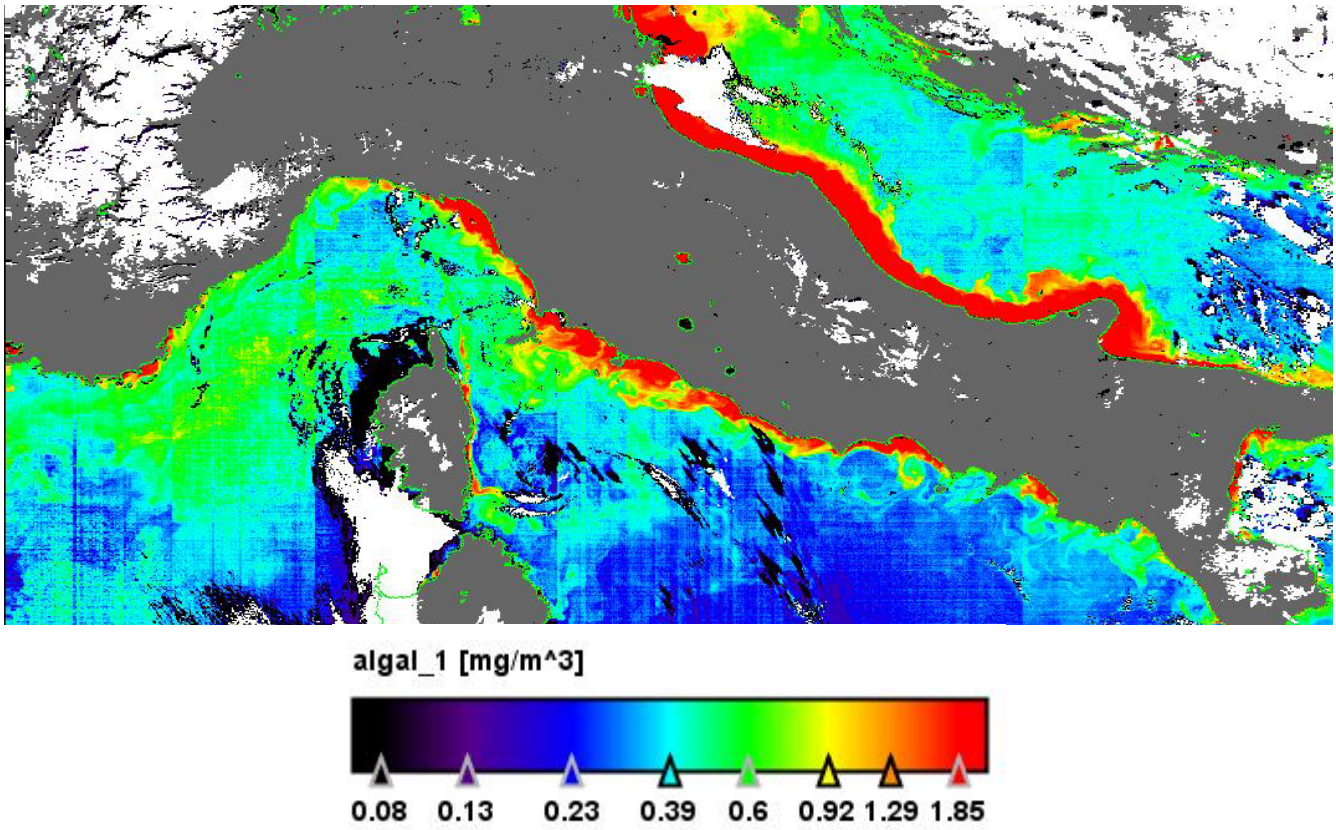

Figure 31: The Algal 1 L2 product corresponding to the L1b MER_RR__1PPACR20081221_094343_000000902074_00480_35604_0000

Figure 32 and Figure 33 show the band ratios, at L1b TOA smile corrected reflectance level, of respectively $\frac{\rho_{MERIS}^{TOA}(510)}{\rho_{MERIS}^{TOA}(490)}$ and $\frac{\rho_{MERIS}^{TOA}(560)}{\rho_{MERIS}^{TOA}(510)}$ with and without equalization. Clearly the equalization significantly improves the situation at L1b. Most of the vertical striping disappears and the frame-to-frame noise becomes dominant.

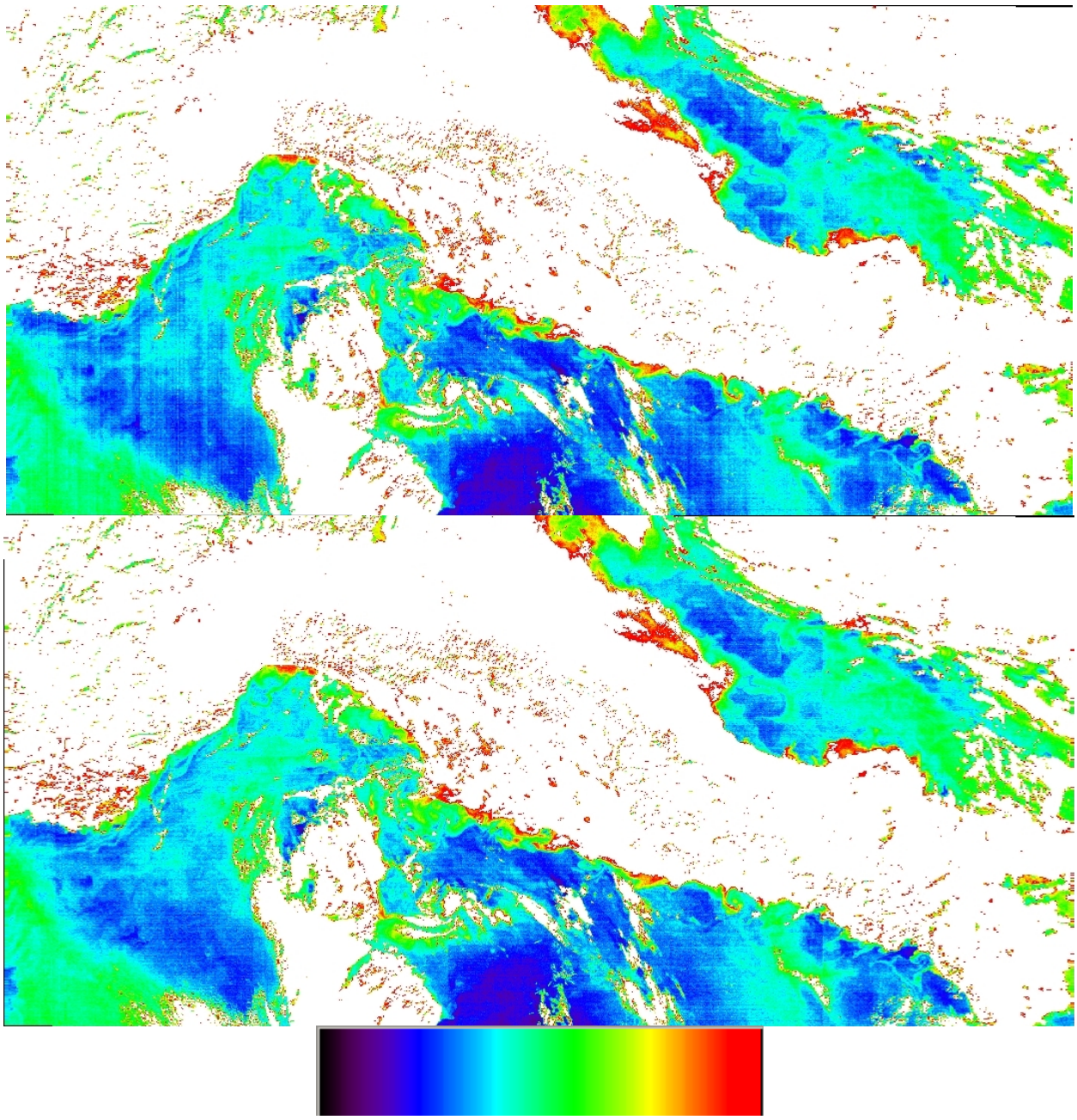

Figure 32: Band ratio between the smile corrected L1 TOA reflectance in band 4 and 3, before equalization (top panel) and after equalization (bottom panel). The color scale ranges from from 0.83 to 0.88

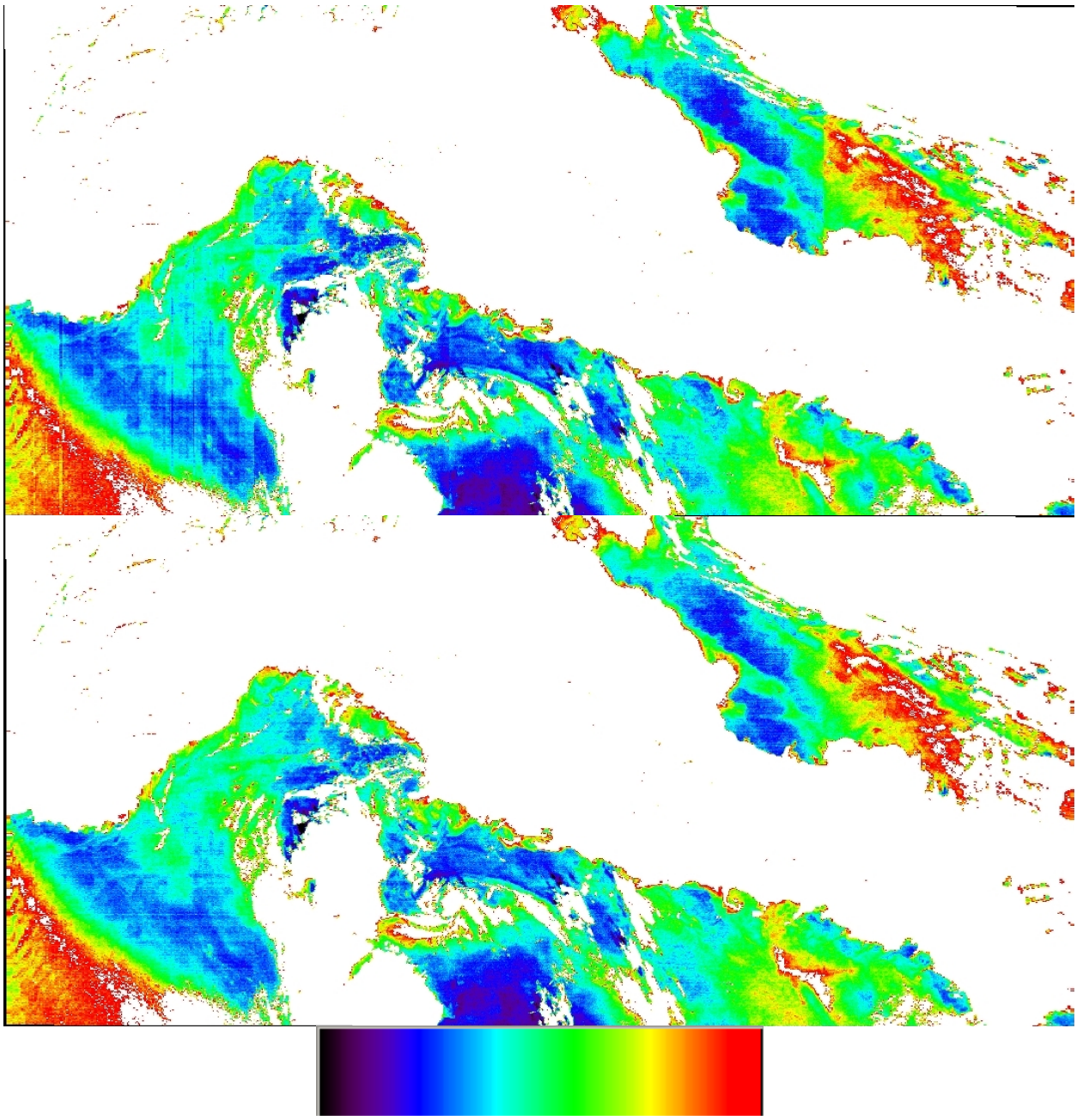

Figure 33: Band ratio between the smile corrected L1 TOA reflectance in band 5 and 4, before equalization (top panel) and after equalization (bottom panel). The color scale ranges from from 0.66 to 0.7

5.3.3.2 Example 2

Figure 34 shows a L2 Algal 1 product processed with the IPF version (equivalent to MEGS 7.4). No equalization correction was applied prior to the L2 processing.

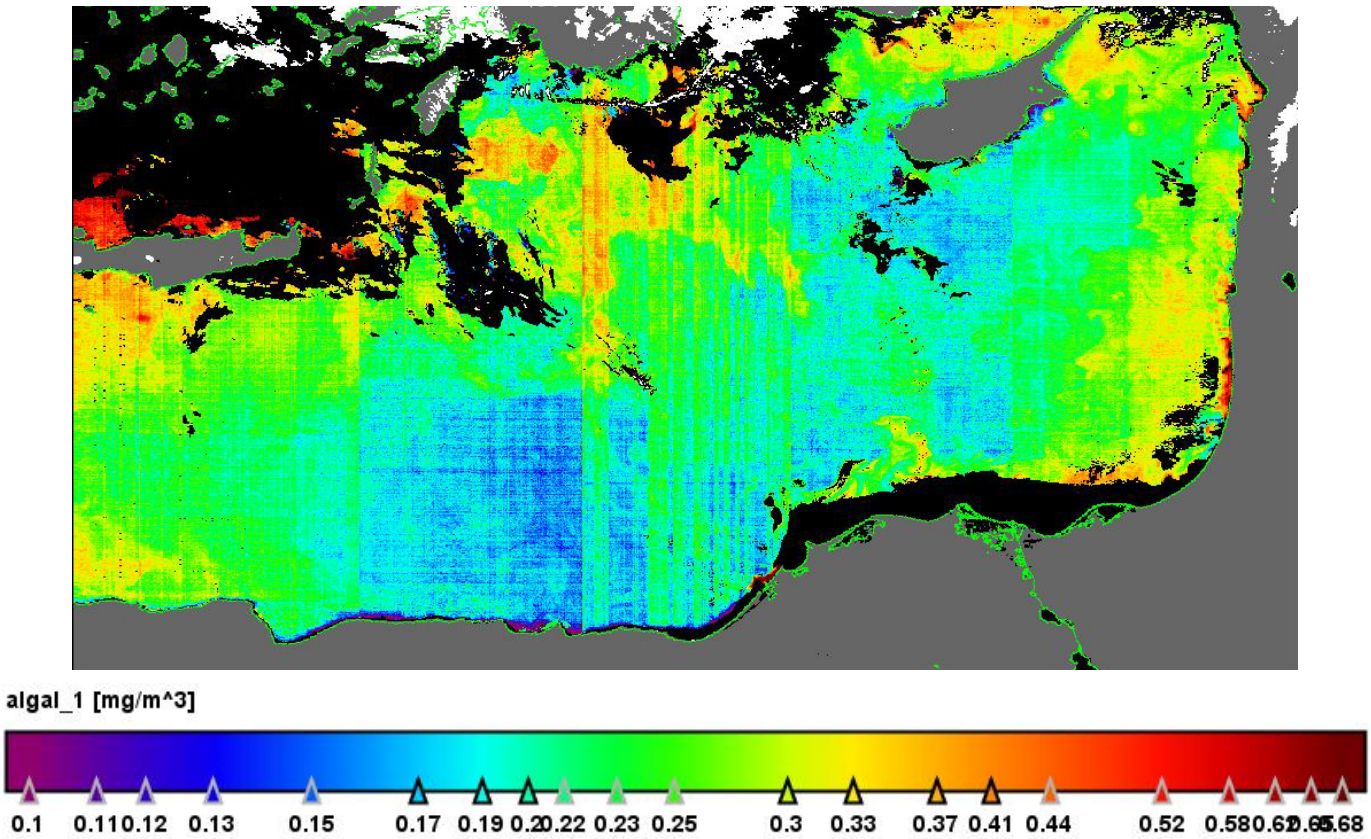

Figure 34: The Algal 1 L2 product corresponding to the L1b MER_RR__1PPBCM20090203_082156_000002002076_00107_36233_0075.N1

In Figure 35 we show the results of the equalization for a band ratio.

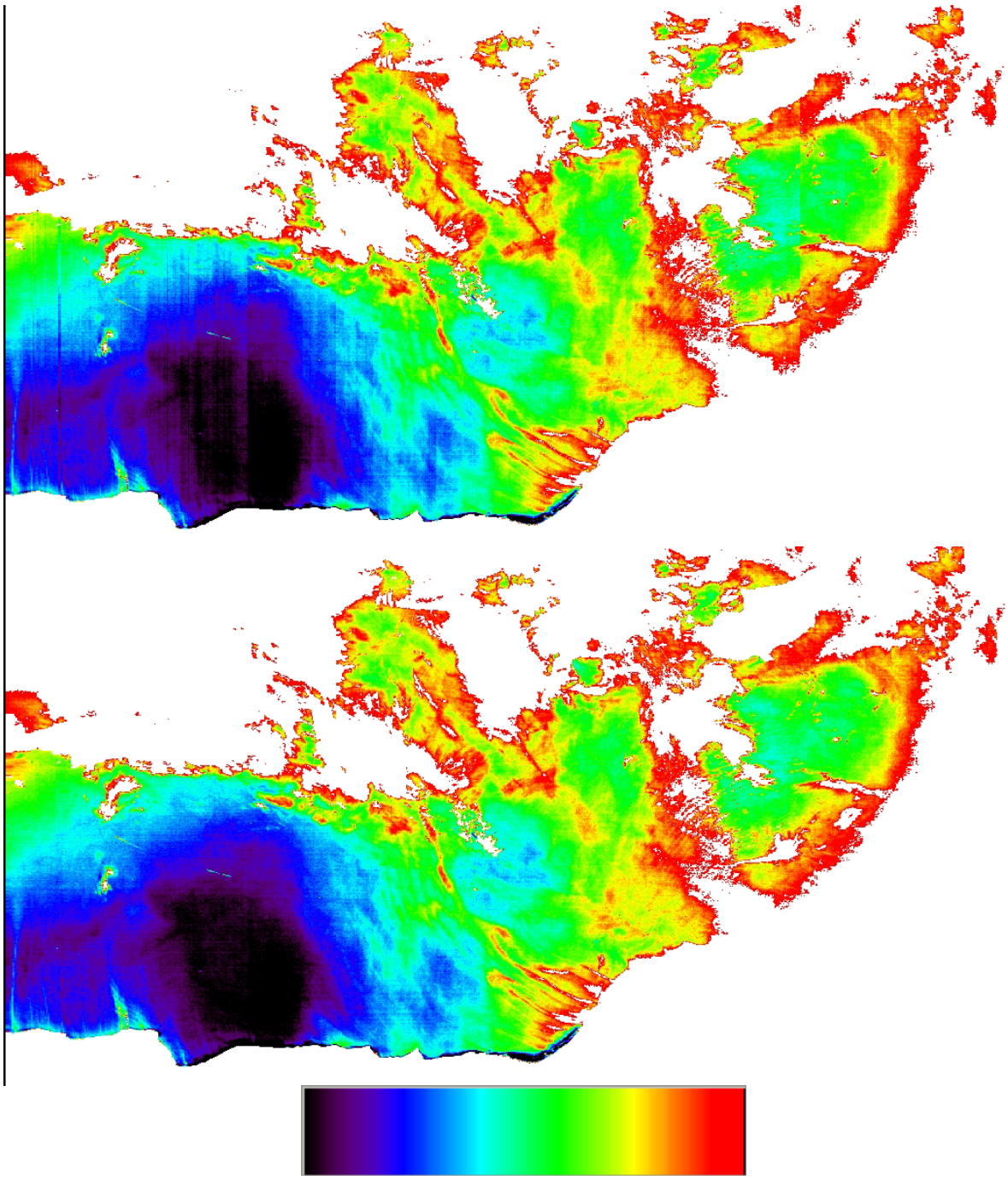

Figure 35: Band ratio between the smile corrected L1 TOA reflectance in band 5 and 4, before equalization (top panel) and after equalization (bottom panel). The color scale ranges from from 0.66 to 0. The L1b product is MER_RR__1PPBCM20090203_082156_000002002076_00107_36233_0075.N1

5.3.4 Vegetation

Figure 36 shows an example of band ratio before and after equalization for a scene over the Amazon forest. The image quality is significantly improved although camera interfaces are still visible.

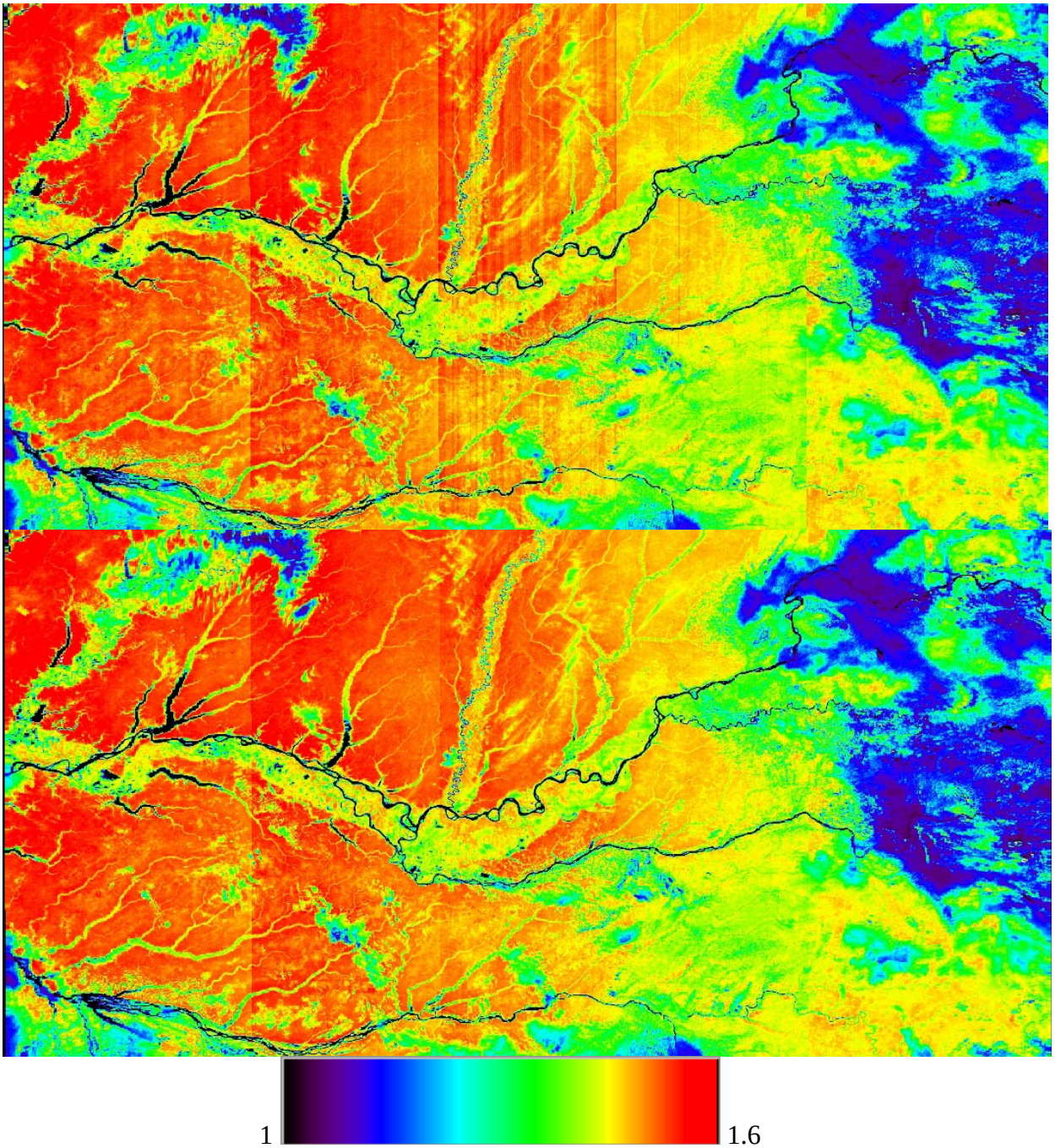

Figure 36: Band ratio between the smile corrected L1 TOA reflectance in band 13 and 12, before equalization (top panel) and after equalization (bottom panel). The color scale ranges from from 1 to 1.6 The L1b product is MER_RR__1PPBCM20080716_142304_000003972070_00225_33345_0119.N1

5.4 Conclusion of the verification

The L1b data seem to be significantly improved by the equalization correction over all surface types and at any time of the mission. Since the detector-to-detector radiometric differences increase with time the (positive) impact of the equalization on image quality is greater for the most recent products.

6 Discussion

6.1 Known issues and limitations

6.1.1 Determination of coefficients at the edges of the swath

We are using a 51 detector sliding average as a smoothing procedure for the mean detector TOA reflectance (see formula in section 3.2.1). For the first 20 and last 20 detectors, the smoothing is done using several times the first and last detector TOA reflectance values, thus giving weight in to the first and last detector TOA reflectances. Should the TOA reflectance variations with detector index be too steep, in these two area of the swath, it might lead to local overestimation/underestimation of the 'true' geophysical signal for which the smoothed function is a proxy.

6.1.2 Equalization of band 11

The retrieval of equalisation coefficients as it is described in the present document is not applicable to band 11 and 15 since there is no smile correction for these two bands. Moreover, band 11 position was changed in December 2002.

Although we did not yet develop such smile correction for band 11, we have retrieved equalization coefficients for band 11. These equalization coefficients should not be used for equalization, but we attempted to apply them to one of the products in our verification dataset. Surprisingly, detector-to-detector systematic variations in band 11 are well corrected for as can be observed in Figure 37. This is an encouraging sign that Antarctica could be used to derive equalization coefficients in band 11 as well (should an appropriate smile correction be derived for band 11).

The development of a smile correction for band 11 would require high spectral resolution TOA reflectance simulation to enable a 'reflectance correction' for the smile effects.

Moreover, for this band, each camera could be equalized separately.

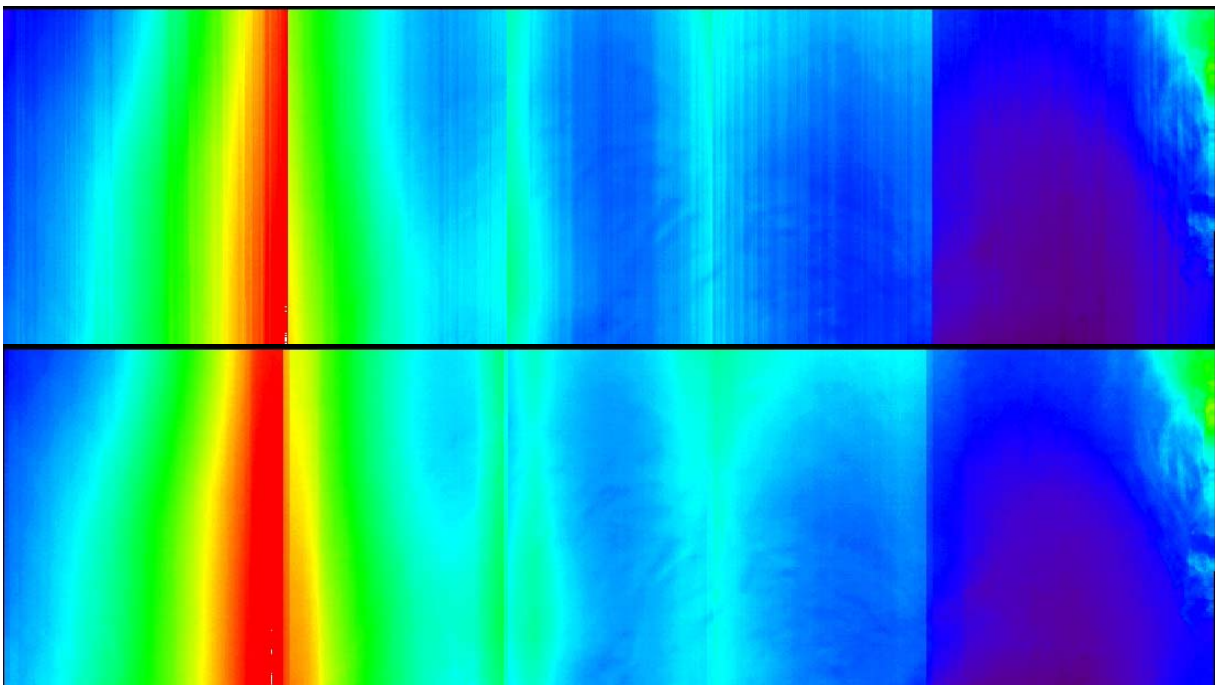

Figure 37: $\frac{\rho_{MERIS}^{TOA}(900)}{\rho_{MERIS}^{TOA}(885)}$ *before (top panel) and after (bottom panel) equalization for the product MER_RR__1PPBCM20061121_003105_000000542053_00102_24705_0045.N1*

6.1.3 Equalization of band 15

Although we did not yet develop such smile correction for band 15, we have retrieved equalization coefficients for band 15 and applied them to one of the products in our verification dataset. Again, the detector-to-detector systematic variations are well corrected for in band 15 as can be observed in Figure 38.

Moreover, the 205 acquisitions we selected are acquired over the Antarctica plateau. It has been found that the water vapour content over this area is extremely low (R - 6). We should thus expect only a small influence of the gaseous absorption in band 11. A smile correction assuming no water vapour absorption could be applied to band 15 data following the methodology applied at other bands. The formalism presented in this technical note to retrieve the correlation coefficients would apply. The retrieved coefficients should then remain valid even in cases where water vapour absorption is significant. Exploitation of band 15 in cases of significant water vapour absorption would still require a smile correction or a retrieval algorithm that make explicit use of the detector dependency of the central wavelength in band 14 and 15.

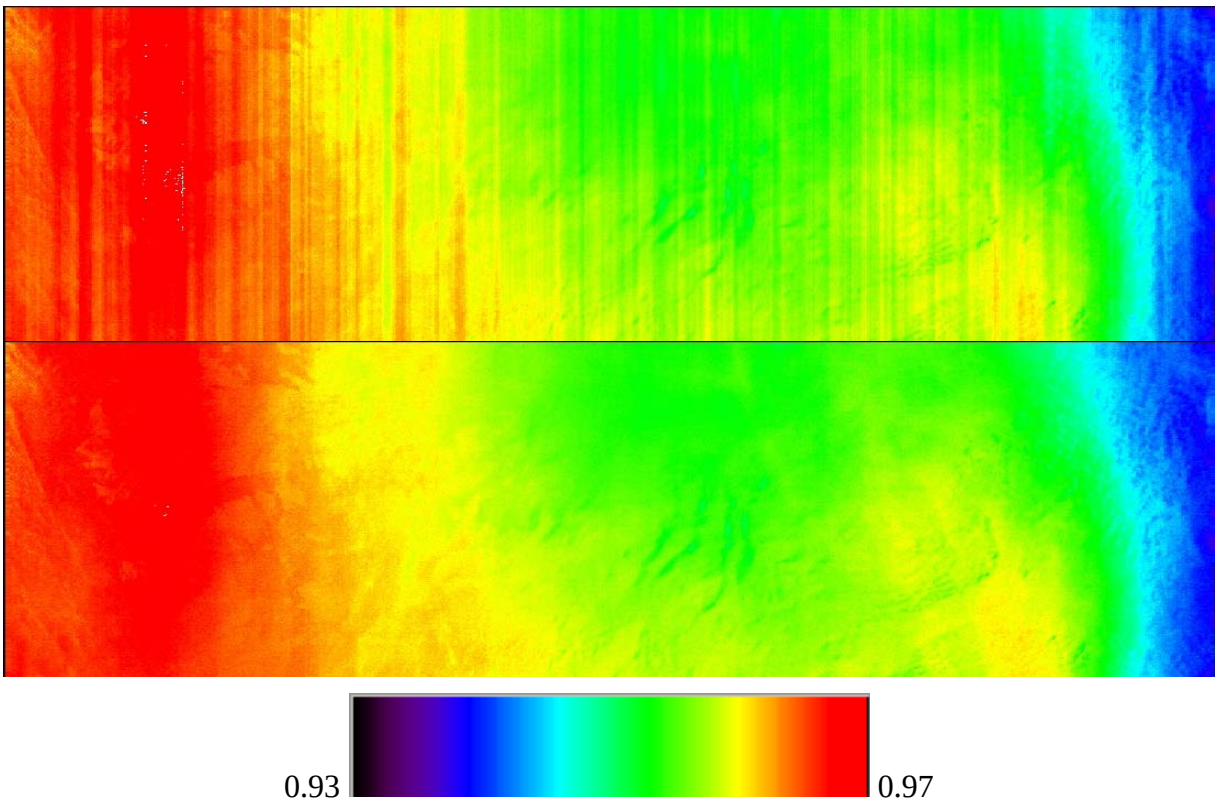

Figure 38: $\frac{\rho_{MERIS}^{TOA}(900)}{\rho_{MERIS}^{TOA}(885)}$ *before (top panel) and after (bottom panel) equalization for the product MER_RR__1PPBCM20061121_003105_000000542053_00102_24705_0045.N1*

6.1.4 Smile correction

We already discussed the need for a smile correction prior to the retrieval of the equalization coefficients or prior to their application. The smile correction we used in our breadboard follows the BEAM approach, i.e., the reflectance correction (the smile correction is a two step correction: 1) irradiance correction, 2) reflectance correction) is done at TOA level. In the L2 processing, in the ground segment, this is done after gaseous correction, stratospheric aerosol correction and glint correction. We believe the ground segment approach is wrong. The ground segment approach leads to significant smile correction errors when trying to perform a reflectance correction in bands located in the wing of the Chapuis band over Antarctica (our approach as well due to the assumption of linear interpolation in this band)

6.2 Characteristics of the equalization coefficients

6.2.1 What is the impact of the equalization on the global radiometry of a product?

In section 3.2.3.3 we mentioned that the equalization should not introduce significant biases in the radiometry of a full L1b product. We estimated the change to be less than about 0.01% at TOA reflectance level (taking 3-sigma confidence interval). To quantify the impact of the retrieved equalization coefficients we average them across the swath for each day of the mission and each band:

$$\bar{c}_{eq}(\lambda,t_i) \equiv \frac{1}{d_{\max}} \sum_{d=0}^{d_{\max}} c_{eq}(\lambda,d,t_i) = \frac{1}{d_{\max}} \sum_{d=0}^{d_{\max}} \left[c_{eq}^{t=0}(\lambda,d) + \frac{\partial c_{eq}(\lambda,d,t)}{\partial t} t_i + \frac{\partial^2 c_{eq}(\lambda,d,t)}{\partial t^2} t_i^2 \right]$$

The results of the time variations of $\bar{c}_{eq}(\lambda,t_i)$ are shown in Figure 39. We observe that the $\bar{c}_{eq}(\lambda,t_i)$ are always below 1.0001, thus corresponding to a bias on the TOA reflectance radiometry of a product always below 0.01 % and generally below 0.005%. This is in line with our estimate previously mentioned from section 3.2.3.3. Such biases are one order of magnitude smaller than the detector-to-detector radiometric differences the equalization corrects for. The introduced biases can be considered marginal.

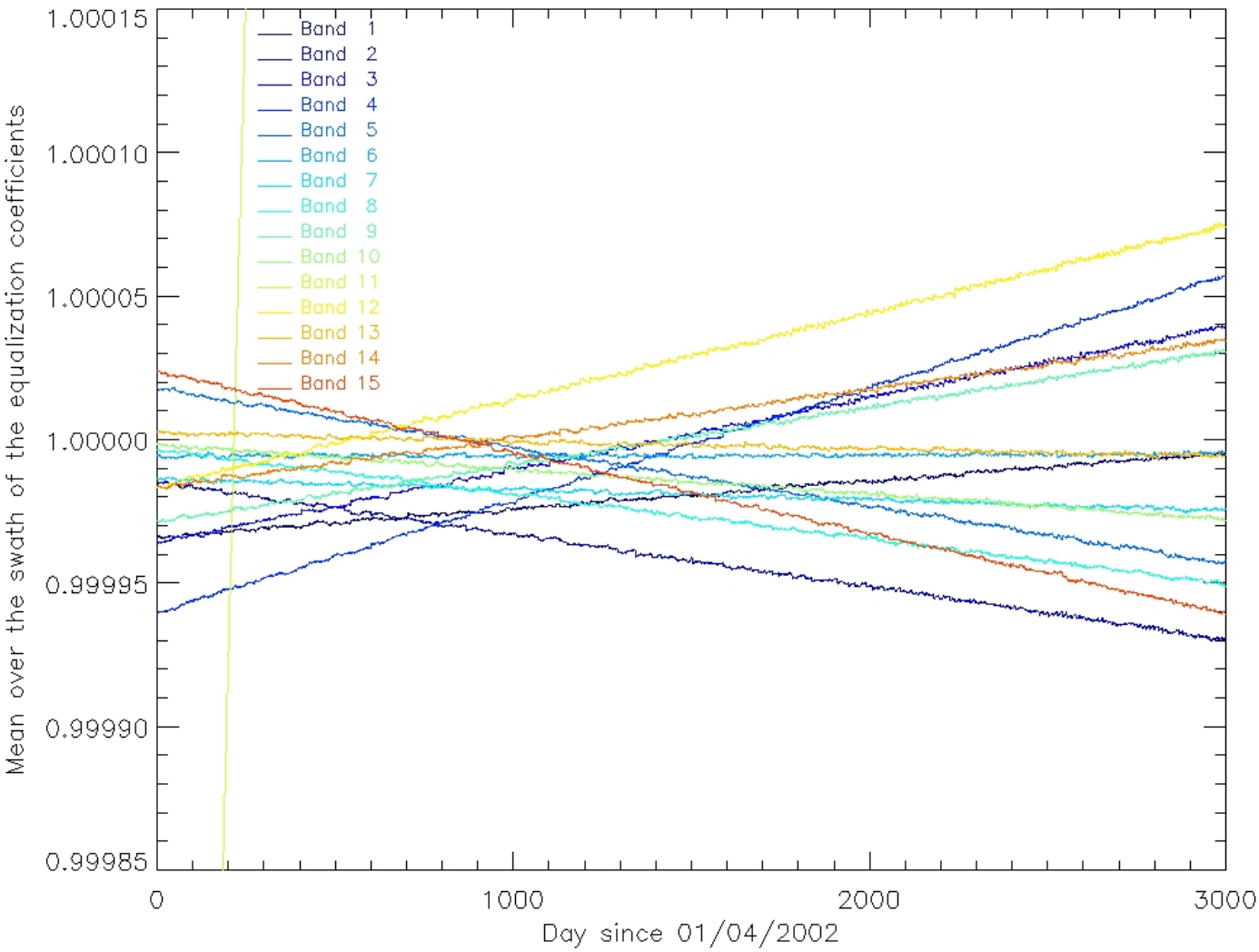

Figure 39: the time variations of mean across track equalization coefficient $\bar{c}_{eq}(\lambda, t_i)$ in each band.

6.2.2 Time variations of the standard deviation associated to the detector-to-detector variability of the equalization coefficients

In the previous section, we have analysed how the mean value across all detectors of the equalization coefficient in a given band changes through time. We can also look at how the standard deviation associated with this mean. Using the retrieved 2nd order model we can compute the equalization coefficient every first day of each year. Whilst in the previous section we computed the mean equalization across track for all detectors, we here focus on the coefficients from group 2 (i.e., excluding those for which there is an influence of at camera interface radiometric differences) and compute the standard deviation. The results are presented in Figure 40. It can be noted that the amplitude of the detector-to-detector systematic differences

increases with time for all bands. It has increased by about a factor 3 for the visible since the beginning of the MERIS mission.

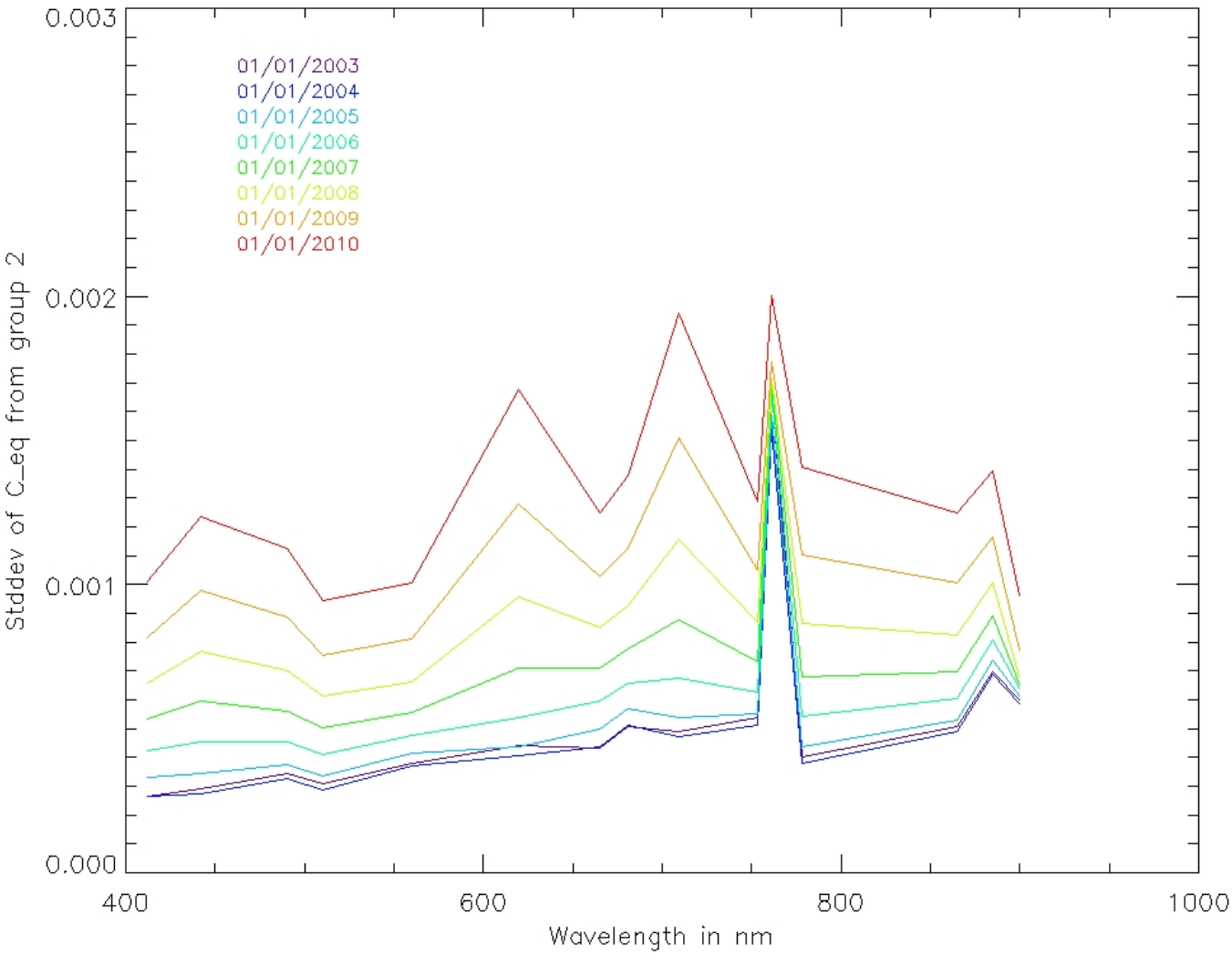

Figure 40: the standard deviation associated to the across track variations of the equalization coefficients in group 2 for each spectral band, every 1st day of the year since 2003.

6.2.3 Band to band correlations between equalisation coefficients

In Figure 41 we present the band-to-band correlation coefficients of the $c_{eq}^{t=0}(\lambda,d)$, $\frac{\partial c_{eq}(\lambda,d,t)}{\partial t}$, $\frac{\partial^2 c_{eq}(\lambda,d,t)}{\partial t^2}$ in a matrix form with the correlation coefficients are colour coded to give an immediate visual

impression. We use the widely spread Pearson correlation coefficients and apply it to the particular case, for instance for $c_{eq}^{t=0}(\lambda,d)$ we have:

$$r^2(\lambda_i,\lambda_j) = \frac{\left[\sum_{d=0}^{N_{\max}(d)}\left(c_{eq}^{t=0}(\lambda_i,d)-\bar{c}_{eq}^{t=0}(\lambda_i)\right)\left(c_{eq}^{t=0}(\lambda_j,d)-\bar{c}_{eq}^{t=0}(\lambda_j)\right)\right]^2}{\sum_{d=0}^{N_{\max}(d)}\left(c_{eq}^{t=0}(\lambda_i,d)-\bar{c}_{eq}^{t=0}(\lambda_i)\right)^2 \sum_{d=0}^{N_{\max}(d)}\left(c_{eq}^{t=0}(\lambda_j,d)-\bar{c}_{eq}^{t=0}(\lambda_{js})\right)^2}$$

Several observations can be made:

- There is a significant correlation between the $c_{eq}^{t=0}(\lambda,d)$ of band 2, 3, 4, 6, 7, 9, 12 with r^2 around 0.5. The $c_{eq}^{t=0}(\lambda,d)$ of band 1, 5, 8, 10, 13, 14 and 15 are loosely correlated somewhat much less correlated, r^2 mostly between 0 and 0.5.
- There is a clear "proximity correlation'' pattern visible for the linear trend $\frac{\partial c_{eq}(\lambda,d,t)}{\partial t}$: the $\frac{\partial c_{eq}(\lambda,d,t)}{\partial t}$ of neighbouring bands are generally well correlated (with $r^2 > 0.7$ for 4 neighbouring bands).
- We can distinguish two groups of correlations for the quadratic trend $\frac{\partial^2 c_{eq}(\lambda,d,t)}{\partial t^2}$: band 2 to 10 (except band 9) and band 12 to 15.
- In all three coefficients $c_{eq}^{t=0}(\lambda,d)$, $\frac{\partial c_{eq}(\lambda,d,t)}{\partial t}$, $\frac{\partial^2 c_{eq}(\lambda,d,t)}{\partial t^2}$, band 1 appears to be loosely or not correlated to other bands.

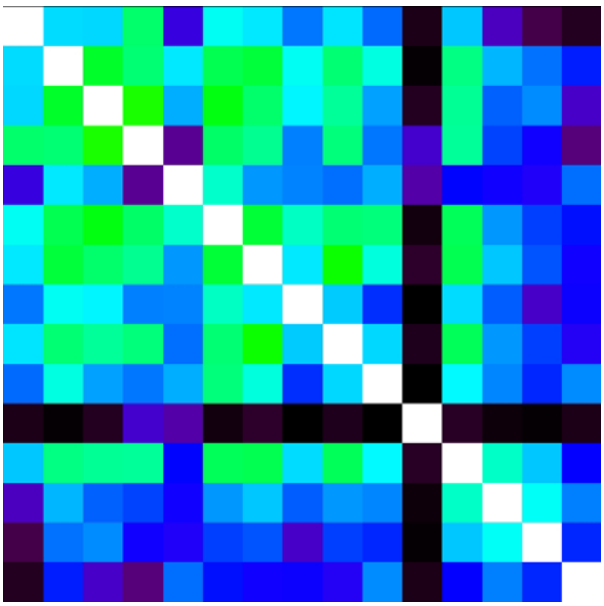

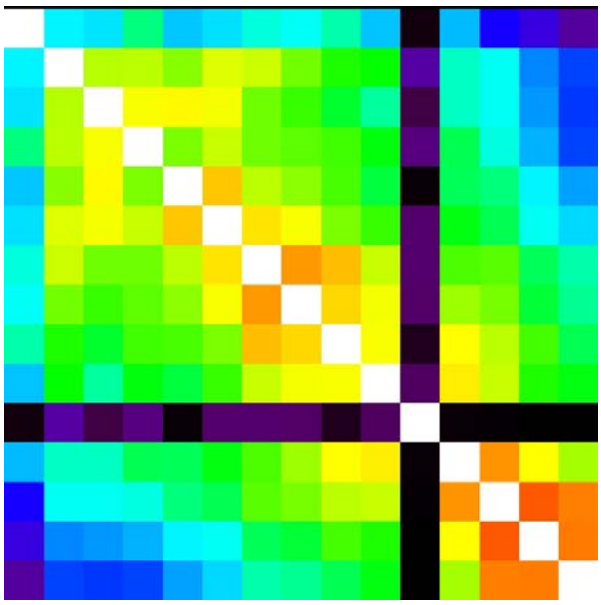

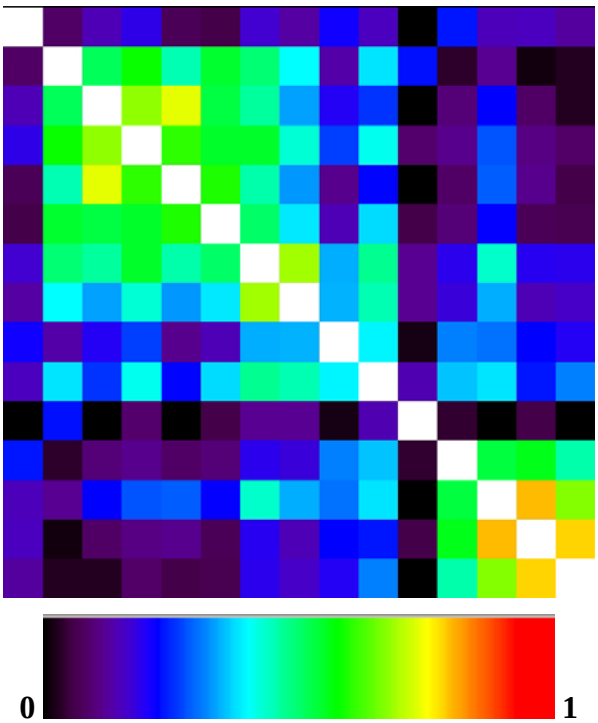

Figure 41: The correlation coefficients between spectral bands for the $c_{eq}^{t=0}(\lambda,d)$, $\frac{\partial c_{eq}(\lambda,d,t)}{\partial t}$, $\frac{\partial^2 c_{eq}(\lambda,d,t)}{\partial t^2}$ *presented as a matrix respectively in the top, middle and bottom panel. The correlation coefficients range from 0 to 1 (in white).*

6.2.4 Correlations between $c_{eq}^{t=0}(\lambda,d)$, $\frac{\partial c_{eq}(\lambda,d,t)}{\partial t}$ and $\frac{\partial^2 c_{eq}(\lambda,d,t)}{\partial t^2}$

Here we try to answer the following question: are the time variations of the equalization coefficients related to the value of the equalization coefficients at launch? In other words, is the amplitude of the equalization coefficients simply changing with time or is also the detector-to-detector pattern changing with time?

To study this we compute the correlation coefficients between $c_{eq}^{t=0}(\lambda,d)$, $\frac{\partial c_{eq}(\lambda,d,t)}{\partial t}$ and $\frac{\partial^2 c_{eq}(\lambda,d,t)}{\partial t^2}$, for each band. For instance, the correlation coefficient between $c_{eq}^{t=0}(\lambda,d)$, $\frac{\partial c_{eq}(\lambda,d,t)}{\partial t}$ in band 1 is:

$$r\left(c_{eq}^{t=0}(\lambda_1,d),\frac{\partial c_{eq}(\lambda_1,d,t)}{\partial t}\right)=\frac{\left[\sum_{d=0}^{N_{\max}(d)}\left(c_{eq}^{t=0}(\lambda_1,d)-\bar{c}_{eq}^{t=0}(\lambda_1)\right)\left(\frac{\partial c_{eq}(\lambda_1,d,t)}{\partial t}-\overline{\frac{\partial c^2{}_{eq}(\lambda_1,d,t)}{\partial t}}\right)\right]}{\sum_{d=0}^{N_{\max}(d)}\left(c_{eq}^{t=0}(\lambda_1,d)-\bar{c}_{eq}^{t=0}(\lambda_1)\right)\sum_{d=0}^{N_{\max}(d)}\left(\frac{\partial c_{eq}(\lambda_1,d,t)}{\partial t}-\overline{\frac{\partial c^2{}_{eq}(\lambda_1,d,t)}{\partial t}}\right)}$$

The result of the computation for each spectral band between $c_{eq}^{t=0}(\lambda,d)$, $\frac{\partial c_{eq}(\lambda,d,t)}{\partial t}$ and $\frac{\partial^2 c_{eq}(\lambda,d,t)}{\partial t^2}$ are shown in Figure 42.

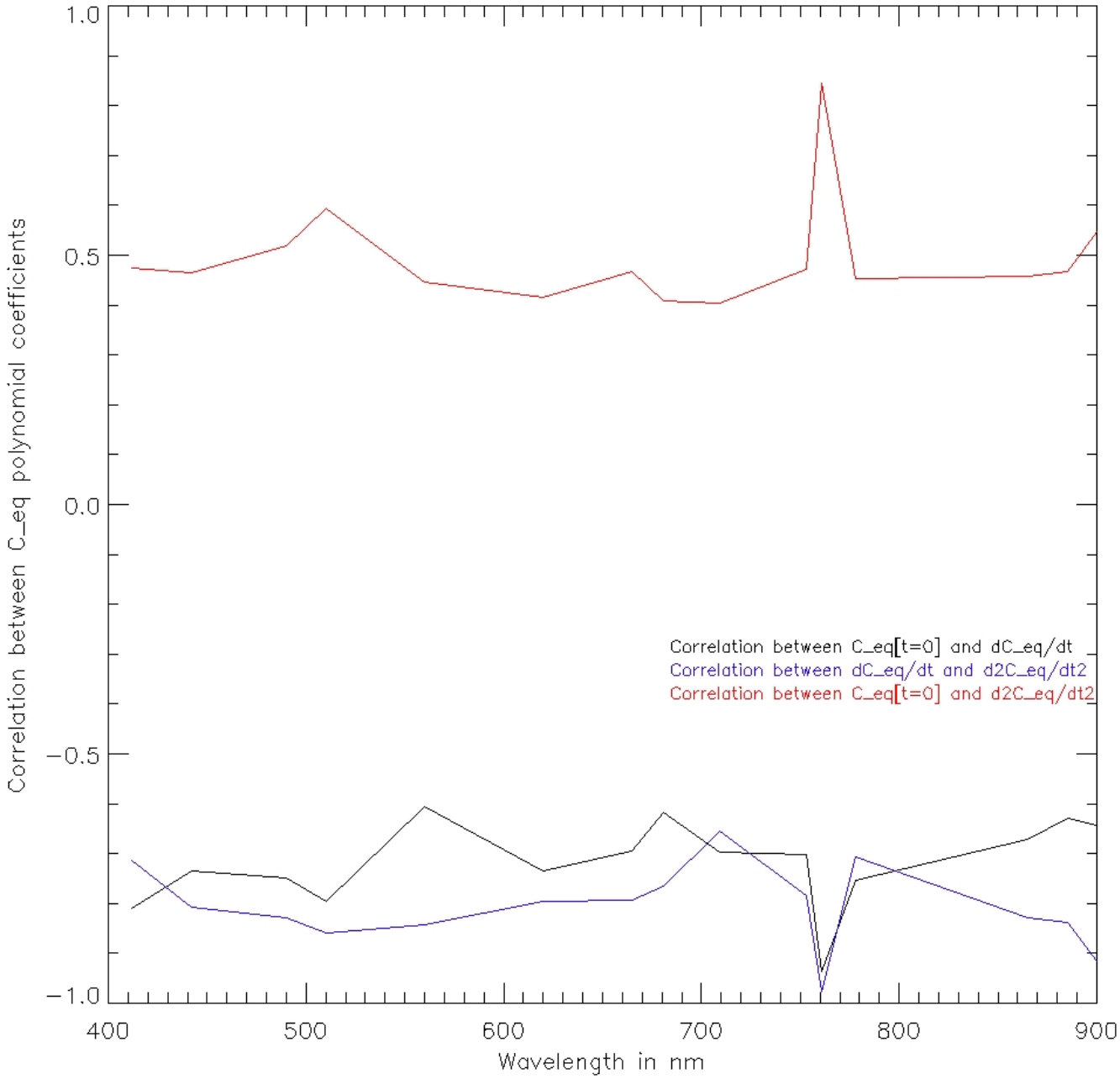

Figure 42: The correlation coefficients between spectral bands for the $c_{eq}^{t=0}(\lambda,d)$, $\frac{\partial c_{eq}(\lambda,d,t)}{\partial t}$, *and* $\frac{\partial^2 c_{eq}(\lambda,d,t)}{\partial t^2}$.

The results on Figure 42 seem to indicate that values of $c_{eq}^{t=0}(\lambda,d)$ are anti correlated with $\frac{\partial c_{eq}(\lambda,d,t)}{\partial t}$, and $\frac{\partial^2 c_{eq}(\lambda,d,t)}{\partial t^2}$. The correlation coefficient is significant but strictly equal to 1. An example of the variations with time of $c_{eq}(\lambda,d,t)$ is shown for band 1, in a region of the swath around the interface between camera 3 and 4.

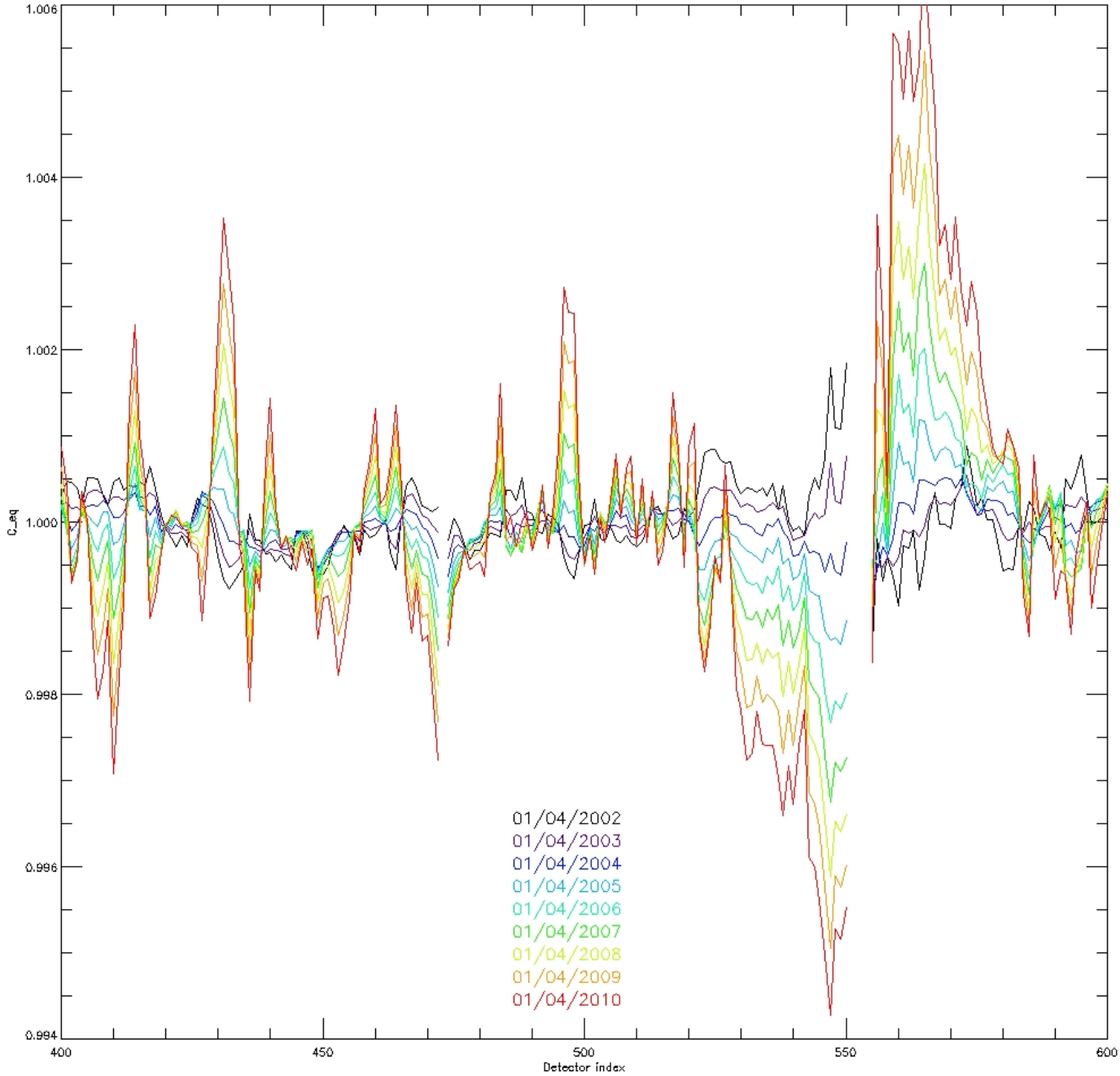

Figure 43: The variations of the coefficients between spectral bands for the $c_{eq}(\lambda, d, t)$ in band 1 for 9 different years. The interface between camera 3 and 4 is visible between the detector indices 550 and 560.

6.2.5 Is there a particular spatial frequency characterising the detector-to-detector systematic differences?

To answer this question, we plot respectively in Figure 44, Figure 45 and Figure 46 the square of the autocorrelation function of $c_{eq}^{t=0}(\lambda,d)$, $\frac{\partial c_{eq}(\lambda,d,t)}{\partial t}$, $\frac{\partial^2 c_{eq}(\lambda,d,t)}{\partial t^2}$. We have excluded equalization coefficients from group 1 and kept only group 2 equalization coefficients to decouple this analysis from camera interface issues (see section 5.2).

Several remarks:

- The autocorrelation function in all bands is significant (i.e. $r^2 > 0.2$) for a detector lag of 3 to 4 detectors only.
- For larger detector lags the values of the square of the autocorrelation function are very small but peaks are visible around 20 detectors and its successive harmonics (not all harmonics are visible on the figures)

For reminder, the autocorrelation of a random process is a Dirac function. The autocorrelation functions for $c_{eq}^{t=0}(\lambda,d)$, $\frac{\partial c_{eq}(\lambda,d,t)}{\partial t}$, $\frac{\partial^2 c_{eq}(\lambda,d,t)}{\partial t^2}$ suggest that they follow a nearly random distribution.

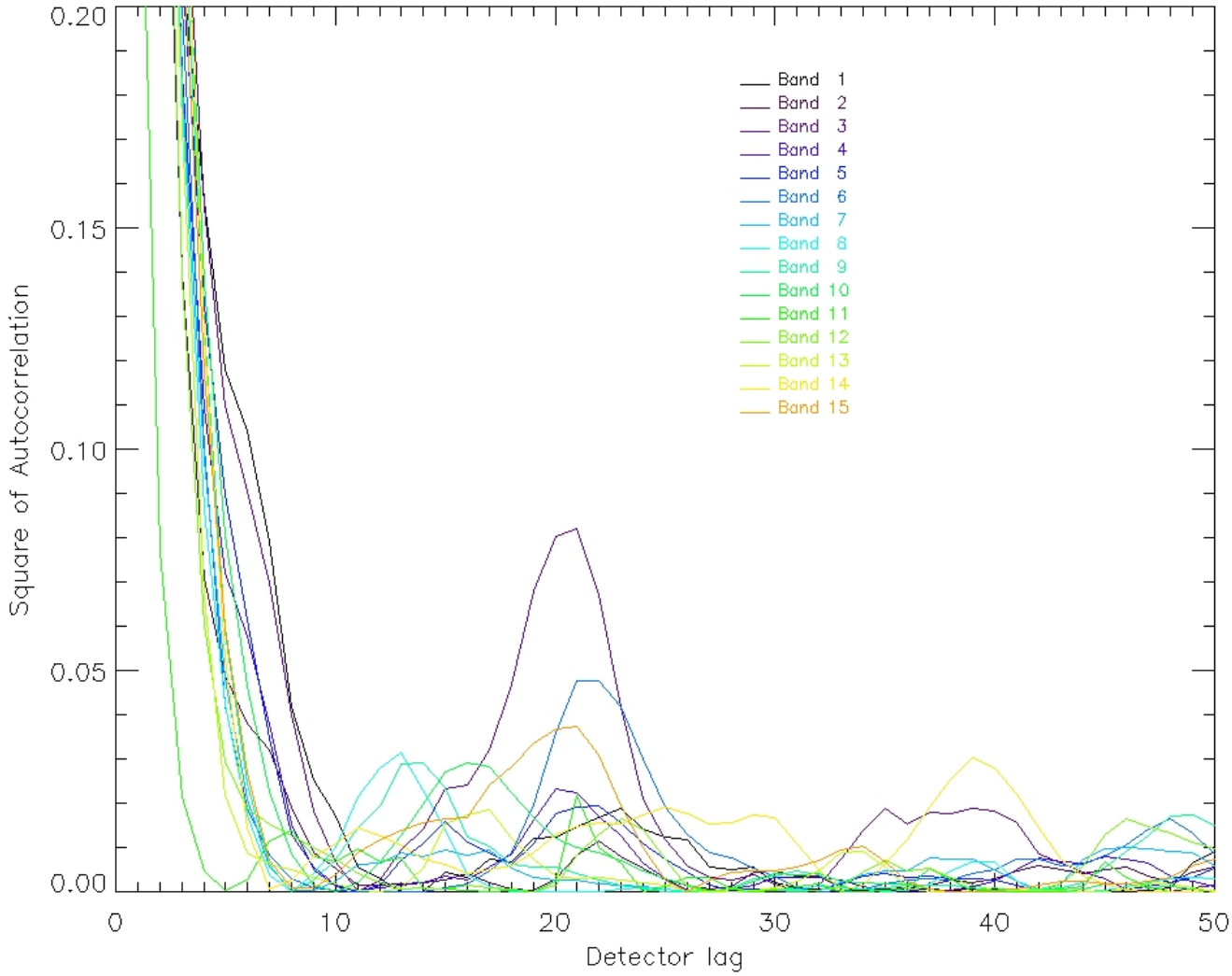

Figure 44: Zoom on the square of the autocorrelation function of the $c_{eq}^{t=0}(\lambda,d)$ *up to a 50 detector lag*

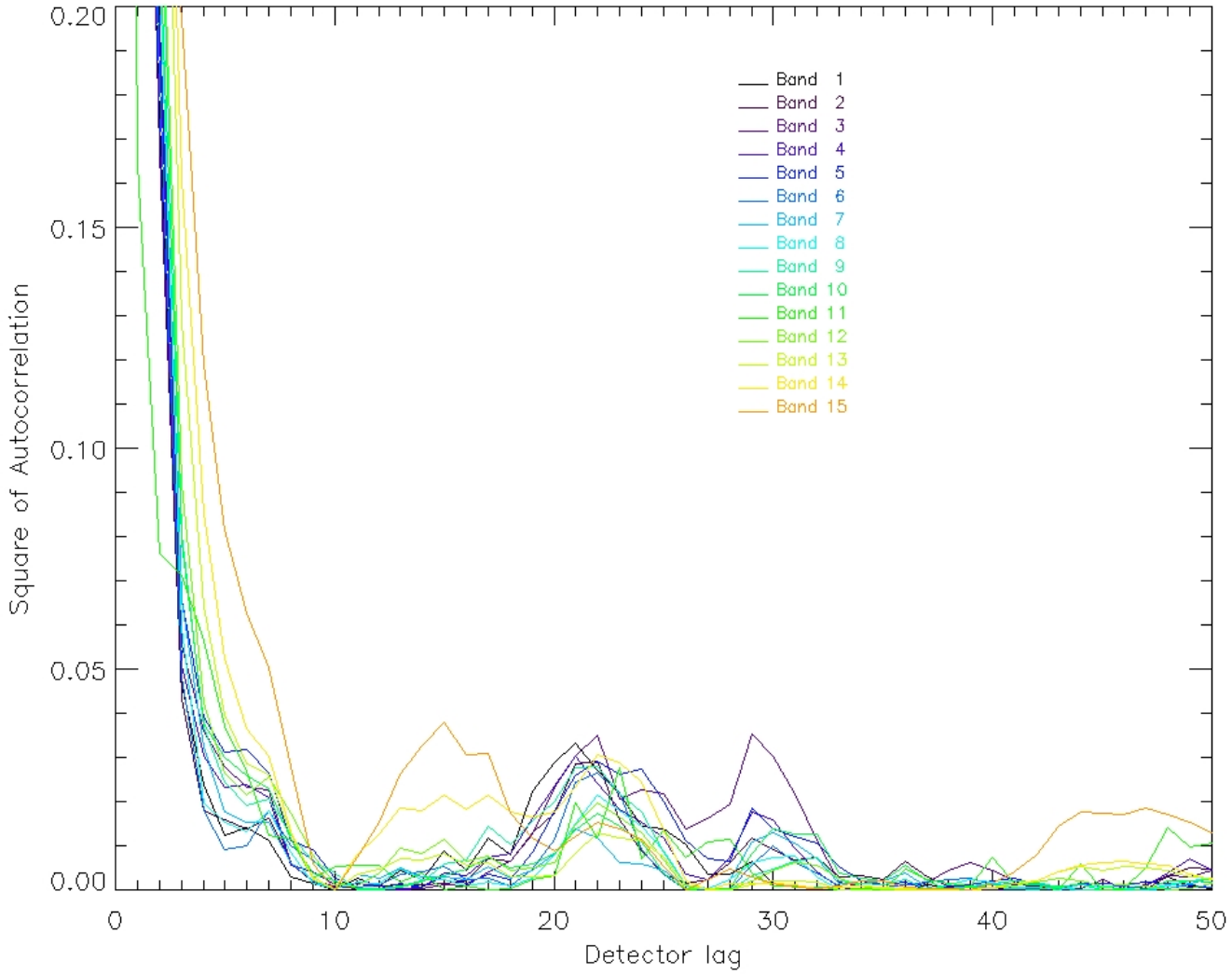

Figure 45: Zoom on the square of the autocorrelation function of the $\frac{\partial c_{eq}(\lambda,d,t)}{\partial t}$ *up to a 50 detector lag*

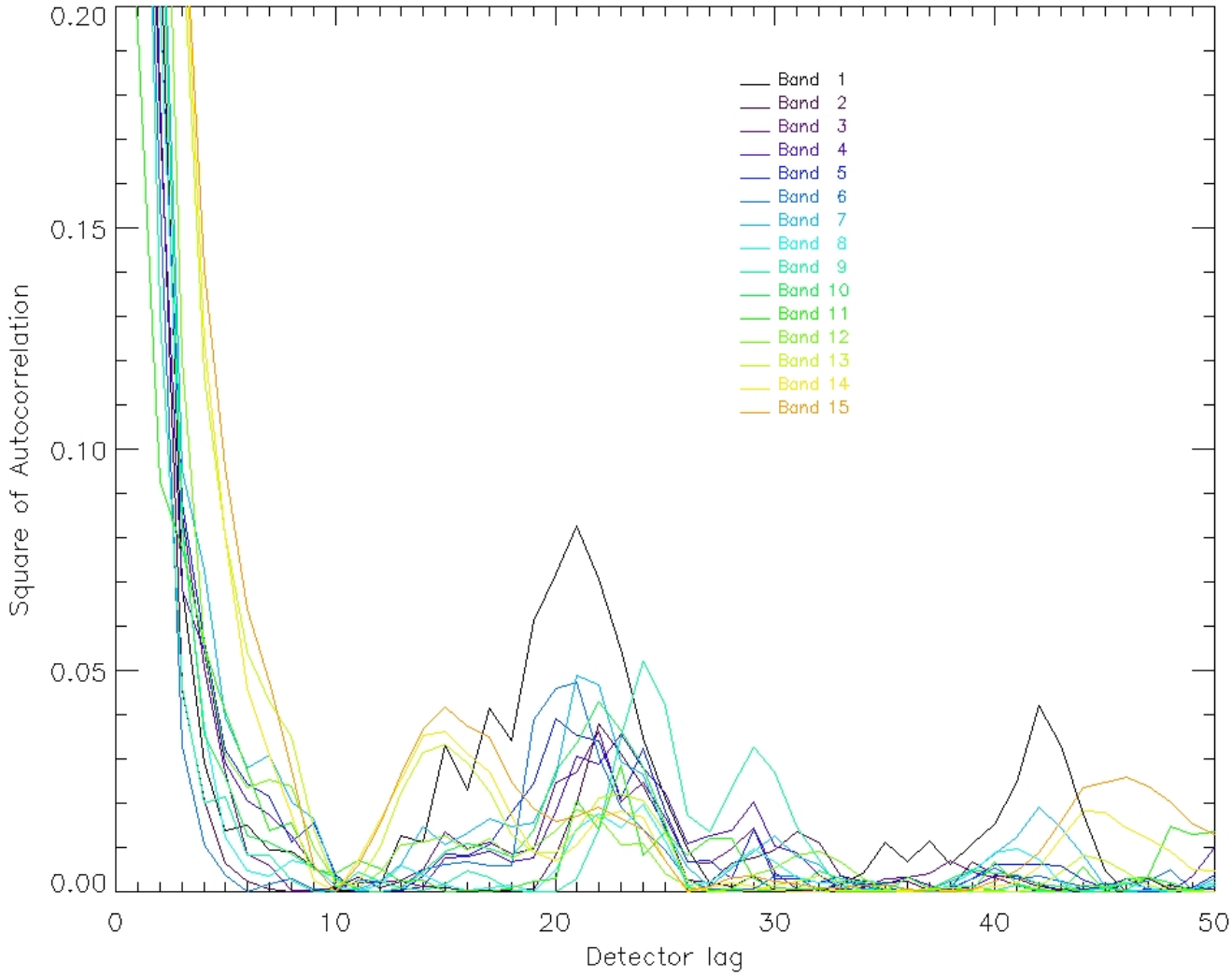

Figure 46: Zoom on the square of the autocorrelation function of the $\frac{\partial^2 c_{eq}(\lambda,d,t)}{\partial t^2}$ *up to a 50 detector lag T*

We have also generated Fast Fourier Transform (FFT) of the $c_{eq}^{t=0}(\lambda,d)$, with the same objective in mind of finding characteristic spatial frequencies. Because the mean value across the swath of $c_{eq}^{t=0}(\lambda,d)$ is 1 with small deviations to this mean at each detector, the norm of the FFT exhibits a strong for the spatial frequency 0. To put the emphasis on the variations around the mean values, we show in the function ||FFT[$c_{eq}^{t=0}(\lambda,d)$-1]|| rather than ||FFT[$c_{eq}^{t=0}(\lambda,d)$]||. Note that only $c_{eq}^{t=0}(\lambda,d)$ belong to group 2 which explains the values of the abscissa.

For all bands we note that largest terms are for spatial frequencies below 50 detectors (numerically, we computed that about 60% of the $c_{eq}^{t=0}(\lambda,d)$ variations can be reproduced with spatial frequencies smaller than 50 detector)

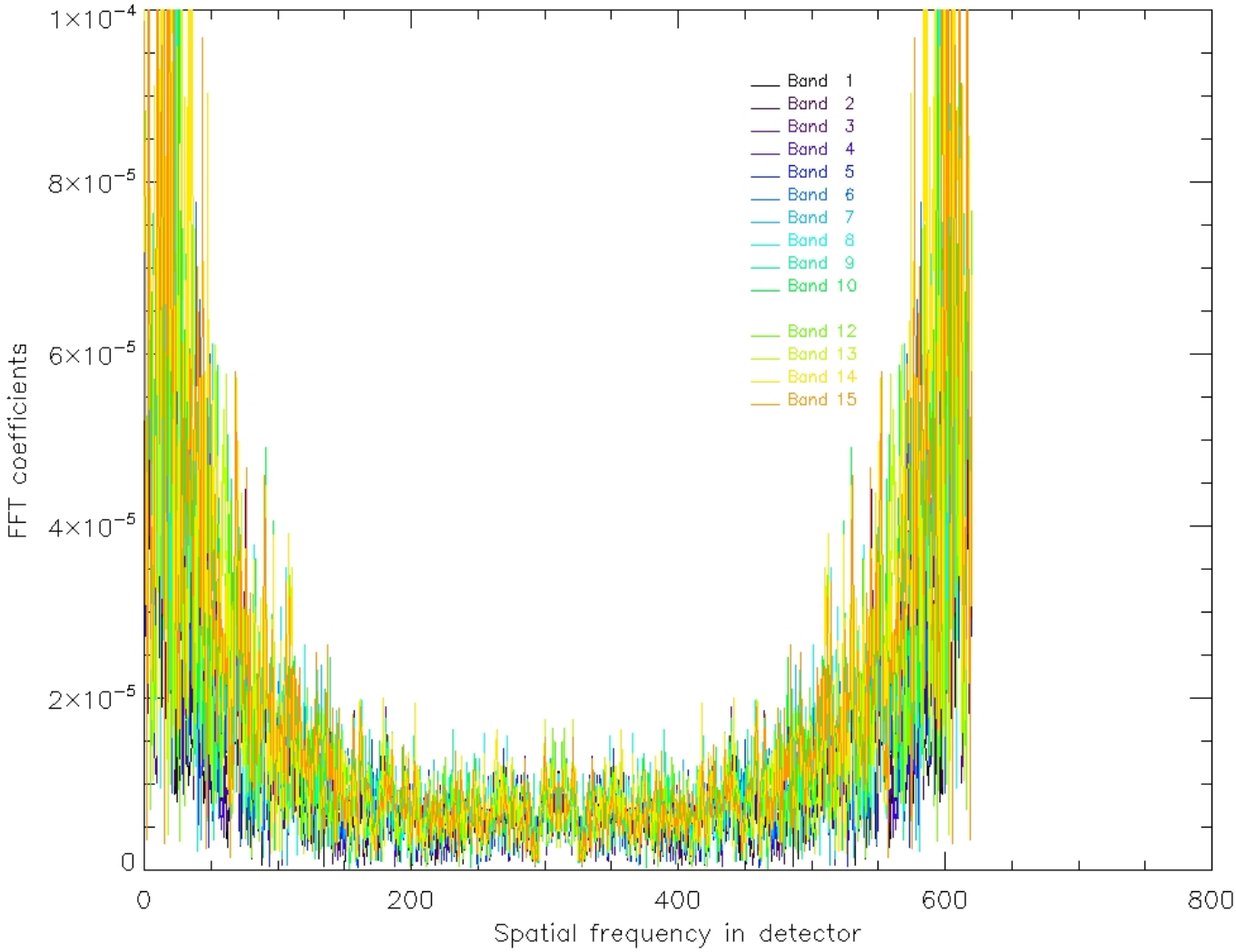

Figure 47: The norm of functions FFT [$c_{eq}^{t=0}(\lambda,d)$-1] for all bands (but band 11)

6.2.6 Is there any impact of the OCL off period on the equalization coefficient retrieval

The OCL was off from 13/12/2004 to 09/10/2006.
There is no visible signature of this period in the values the equalization coefficients retrieved on a product basis: see for instance Figure 17.

There is no visible signature of the OCL off period in the variation of the $\sigma_{detector}(\lambda)$ and $\sigma_{frame}(\lambda)$, which are respectively proxies for the across track and along track noise (see Figure 21, Figure 22, Figure 23, Figure 24) nor in our proxy for at camera interface radiometric differences.

6.3 Impact of the correction on the retrieval of water leaving reflectances

We showed that the equalization procedure introduces bias over a product of less than 0.01% TOA. The standard deviation of their variations around the values 1 is below 0.2% for all bands.
The autocorrelation and FFT analysis of the equalization coefficients revealed that they have the characteristics of random variables of the detector index.
In a previous study (see *R - 7*) see, we presented a simplified version of the MERIS operational atmospheric correction, the so-called 4-band Least Square atmospheric correction. Its performance and behaviour on a set of where shown to be similar to the operational algorithm. We used this alternative atmospheric correction to propagate TOA random and systematic errors via a Monte Carlo approach on a set of 80 Case 1 matchups (see R - 5).
We came to the following conclusions:

- Perturbations of the TOA signal by random errors characterized by a standard deviation below 0.5 % do not introduce significant biases (i.e., greater than 5%) at normalized water leaving reflectance level.
- Perturbations of the TOA signal by random errors characterized by a standard deviation below 0.5 % have no significant impact on the retrieval of normalized water leaving reflectance in the visible (band 1 to 5). By no significant impact, we mean that the probability of retrieval error greater than 5% on the water leaving reflectance is less than 0.1.
- Perturbations of the TOA signal by random errors characterized by a standard deviation of even less than 0.1 % can have a significant impact on the retrieval of normalized water leaving reflectance in the red-NIR (band 620 nm and beyond). By significant impact, we mean that the probability of retrieval error greater is than 5% on the water leaving reflectance is larger than 0.1.

This gives ground to claim that the equalization should have no significant impact on the bias associated to the water leaving reflectance retrieval errors as assessed with MERMAID for instance. It should have no significant impact on the retrieval of the water leaving reflectances in the visible in Case 1 waters. It could have a significant impact on the retrieval of the water leaving reflectances in Case 1 waters for wavelength longer than 620 nm.

These claims should however be verified by processing to L2 equalized products.

6.4 The detector-to-detector systematic radiometric differences: what causes them?

Our equalization coefficient corrects for the detector-to-detector systematic differences observed in MERIS products but we do not know the cause for these detector-to-detector systematic differences.

Let's summarize our findings on the equalization coefficients:

- They are multiplicative factors applied on a detector basis.
- They are slowly changing with time and their time variation can be modelled by a parabola.
- The standard deviation of their variations around the values 1 at detector not in the vicinity of camera boundaries is below 0.2%.
- They seem to equalize images regardless of their spectral characteristics or radiometric level (ocean, snow, vegetation).

How such detector-to-detector systematic radiometric difference can be introduced in the L1b?

Hereafter, we extracted from the L1b Detailed Processing Model (see *R - 8*), the so-called acquisition model:

$$X_{b,k,m,f} = NonLin_{b,m}\left[g(T_f^{VEU}).\left[A_{b,k,m}.\left(L_{b,k,m,f} + G_{b,k,m}(L_{*,*,*,f})\right) + Sm_{b,k,m,f}(L_{b,k,m,*})\right] + g_c(T_f^{CCD}).C^0_{b,k,m}\right] + \varepsilon$$

where

- $X_{b,k,m,f}$ is the MERIS raw sample (not corrected on board);
- $NonLin_{b,m}$ is a non-linear function;
- T_f^{VEU} is the amplification unit temperature;
- T_f^{CCD} is the sensor temperature;
- $g(T)$ and $g_c(T)$ are temperature dependent gain terms (close to 1);
- $A_{b,k,m}$ the "absolute radiometric gain";
- $L_{b,k,m,f}$ the spectral radiance distribution in front of MERIS;
- $Sm_{b,k,m,f}$ the smear signal, due to continuous sensing of light by MERIS;
- $G_{b,k,m}$ a linear process representing the stray light contribution to the signal. For a given sample, some stray light is expected from all the other simultaneous samples in the module, spread into the sample by specular (ghost image) or scattering processes.
- $C^0_{b,k,m}$ the dark signal (corrected on board for temperature effects by the Offset Control Loop);
- ε is a random process representative of the instrument errors and parasitic processes not accounted for in the other terms of the model.

Inverting the acquisition model and we obtain the radiometric equation summarizing the MERIS L1b processing:

$$L_{b,k,m,f} = \frac{1}{A_{b,k,m}\, g\left(T_f^{VEU}\right)}\left[X'_{b,k,m,f} - S_{b,k,m,f} - C_{b,k,m,f}\right] - G_{b,k,m}(L_{*,*,*,f})$$

Where:

- $X'_{b,k,m,f} \equiv NonLin^{-1}_{b,m}\left(X_{b,k,m,f}\right)$
- $C_{b,k,m,f} = g_c\left(T_f^{CCD}\right) \times C^0{}_{b,k,m}$
- $S_{b,k,m,f}$ is an estimate of the term $g\left(T_f^{VEU}\right) Sm_{b,k,m,f}\left(L_{b,k,m,*}\right)$ obtained from the dark offset corrected smear band.

The suspect should be a detector dependant and band dependant term, slowly varying in time (e.g., not randomly from frame-to-frame). It should be one of the terms on the right hand side of the radiometric equation.

6.4.1 A straylight issue?

Unlikely: there is no obvious reason why the straylight correction should not introduce the type of detector dependant pattern we observe. The straylight effect and its correction are moreover frame dependant and scene dependant. The equalization seems how ever to work irrespective of the scene.

6.4.2 A dark current issue?

Unlikely: dark currents are much smaller than the actual counts associated with the geophysical signal. They act as an offset and not as a multiplicative corrective term. There is thus no obvious reason why the equalization coefficients could correct for a dark current correction residual error.

6.4.3 A non linearity issue?

Unlikely: the equalization seems to give good results at all radiometric level.

6.4.4 A smear issue?

Unlikely: although smear effect typically look like vertical stripping when induced by light saturation, our poor understanding of the smear correction leads us to think that the expected error for this term should not be detector dependant (rather frame dependant or scene dependant).

6.4.5 A calibration issue?

Not unlikely: calibration appears in the radiometric equation as a multiplicative factor. It is detector dependant. It is slowly evolving in time via the instrument degradation model. Contamination of the calibration counts by speckle has been claimed to potentially contaminating calibration measurements (see R - 2 and *R - 9*).

6.5 Could the equalization coefficients retrieval for single spectral bands be further constrained by band ratio equalization coefficients?

We discussed previously the reason why band ratios are so sensitivity to detector-to-detector systematic radiometric differences. Could such sensitivity be exploited to further constrain the retrieval of the equalization coefficients on a single product basis?

The retrieval of the equalization coefficient on a single product basis as we have described in this document can be seen a system of 15 equations and 15 unknown which we can resolve independently: for each band, we follow the steps indicated in section 3.2.2 and we obtain the equalization coefficients:

$c_{eq}(\lambda_1, d) = Y_1$

…

$c_{eq}(\lambda_{15}, d) = Y_{15}$ A band radio is defined as:

We have defined a band ratio as:

$$\gamma_{MERIS}(\lambda_1,\lambda_{2,}x,y)=\frac{\rho_{MERIS}^{TOA}(\lambda_1,x,y)}{\rho_{MERIS}^{TOA}(\lambda_2,x,y)}$$

If follows that:

$$\gamma_{MERIS}(\lambda_1,\lambda_{2,}x,y)=\frac{\rho_{MERIS}^{TOA}(\lambda_1,x,y)}{\rho_{MERIS}^{TOA}(\lambda_2,x,y)}=\frac{c_{eq}(\lambda_1,d=f(x,y))}{c_{eq}(\lambda_2,d=f(x,y))}\frac{\rho_{TRUE}^{TOA}(\lambda_1,x,y)}{\rho_{TRUE}^{TOA}(\lambda_2,x,y)}\equiv C_{eq}(\lambda_1,\lambda_2,d)\gamma_{TRUE}(\lambda_1,\lambda_{2,}x,y)$$

If we follow the same procedure described in section 3.2.2 for the retrieval of the $C_{eq}(\lambda_i,\lambda_{i+1},d)$ but apply it to a band ratio rather than a single band, we add to the previous system 14 more equations:

$$C_{eq}(\lambda_1,\lambda_2,d)=\frac{c_{eq}(\lambda_1,d)}{c_{eq}(\lambda_2,d)}=Y_{16}$$

…

$$C_{eq}(\lambda_{14},\lambda_{15},d)=\frac{c_{eq}(\lambda_{14},d)}{c_{eq}(\lambda_{15},d)}=Y_{29}$$

We have 29 equations and 15 unknowns (i.e., the $c_{eq}(\lambda_i,d)$) . This can be solved with a weighted least square method using a variance-covariance matrix based on the uncertainty estimates obtained from the individual retrieval of the $c_{eq}(\lambda_i,d)$ and $C_{eq}(\lambda_i,\lambda_{i+1},d)$.

Such methodology could be investigate.

6.6 Ground segment implementation: practical considerations

6.6.1 Implementation of the equalization procedure

The implementation of the equalization procedure is straightforward. It is a simple multiplication of each pixel by an equalization coefficient. The equalization coefficients at launch and it first and second derivative are provided in a LUT. Its entries are detector index and spectral band.

6.6.2 Smile correction

We already mentioned that the ground segment approach to the smile correction is methodologically erroneous (smile correction after gaseous, stratospheric aerosol and glint correction). However, for consistency, in order to apply the equalization coefficients generated with our breadboard to the ground segment processing chain, our breadboard should include a smile correction and gaseous correction identical to the ground segment. Modifying the smile correction in the ground segment should however be a better way to proceed.

6.6.3 FR versus RR

The equalisation procedure should be done at FR level and not a RR level because the RR detector are actually corresponding to the averaging of 4 physical CCD detectors in the across track dimension.

This requires that the FR products corresponding to the RR scenes we have used in this study be extracted from the ground segment. The FR coverage in year 2002 to 2005 of this region of Antarctica is scarce but is nominal afterwards. This means that the retrieval of FR equalization coefficients could be loosely constrained for the first years of the first years of the mission.

6.6.4 Didn't' we derive Quality Indicators?

What are the variable that we derived in the equalization process and its verification that we could use as Quality Indicators to monitor the performance of the MERIS mission (and potentially OLCI)?
Here is a list of potential Quality Indicators:

- $\sigma_{\mathrm{det}ector}(\lambda)$ and $\sigma_{frame}(\lambda)$ as shown in Figure 21 and Figure 28
- Camera interface radiometric difference as shown in Figure 24 to Figure 27

6.6.5 Computing time

The computing time required to retrieve the equalisation coefficients from a set of about 100 MERIS L1b RR files on a Xeon quadcore (8 nodes each at 2 GHz) with IDL multithreading capabilities (not fully exploited) is about 24 hours.
Once these coefficients are computed they can be applied to any smile corrected MERIS L1b scenes. The equalization itself is only a matter less than a minute computing time.

7 Conclusion

We have prototyped an equalization correction of L1b products after smile correction that could provide significant image quality improvement for the whole mission.

The equalization coefficients allow to both monitor and reduce detector-to-detector radiometric systematic differences and at camera interface systematic radiometric differences.

8 Acknowledgement

Thanks to R. Duca and for discussions.

9 References

R - 1: Georgi T. Georgieva, James J. Butler, The effect of speckle on BRDF measurements, Earth Observing Systems X, edited by James J. Butler, Proceedings of SPIE Vol. 5882 (SPIE, Bellingham, WA, 2005)

R - 2: Delwart, S., MERIS instrument characterization overview, US workshop 2006

R - 3: Taylor B. and Kuyatt C., Guidelines for Evaluating and Expressing the Uncertainty of NIST Measurement Results, NIST Technical Note 1297, 1994 Edition

R - 4: Fox N., A guide to expression of uncertainty of measurements
QA4EO-CEOS-GEN-DQK-006, v2.0, 2008

R - 5: Bouvet M., Instrumental Error Propagation for MERIS and OLCI: from L1B Top-Of-Atmosphere Reflectances to L2 Normalized Water Leaving Reflectances. ESA Technical Note, TEC-EEP/2008.321/MB

R - 6: Lawrence J.S., Ashley M.C.B., Burton M.G., Storey J.W.V., Dome C's Atmospheric Conditions: Implications for Astronomy, Chinese Astronomy and Astrophysics 31 (2007) 221–227

R - 7: Bouvet M., Presentation to the MQWG 15 on the MERIS matchups analysis (available on request)

R - 8: MERIS Level 1 Detailed Processing Model, Parameters Data List, PO-TN-MEL-GS-0002, V7.0

R - 9: Bazalgette Courrèges-Lacoste G., Enhancement of diffusers BSDF Accuracy, ESA contract 18432/04/NL/AR, Final report